Doctoral theses at NTNU, 2020:91

Xu Lu

Multi-scale study of hydrogen-assisted cracking in nickel-based superalloys

Doctoral thesis

Xu Lu

ISBN 978-82-326-4534-3 (printed ver.)
ISBN 978-82-326-4535-0 (electronic ver.)
ISSN 1503-8181

NTNU
Norwegian University of Science and Technology

NTNU
Norwegian University of Science and Technology
Thesis for the Degree of
Philosophiae Doctor
Faculty of Engineering
Department of Mechanical and Industrial Engineering

Doctoral theses at NTNU, 2020:91

NTNU
Norwegian University of Science and Technology

Xu Lu

Multi-scale study of hydrogen-assisted cracking in nickel-based superalloys

Thesis for the Degree of Philosophiae Doctor

Trondheim, February 2020

Norwegian University of Science and Technology
Faculty of Engineering
Department of Mechanical and Industrial Engineering

NTNU
Norwegian University of
Science and Technology

NTNU
Norwegian University of Science and Technology

Thesis for the Degree of Philosophiae Doctor

Faculty of Engineering
Department of Mechanical and Industrial Engineering

ISBN 978-82-326-4534-3 (printed ver.)
ISBN 978-82-326-4535-0 (electronic ver.)
ISSN 1503-8181

Doctoral theses at NTNU, 2020:91

Printed by NTNU Grafisk senter

Preface

This doctoral thesis is submitted to the Norwegian University of Science and Technology (NTNU), in fulfilment of requirements for the Doctor of Philosophy degree. The work was carried out at the Department of Mechanical and Industrial Engineering from September 2016 to December 2019. Prof. Afrooz Barnoush has been the main supervisor. Associate Prof. Astrid de Wijn has been the co-supervisor. The work was carried out in the NTNU Nanolab, the Nanomechanical Lab and Metallography Lab at the Department of Mechanical and Industrial Engineering.

The Research Council of Norway is gratefully acknowledged for the financial support through the project HyF-Lex (244068/E30), and the support to the Norwegian Micro- and Nano-Fabrication Facility, NorFab (245963/F50). Additionally, the China Scholarship Council is specially acknowledged for the financial support of this PhD work.

Xu Lu

Trondheim, January 2020

Acknowledgements

Three years of PhD work could not have been accomplished without the help and support from many people, whom I would like to express my acknowledgement.

First and foremost, my sincere gratitude goes to Prof. Afrooz Barnoush, for giving me the opportunity to join his group as a PhD candidate and supervising me over the past three years. Your endless inspiration, enthusiasm, support and guidance make every problem that steps into this journey solvable. The discussions with you that enriched my scientific knowledge will deeply engraved in my mind.

Associate Prof. Astrid de Wijn is specially acknowledged for being my co-supervisor and sharing with me your profound knowledge in the simulation world. I would also like to express my gratitude to Prof. Nuria Espallargas for her devotion to revising my thesis and taking care of my defense. Your efficiency and conscientiousness are deeply admired. Prof. Torgeir Welo is also appreciated for supporting me during the last few months and paving the way for my defense.

I would like to thank Dr. Nousha Kheradmand for guiding me in both metallography lab and nanomechanical lab. I also enjoy the moments discussing scientific problems with you. Mr. Ken Roger Ervik and Dr. Amin Hossein Zavieh are gratefully acknowledged for their technical support in the Nanolab. Dr. Yan Ma from RWTH Aachen University is specially thanked for the co-operation on materials characterization and fruitful discussions on phase transformations.

I give my gratitude to Prof. Reinhard Pippan, Dr. Evgeniy Merson and Associate Prof. Christer Westum Elverum for taking time to review my thesis, bringing up insightful comments and being part of the committee.

My sincere gratitude also goes to my awesome colleagues and officemates. I am very grateful to Dr. Yun Deng, for being a great friend and mentor in both daily life and scientific works. Thank you for sharing with me your experimental skills and insightful ideas. My PhD life could not have been so smooth without your help and guidance! The same gratitude goes to Dr. Di Wan. Your expertise in technical skills, especially SEM, helps me a lot achieving this day. You have always been an awesome friend and classmate during the past twelve years! I would also like to thank Mr. Jan Inge Hammer Meling for being a perfect friend who is always ready to shear life experiences

with us and being a good collaborator in scientific discussions. To Iman, thank you for helping me with TDS measurements.

To all the administrative staff and other colleagues at the Department of Mechanical and Industrial Engineering (MTP), I would like to thank you for creating an enjoyable and stimulating work environment. To all my friends in Trondheim, your support improved my life quality over the past three years!

Last but most importantly, I would like to express my deepest gratitude and love to my families. To my beloved parents for their unconditional encouragement, support and love that make me who I am today. To my dearest husband Dr. Dong Wang for holding my hands firmly through all the flowers and thorns. To my upcoming baby boy for lightening up our lives everyday ever since you are there. I love you all!

Xu Lu

Trondheim, Norway

Table of Contents

List of Abbreviations

AIDE	Adsorption-induced dislocation emission
APT	Atom probe microscopy
BCC	Body-centered cubic
BC	Bi-crystal
DFT	Density function theory
DSB	Dislocation slip band
EBSD	Electron backscatter diffraction
ECC	Electron channeling contrast
ECCI	Electron channeling contrast imaging
EDM	Electrical discharge machining
FCC	Face-centered cubic
FIB	Focused ion beam
GB	Grain boundary
HAGB	High-angle grain boundary
HE	Hydrogen embrittlement
HEA	High entropy alloy
HEDE	Hydrogen-enhanced decohesion
HELP	Hydrogen-enhanced localized plasticity
HESIV	Hydrogen-enhanced strain-induced vacancy formation
IG	Intergranular
LAGB	Low-angle grain boundary

O&G	Oil and gas
SEM	Scanning electron microscopy
SFE	Stacking fault energy
SSRT	Slow strain rate tensile test
TB	Twin boundary
TDS	Thermal desorption spectroscopy
t-EBSD	Transmission electron backscatter diffraction
TEM	Transmission electron microscopy
TG	Transgranular
TKD	Transmission Kikuchi diffraction
TTT	Time-Temperature-Transformation

List of Figures

List of Tables

Part I

1 Introduction

1.1 Motivation

The development of human history has been highly linked to the advance of technology and the exploration of resources, especially in the last two centuries. As the global energy resources and needs are still dependent on oil and gas (O&G) exploitation, the performance of equipment components used in this field still attract significant attention. A very important part of O&G equipment is the safety and sustainability control during the exploitation of reserves to avoid catastrophic accidents. This remains challenging due to the extreme environment at which the equipment components are exposed to, i.e. corrosive atmosphere, high-pressure high-temperature and in other instances extreme low temperatures conditions, mechanical forces, etc. Thus, the selection of the construction material is of vital importance for security reasons. Nickel-based superalloys, specifically precipitation hardened ones, are widely used in wellbore components in O&G production due to their combination of excellent mechanical properties, good corrosion resistance, and wide working temperature range [1]. However, the failure of nickel alloy components is frequently observed, which can lead to severe catastrophic consequences to humans and the environment. It is well-known that most of the failures are caused by environmentally assisted cracking [2, 3], and more specifically hydrogen embrittlement (HE), which has triggered the researchers' attention over the past decades and remains a hot topic until now.

The phenomenon of HE can be traced back to year 1874, when William H. Johnson reported the remarkable changes observed in iron and steel when exposed to hydrogen and acids [4]. Johnson observed an extraordinary reduction of mechanical properties in iron after immersion in hydrochloric and sulphuric acids. Since then, the investigation of HE has become especially noticeable in both academia circle and industry. In the O&G field, HE is a deleterious effect that reduces the lifetime of in-service components. As a frequently used alloy in the O&G industry, the research on HE susceptibility of nickel-based superalloys has been performed for decades and is still in progress [5-18]. Some of the proposed key factors affecting the resistance to HE of these series of alloys include: the microstructure of the material [12, 19, 20]; the strength of the alloy [17]; the evolution of secondary phases such as precipitates in the matrix and along the grain boundaries (GBs) [21-23]; hydrogen charging condition, i.e., whether it is internal hydrogen or external hydrogen [24, 25]; testing conditions, i.e., tensile stress condition, strain rate and

temperature [15, 25-27]; the distribution of the GBs and the nature of triple junction connectivity [28, 29], etc. Both intergranular (IG) and transgranular (TG) fracture modes have been observed on failed samples after hydrogenation. Researcher have also tried to unravel the underlying mechanisms for each failure mode [18, 19, 21-23, 30]. However, a large number of unknowns around the failure mechanisms still exist and HE is a complex subject in which no consensus has been reached until now. Additionally, HE behavior varies from one material to another as they usually possess different microstructures. To probing the HE phenomenon and to clarify the above-mentioned factors, each material should be investigated separately.

For nickel alloys, there are many unsolved questions regarding the failure mechanisms related to HE. Firstly, during electrochemical hydrogen charging, the preservation of a clean surface after charging remains a difficult task. The influence of electrochemical charging on the corresponding microstructure change is usually ignored, even though hydrogen diffusion is sluggish in face-centered cubic (FCC) alloys. It is widely recognized that GB δ phase is the common reason for IG cracking [22]. Though, the causes of non-precipitate-decorated GB cracking are rarely studied and documented. High-angle GBs (HAGBs) are proposed to initiate cracks [31], however, the measurement of misorientation alone, which is based on the 2D surface information, is not adequate due to the complex structure of GBs and the effect from adjacent grains. Additionally, the role of hydrogen in the dislocation interaction with specific GBs remains unclear. Moreover, due to the resolution limitation of the available microscopic techniques, the interaction of strengthening phases with sizes only in the range of tens of nanometers, with hydrogenated dislocations is difficult to discern until now. This aspect is beneficial for unrevealing the underlying mechanisms for TG failure in precipitation hardened nickel alloys. Beyond that, the behavior of these precipitates to hydrogen trapping needs detailed investigations. So far, tuning the possible parameters to improve HE resistance in nickel alloys remains a significant and ongoing topic.

A comprehensive insight to hydrogen influence and weakening effects on mechanical properties of Nickel-based superalloys is required. With the application of advanced and state-of-the-art testing and characterization techniques, i.e. nanoindentation, small-scale tensile test, scanning electron microscopy (SEM), transmission electron microscopy (TEM), focused ion beam (FIB) and atom probe microscopy (APT), hydrogen interaction with defects can be thoroughly studied

in a confined region under controlled conditions. Combination of these methods at different length scales can lead to address the missing approach and lack of knowledge in the literature.

1.2 Objectives

The main goal of this thesis is to gain a comprehensive understanding of the mechanisms for hydrogen-assisted mechanical degradation in two types of nickel-based superalloys, i.e. Alloy 718 and Alloy 725, which are the promising candidates for the components used in the O&G industry in the future. Experiments have been performed at several length scale including meso-scale, microscale and nanoscale. A series of advanced testing and post-mortem characterization techniques have been conducted during this PhD study to fulfill the following secondary objectives:

- Study the effect of electrochemical hydrogen charging on the mechanical degradation of precipitation hardened Alloy 718 and assess the possible mechanisms for IG and TG cracking.
- Compare HE behavior of precipitation hardened Alloy 718 and Alloy 725 in relation to their microstructures.
- Investigate the possible mechanisms for IG cracking in Alloy 725 by performing micropillar compression test containing several types of GBs.
- Choose an interstitial equimolar high-entropy alloy CoCrFeMnNi as a model material to investigate the underlying mechanism for TG cracking by conducting in-situ cantilever bending test.

1.3 Thesis overview

This thesis consists of an introductory part and a collection of four research papers that were published or are to be submitted to scientific journals.

Part I: The introductory part is composed of five chapters. Chapter 1 provides the motivation and an overview of the whole PhD work. Chapter 2 covers the fundamental background of HE and the well-known mechanisms to date. Chapter 3 states the basic properties of nickel-based superalloys and literature reviews on the relevant HE behavior. Chapter 4 surveys the main testing methods applied in the present work. Chapter 5 includes a summary of the journal papers on the thesis topic. Chapter 6 presents the main conclusions and outlook for future work.

Part II: This part compiles the publications that have been published or that are to be submitted to scientific journals.

1.4 List of papers and contributions

Four research papers published or to be submitted to a peer-review journal are included in this thesis. Two conference papers were published in conference proceedings. The details of the papers and author contributions are presented below.

Peer-reviewed journal papers:

1. **X. Lu**, D. Wang, D. Wan, Z.B. Zhang, N. Kheradmand, A. Barnoush, Effect of electrochemical charging on the hydrogen embrittlement susceptibility of Alloy 718, *Acta Materialia* 179 (2019) 36-48.
2. **X. Lu**, Y. Ma, D. Wang, On the study of hydrogen embrittlement behavior of nickel-based superalloys: Alloy 718 vs Alloy 725, *to be submitted to Materials Science and Engineering: A.*
3. **X. Lu**, et al., Hydrogen effect on the deformation behavior of Alloy 725 micropillars containing grain boundaries, *to be submitted to International Journal of Hydrogen Energy.*
4. **X. Lu**, D. Wang, Z.M. Li, Y. Deng, A. Barnoush, Hydrogen susceptibility of an interstitial equimolar high-entropy alloy revealed by in-situ electrochemical microcantilever bending test, *Materials Science and Engineering: A* 762 (2019) 138114.

Conference papers in proceedings:

1. **X. Lu**, A. Barnoush, Effect of electrochemical charging on the hydrogen embrittlement susceptibility of Inconel 718 superalloy, *3rd International Conference on Metals & Hydrogen*, Ghent, Belgium, May 28-31, 2018.
2. **X. Lu**, A. Barnoush, Small-scale study of hydrogen embrittlement susceptibility of nickel-based superalloy Alloy 725, *Eurocorr conference*, Sevilla, Spain, September 09-13, 2019.

Oral presentations in international conferences:

1. **X. Lu**, A. Barnoush, Effect of electrochemical charging on the hydrogen embrittlement susceptibility of Inconel 718 superalloy, *3rd International Conference on Metals & Hydrogen*, Ghent, Belgium, May 28-31, 2018.
2. **X. Lu,** Y. Ma, M. Zamanzade, Y. Deng, D. Wang, W. Bleck, W.W. Song, A. Barnoush, Insight into hydrogen embrittlement on medium-manganese steel via in-situ electrochemical nanoindentation test, *MSE conference*, Darmstadt, Germany, September 26-28, 2018.

Posters in international conferences:

1. **X. Lu**, A. Barnoush, Effect of electrochemical charging on the hydrogen embrittlement susceptibility of Inconel 718 superalloy, *3rd International Conference on Metals & Hydrogen*, Ghent, Belgium, May 28-31, 2018.
2. **X. Lu**, D. Wang, A. Barnoush, Hydrogen-induced cracking study on Ni-based superalloys, *MSE conference*, Darmstadt, Germany, September 26-28, 2018.

Statement of author contributions:

X. Lu planned and conducted the experimental work, analyzed the data and prepared the full manuscript. D. Wang helped with the in-situ electrochemical nanoindentation, micropillar compression and microcantilever bending tests. D. Wan helped with the electron backscatter diffraction data analysis and electron channeling contrast technique. Y. Ma performed the APT experiment. Y. Deng helped with the FIB experiments and planned the microcantilever bending tests. N. Kheradmand helped with the dislocation slip transmission analysis. Z.M. Li provided the high entropy alloys. A. Barnoush contributed with intellectual discussions on data analysis. All the authors contributed to revising of the manuscripts.

Other peer-reviewed publications that are not included in the thesis:

1. **X. Lu**, Y. Ma, M. Zamanzade, Y. Deng, D. Wang, W. Bleck, W.W. Song, A. Barnoush, Insight into hydrogen effect on a duplex medium-Mn steel revealed by in-situ nanoindentation test, *International Journal of Hydrogen Energy* 44 (2019) 20545-20551.

2. D. Wang, **X. Lu**, Y. Deng, X.F. Guo, A. Barnoush, Effect of hydrogen on nanomechanical properties in Fe-22Mn-0.6C TWIP steel revealed by in-situ electrochemical nanoindentation, *Acta Materialia* 166 (2019) 618-629.
3. D. Wang, **X. Lu**, D. Wan, Z. Li, A. Barnoush, In-situ observation of martensitic transformation in an interstitial metastable high-entropy alloy during cathodic hydrogen charging, *Scripta Materialia* 173 (2019) 56-60.
4. D. Wang, **X. Lu**, Y. Deng, D. Wan, Z. Li, A. Barnoush, Effect of hydrogen-induced surface steps on the nanomechanical behavior of a CoCrFeMnNi high-entropy alloy revealed by in-situ electrochemical nanoindentation, *Intermetallics* 114 (2019) 106605.
5. D. Wang, **Xu Lu**, et al., Effect of hydrogen on the embrittlement susceptibility of Fe-22Mn-0.6C TWIP steel revealed by in-situ tensile tests, *to be submitted*.

2 Hydrogen embrittlement

2.1 Phenomenology

Ever since William H. Johnson revealed the extraordinary changes in the breaking-strain and toughness of a piece of iron that was immersed temporarily in acids [4], the terminology of hydrogen embrittlement (HE) has been brought up and developed as a hot topic for decades. Hydrogen, as the lightest but most abundant chemical substance in the universe, can lower the load-bearing ability of many metallic materials. Such effect can strongly reduce the lifetime of an in-service construction material and lead to unexpected catastrophes. For example, the offshore O&G industry has been experiencing “the bolt problem”, the frequently observed bolt failures in the components, which is critical for subsea safety equipment [32]. It was concluded that the failure of numerous bolts was caused by hydrogen-induced stress corrosion cracking due to the HE. This phenomenon is always challenging for the offshore industry since hydrogen is generated at the surface during cathodic protection. Apart from offshore constructions and offshore typical alloys, hydrogen can affect many other applications and alloys, such as high strength steels [33-35], nickel alloys [36-41], high entropy alloys [42-46], titanium alloys [47, 48] etc. Despite numerous experimental and numerical research works dedicated to revealing the intrinsic mechanisms of HE and proposed several popular mechanisms [45, 49-66], there is no consensus reached in the understanding of HE and sometimes controversial findings are reported. The complication of HE originates from several aspects, on one side, there are the environmental and mechanical aspects and on the other side, there are the materials itself [67]. In addition, the complication of HE is based on the intrinsic properties of hydrogen as well such as the difficulties in detecting hydrogen in failures [63]. With so many challenges, the necessity of designing critical experiments becomes a must and urgent task for the future HE studies and understanding of the mechanisms related to this phenomenon.

2.2 Hydrogen entry, diffusion and trapping

Hydrogen entry into metals or alloys may lead to HE. As the most abundant element, hydrogen can be introduced into materials in several ways: through hydrogen gas exposure or by electrochemical reactions [68]. Molecular hydrogen gas can enter a molten metal surface during manufacturing processes, dissociate in solution and retain as a mono-atomic solute upon

solidification [69]. Since the diatomic hydrogen molecule is too large to enter the surface of a solid metal, it must be dissociated into single atoms to cross the gas/metal interface. The amount of hydrogen dissolved in metals is proposed to be proportional to the square root of hydrogen pressure $P_{H^2}^{1/2}$ by Sieverts [70] at an equilibrium state:

$$\frac{1}{2}\mathrm{H_{2(g)}} + \mathrm{M} = \mathrm{MH_{abs}} \tag{2.1}$$

$$C = KP_{H^2}^{1/2} \tag{2.2}$$

where C is the solubility of hydrogen in the metal and K a constant. It has been investigated on iron and nickel that hydrogen solubility is a function of temperature [71]. Another way of hydrogen entry is due to electrochemical reactions (redox) in aqueous medium. This normally occurs during cathodic protection, acid cleaning or electroplating processes [69]. In this case, hydrogen solubility is proportional to the square root of the cathodic charging current density [68]. Hydrogen produced from electrolytes normally consists two steps. The first step is to generate adsorbed hydrogen on metal surface ($\mathrm{MH_{ads}}$). This can be accomplished in either discharge of hydrated protons in acid solutions (eq. 2.3) or through the electrolysis of water in alkaline solutions (eq. 2.4) [67]:

$$\mathrm{H_3O^+ + M + e^- \rightarrow MH_{ads} + H_2O}\ \text{(in acid solution)} \tag{2.3}$$

$$\mathrm{H_2O + M + e^- \rightarrow MH_{ads} + OH^-}\ \text{(in alkaline solution)} \tag{2.4}$$

In the second step, most of the hydrogen atoms recombine to form diatomic gaseous hydrogen and escape through either chemical desorption (eq. 2.5) or electrochemical desorption (eq. 2.6-2.7) [67]:

$$\mathrm{MH_{ads} + MH_{ads} \rightarrow H_2 + 2M} \tag{2.5}$$

$$\mathrm{MH_{ads} + H_3O^+ + e^- \rightarrow H_2 + H_2O + M}\ \text{(in acid solution)} \tag{2.6}$$

$$MH_{ads} + H_2O + e^- \rightarrow H_2 + OH^- + M \text{ (in alkaline solution)} \quad (2.7)$$

But part of the adsorbed hydrogen on the metal surface can diffuse through the metal surface and be absorbed:

$$MH_{ads} \rightarrow MH_{abs} \quad (2.8)$$

In a real experimental study, the so-called "hydrogen recombination poison", which refers to the compound that is poison catalyst for a hydrogenation reaction, is normally added into the solution to promote hydrogen entry into metals. The most effective promoters for hydrogen absorption are based on the V-A and VI-A group elements [67].

In addition to the above-mentioned charging methods, a novel charging approach by generating plasma phase of hydrogen on an Fe-3wt%Si steel was successfully reported [72]. Other hydrogen charging methods involve the use of advanced environmental SEM and TEM equipment [73, 74], which enable a real-time observation of hydrogen-induced cracking and hydrogen-dislocation interaction.

Once a certain concentration of hydrogen atoms is set up at the metal surface, there will be a motion of the atoms into the material called concentration gradient-driven diffusion process. This process is normally described by the Fick's law, where the diffusion flux density j_D $[cm^{-2}s^{-1}]$, which is defined as the number of atoms passing through a unit area per unit time, is proportional to the concentration gradient [75]:

$$j_D = -D\frac{d_c}{d_x} \quad (2.9)$$

D is a proportionality constant referred to as the diffusion coefficient or diffusion constant. In most cases, the flux density is of little interest, but the information of concentration change in space with time is more important:

$$\frac{\partial c}{\partial t} = D\frac{\partial^2 c}{\partial x^2} \quad (2.10)$$

By applying special initial and boundary conditions, the above partial differential equation can be solved as time and spatial position-dependent concentration variation. The diffusion coefficient is confirmed to be sensitive to the temperature T by a Boltzmann factor:

$$D = D_0 \cdot \exp\left(-\frac{Q}{kT}\right) \tag{2.11}$$

Where D_0 is a pre-exponential factor and Q is the activation energy which is dependent on the diffused element and the crystal structures. Since hydrogen is the smallest chemical element, its diffusion rate in metal is larger than other interstitial or substitutional elements. In addition, the rate of diffusion process is highly dependent on the hydrogen trapping behavior in the metals. At ambient temperatures, the preferred interstitial sites for FCC metals are octahedral sites and for body-centered cubic (BCC) and hexagonal close packed (hcp) metals are tetrahedral sites due to the special atom arrangement in the lattice [76]. At a relatively high temperature (above 100 °C), part of the octahedral sites in BCC metals will be occupied [76]. Generally, hydrogen solubility in FCC metals is much higher than that in BCC metals.

Apart from lattice sites, microstructural trapping sites are more critical for HE, including vacancies, dislocations, interfaces between the matrix and precipitates, phase boundaries, grain boundaries (GBs), voids, nano- and microcracks, etc [77]. Those trapping sites are critical due to the disordered structures. Hydrogen traps are divided into reversible and irreversible types according to their activation energies, as illustrated in Figure 2-1. Compared to irreversible trapping sites, hydrogen atoms in reversible sites can jump out of the potential valley and becomes mobile. It was emphasized that there is no threshold value for the binding energy that separates reversible and irreversible sites [76] as the microstructure of the metal, time and environment should also be accounted for. Two popular experimental methods for studying hydrogen diffusion and trapping behavior are electrochemical permeation and thermal desorption tests. For example, in a thermal desorption experiment, weakly trapped hydrogen can diffuse out at relatively low temperature, while a higher temperature is required to release the irreversible trapped hydrogen. However, the actual temperature for releasing hydrogen is highly dependent on the heating rate and hydrogen distribution profile inside the metal. It is very important to clarify this during the test. While those traps lower the mobility of hydrogen atoms, their existence undoubtedly enhance the uptake of

hydrogen. As a result, those trapping sites are more vulnerable and have a higher chance to initiate cracks during plastic deformation.

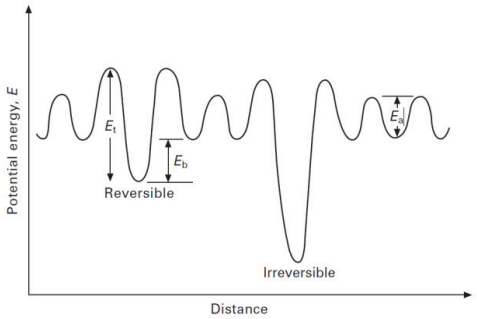

Figure 2-1: Schematic of the potential energy for interstitial sites with activation energy E_a and trapping sites with binding energy E_b and activation energy E_t. The activation energy for hydrogen release from the trap sites varies according to the nature of the trap sites. Adapted from Ref. [76].

In nickel-based superalloys, the complexity of the microstructure comes from different heat treatments. As an example, the microstructure of the precipitation hardened Alloy 718 normally contains carbonitrides, δ phase and fine precipitates γ' (Ni_3(Al, Ti)) and γ'' (Ni_3Nb). The possible reversible trapping sites include γ', γ'' precipitates, δ phases and GBs [9, 23, 78]. Carbonitrides are recognized as irreversible trapping sites for hydrogen with higher binding energy (77-87 kJ/mol) [23]. However, verification of hydrogen trapping behavior of precipitates is difficult by using thermal desorption spectroscopy (TDS) and electrochemical permeation analysis due to the complex microstructure. A recent study by Zhang et. al. [21] used Nanoscale Secondary Ion Mass Spectrometry to investigate the hydrogen concentration in carbonitrides, δ phase, and at their interfaces with the matrix in a precipitation hardened Alloy 718. It was reported that carbonitrides and the matrix adsorbs less hydrogen during electrochemical charging than δ phase, which serves as the main crack initiation sites during mechanical loading. Additionally, no observable hydrogen segregation or depletion occurred at the interfaces between δ phase/carbonitrides and the matrix. However, crack linkage from the agglomerated carbonitrides might propagate into the adjacent matrix. Thus, it is necessary to combine the actual microstructure with hydrogen trapping and distribution information to thoroughly study HE mechanism.

2.3 Hydrogen embrittlement mechanisms

As mentioned in the motivation section, the discovery of HE opened a new era for the researchers who have been dedicated to reveal the detrimental effects of hydrogen in steels and alloys. Several candidate mechanisms have been proposed by different research groups, and each of them holds strong opinions. The experimental and simulation outcomes seem to show that it is impossible to choose one mechanism to explain all the hydrogen-related failures. Background information is usually required when discussing HE in a material. The type of hydrogen source, hydrogen content, testing conditions (e.g. stress level, strain rate, temperature) and intrinsic material properties (e.g. strength, microstructure and impurity level). In this section, several mechanisms proposed until now will be listed and discussed in brief.

Hydrogen-enhanced localized plasticity (HELP)

In 1972, Beachem [79] proposed a model to explain the reduced microscopic plasticity and altered fracture modes at crack tips during hydrogen-assisted cracking of steels. It was suggested that the existence of sufficient amount of hydrogen at the crack tip assists the plastic deformation. Further high-resolution fractography of hydrogen-assisted failed Ni and Fe showed evident localized plasticity near the fracture surface [80, 81]. However, those interpretations were solely based on posteriori observation of microstructures and were not able to accurately describe the underlying deformation process. Later, the “Illinois group” led by Birnbaum, Robertson and Sofronis conducted in-situ experiments in TEM, which allowed a real time observation of the deformation process in the gaseous hydrogen environment at a high spatial resolution [7, 51, 82, 83]. In all published results, they concluded that hydrogen is able to lower the stress required for dislocation motion, alternatively, the presence of hydrogen enhances dislocation source activation, increases dislocation activities and localizes the deformation through the formation of localized microvoids [84]. The reason for hydrogen promoting dislocation motion was later proposed by Birnbaum and Sofronis considering the hydrogen shielding effect [51, 85]. The segregation of hydrogen to dislocations and other elastic singularities modifies the surrounding stress field such that in some certain directions, dislocations move easily at a lower stress level. In addition, hydrogen can affect dislocation interactions. One manifestation is that dislocation pile-up distance is decreased with hydrogen. Another reported hydrogen effect is the localization of slip on a limited number of slip

planes [86, 87]. It is worth mentioning that when depicting this phenomenon, it is required to incorporate the influence of strain rate and temperature. At higher strain rate or temperature, hydrogen will detach from dislocations and act as a solid solution strengthening agent [54]. This mechanism was further linked to the evolved microstructure and fracture morphology on X60 grade steel [88], Ni [53, 89], pure iron [90], etc.

Despite numerous arguments provided by the "Illinois group", contradictory conclusions regarding the enhancement of hydrogen on dislocation mobility were published by using both atomistic simulation [91-94] and experimental methods [73, 74]. The pioneers do not explain the observed results from a thermodynamics viewpoint. Additionally, there are some uncertainties in the in-situ TEM experiment, which was thought to provide the direct proof of hydrogen enhancement on dislocation mobility. The size of the specimen for TEM observation was too small that the diffraction contrast was modified by the image force. In addition, the pressure changes inside the chamber when hydrogen was introduced might have influenced the outcomes. Instead, the electron channeling contrast imaging (ECCI) technique can provide more reliable results of the bulk information during plastic deformation and is widely used now [87, 95].

Hydrogen-enhanced decohesion (HEDE)

Pfeil [96] concluded in 1926 that "Occluded hydrogen has a remarkable weakening effect on the intercrystalline boundary" and "In addition to its effect on the boundaries, hydrogen decreases the cohesion across the cubic cleavage planes." This concept was further developed and by Troiano [97], Oriani [98], McMahon [99] and Gerberich [100, 101]. The essence of this mechanism is the accumulation of hydrogen atoms within specific regions of the crystal lattice can effectively reduce the cohesive energy of the matrix or interfaces. Such decohesion is usually linked to a direct separation of atomic bond when a critical stress state is reached. And it is more readily to occur at sharp crack tips, positions of maximum hydrostatic stress state and interfaces with metalloid impurities where hydrogen concentration is high [102]. HEDE mechanism cannot be validated experimentally due to the limitations of existing techniques to obtain atomic scale interactions. Instead, it was validated mainly through density function theory (DFT) calculations [103] and cohesive zone models [104].

However, the debonding of interatomic bonds during straining will inevitably involve plastic deformation, which can be proved by the slip lines and small dimples on the "flat" fracture surfaces [105]. This indicates that hydrogen reducing cohesive energy between atoms is not the sole mechanism in hydrogen-assisted failure. Thus, combining HELP and HEDE, the concept of "hydrogen-enhanced-plasticity mediated decohesion" was proposed to explain the IG fracture and "quasi-cleavage" TG fracture in recent years [106-109]. Moreover, impurity segregation was reported to contribute to the embrittlement of GB and interface between matrix and the secondary phases, e.g. sulfur in nickel [110-113]. The disorder induced by the impurities should be considered when HEDE mechanism is taken into account. Figure 2-2 shows the deleterious effect of sulfur segregation on the fracture mode and ductility in nickel in presence of hydrogen [114].

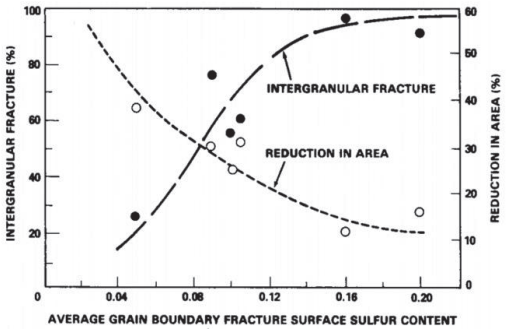

Figure 2-2: The effect of grain boundary sulfur coverage on the fracture mode and ductility in nickel at a hydrogenation environment. Adapted from Ref. [114].

Adsorption-induced dislocation emission (AIDE)

The AIDE mechanism was proposed by Lynch in 1976 [115] following the spirit of Clum [116]. As Lynch stated "The AIDE mechanism is more complex than the HEDE or HELP mechanisms", dislocation emission was deemed to include both nucleation and subsequent movement from the crack tip [102]. Dislocation nucleation consists of dislocation core formation and rearrangement of the lattice structure, which can be facilitated by the weakening of interatomic bonds by hydrogen. In addition, under sustained stress or monotonically increasing stresses, the AIDE mechanism also involves microvoid formation at slip band intersections ahead of crack tips. Normally in air environment, dislocation emission from crack tips is difficult due to the strong interatomic bonds. Dislocations emission ahead of the crack tip contributes to the plastic strain by forming large

dimples with little crack propagation. Higher stresses are needed to produce crack growth. In the hydrogen environment, in contrast, dislocations emit readily from crack tips and promote crack advances on appropriate slip planes due to the presence of hydrogen. Thus, a lower stress is needed to produce crack advance with shallower dimples and lead to embrittlement [102]. Figure 2-3 shows the schematic diagram of the AIDE mechanism at the crack tip [117]. This mechanism finds its application in interpreting hydrogen-assisted IG cracking in various steels and alloys in a recent review paper by Lynch [117].

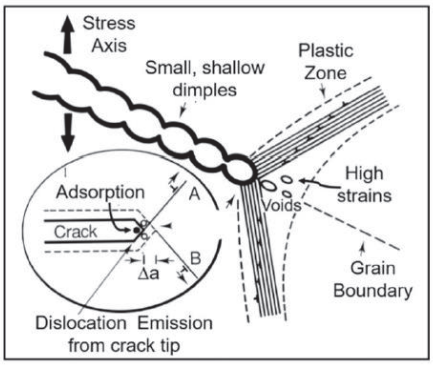

Figure 2-3: Schematic diagram showing the AIDE mechanism. Dislocation emission from crack tips promotes the coalescence of the crack with voids formed in the plastic zone. Adapted from Ref. [117].

Hydrogen-enhanced strain-induced vacancy formation (HESIV)

The HESIV model proposed by Nagumo states that hydrogen enhances the strain-induced vacancies leading to the reduction of mechanical properties [63, 118]. Hydrogen with excess vacancies form clusters act as void sources at stress concentrated area during plastic deformation. The HESIV model shifts the focus in HE from hydrogen itself to the hydrogen-related failure mechanism. A direct experimental evidence of the primary role of vacancies over hydrogen in HE has been published in Ref. [64]. It reveals the hydrogen-related failure on Inconel 625 and iron by conducting tensile test with interposed unloading and reloading in hydrogen-charged and hydrogen-free conditions. Aging and annealing were performed during unloading stage to anneal out strain-induced vacancies or to diffuse out hydrogen. The loading curves of Inconel 625 (Figure 2-4) shows that by annealing at 200 °C at the unloaded stage, both hydrogen and strain-induced defects are removed, and the drastic degradation caused by hydrogen can be completely recovered.

By aging at 30 °C, however, where only hydrogen is removed, a reduction of fracture strain is still observed. In addition, thermal desorption profiles also demonstrated an enhanced hydrogen absorption capacity when hydrogen was present during straining [64], which indicates that hydrogen promotes the generation of strain-induced defects. The fully recovery of mechanical properties at 200 °C annealing temperature indicates that point defects dominant in the degradation process, i.e. vacancies.

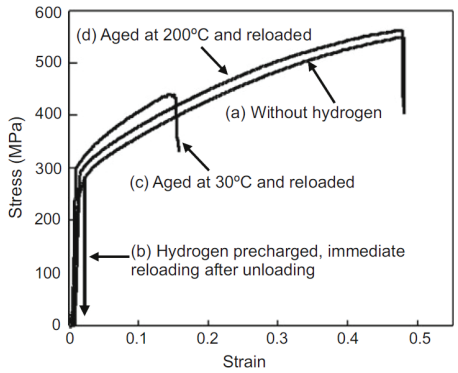

Figure 2-4: Stress-strain curves of Inconel 625 at tensile tests with interposed unloading conditions. Adapted from Ref. [64].

The correlation between HE susceptibility and the amount of strain-induced vacancies regarding the effect of grain size [119] and chemical composition [120] was further reported. Also, the enhanced degradation by reducing the strain rate in a cold-worked eutectoid steel is related to the increasing amount of strain-induced vacancies [121]. Concomitantly, first principle calculations based on DFT confirmed the essential factor of supersaturated vacancies in hydrogen-assisted degradation behavior [122, 123]. The HESIV mechanism was also applied to explain the hydrogen-induced failure [78, 124, 125] and softening [126] in pure Ni.

Defactant theory

The mechanism of Defactant (DEFect ACTing AgeNTS) was proposed by Kirchheim [60, 61, 127]. By using the generalized Gibbs adsorption isotherm, the formation energy of defects, e.g. vacancies, dislocations, stacking faults, void or crack surfaces was concluded to be reduced by solute segregation, a phenomenon analogy to surfactants reduce surface energies in liquid.

Hydrogen is considered as such solute in solid metals. The Defactant theory is suitable to explain the activation of local plasticity. A direct experimental proof of this mechanism is the quantitative estimation of the reduced formation energy of dislocation loops in presence of hydrogen obtained from in-situ nanoindentation test [56, 128-130]. Similar result was also reported on tungsten charged with deuterium plasma by conducting ex-situ nanoindentation test [131]. Also, the elevated stress of α-vanadium micropillars compressed in hydrogen environment was explained by an increase in dislocation density due to the Defactant mechanism [132]. To some extent, the enlarged vacancy concentration with hydrogen reported by Kirchheim consists of the essence of HESIV mechanism, but originated from different perspectives [61].

As stated at the beginning of section 2.3, HE itself is a complicated matter and it is impossible to choose only one mechanism to explain all the observed results. One should perform critical experiments at multi-scale levels to get a thorough understanding of the possible reasons for HE in the materials under study.

3 Ni-based superalloys and related HE studies

Nickel-based superalloys are commonly classified into solid solution strengthening and precipitation strengthening alloys. Several commercially used solid solution strengthening alloys are Inconel 600, Hastelloy X and precipitation hardening alloys are Inconel 718, Inconel 909, Nimonic 90, X-750, etc [133]. The most important phases in nickel-based superalloys are:

- Gamma matrix (γ), austenitic, FCC solid solution phase, contains a high percentage of solid-solution elements such as Co, Cr, Mo, and W;
- The intermetallic precipitate γ' (gamma prime), FCC Ll_2 structure, stoichiometric composition as Ni_3(Al, Ti), spherical or cuboidal shape, coherent;
- The intermetallic precipitate γ'' (gamma double prime), body-centered tetragonal (BCT) $D0_{22}$ structure, stoichiometric composition as Ni_3Nb, disc shape, coherent but metastable;
- The intermetallic precipitate δ (delta), orthorhombic $D0_a$ structure, stoichiometric composition as Ni_3Nb, needle shape, incoherent;
- Carbides, cubic MC and $M_{23}C_6$ (M=Ti, Mo, V, Ta, Zr);
- Topologically close-packed phase (TCP): σ (Sigma).

In the following sections, the materials studied in this PhD thesis (Alloy 718 and Alloy 725) will be introduced and then followed by a detailed description of the HE behavior in nickel-based superalloys.

3.1 Alloy 718 and Alloy 725

In the 1980s, the need for a new material to fulfill the high H_2S, high-pressure gas well application was driven by the O&G companies. Alloy 718 was selected as a good candidate which combines high strength in the aged condition (ultimate tensile strengthen up to 1034 MPa), high temperature resistance up to 704 °C (1300 °F), good corrosion resistance and availability in various sizes [134]. It is an austenitic nickel-chromium (Ni-Cr)-based superalloy designed initially for aerospace applications and soon was used in extremely corrosive environments. It has been widely used in valves, fasteners, tubing hangers and well head completion equipment. Typical composition range for Alloy 718 are shown in Table 3-1. A high amount of Cr and Mo increases the chemical stability in corrosive environment. The addition of Nb, Al and Ti contributes to the strength via

precipitation hardening during heat treatments. Nb also helps to overcome the cracking problems during welding. For most applications, precipitation hardened Alloy 718 is widely used. By applying proper heat treatments, strengthening phases γ' and γ'', which are coherent and ordered, can be homogeneously distributed into the matrix (γ phase). A typical heat treatment for most applications involves two steps, i.e. solution annealed between 1024-1052 °C (1875-1925 °F) and water quenched, followed by aging in the range of 551-567 °C (1425-1475 °F) for 6-8 h and air cooled. A typical Time-Temperature-Transformation (TTT) diagram for Alloy 718 is illustrated in Figure 3-1 [135], from which it is seen that other phases, e.g. δ, σ phases, can be obtained at proper temperature and aging time. The above TTT curve is applicable for wrought Alloy 718 containing 5.38 % Nb and 0.07 % Si [135]. Any constituent variation can change the actual TTT diagram. Also, Nb/Ti-rich carbides are usually observed in the matrix [105]. However, carbides, δ phase and σ phase are potentially deleterious to both strength and toughness.

Table 3-1: Composition range of Alloy 718 [136].

Element	Ni	Cr	Fe	Nb	Mo	Ti	Al	Co
wt. %	50-55	17-21	Balance	4.75-5.50	2.80-3.30	0.65-1.15	0.20-0.80	<1.00
Element	C	Mg	Si	P	S	B	Cu	
wt. %	<0.08	<0.35	<0.35	<0.015	<0.015	<0.006	<0.30	

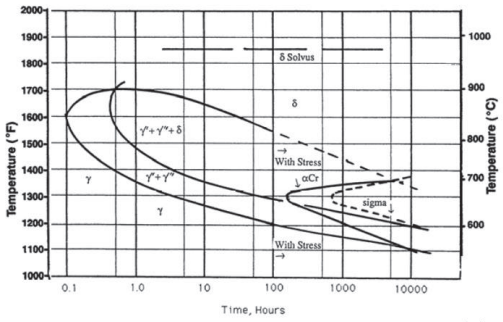

Figure 3-1: Time-Temperature-Transformation diagram for Alloy 718. Adapted from Ref. [135].

Despite excellent mechanical and corrosion resistant properties, Alloy 718 still suffers from localized corrosion when sulfur and halide irons are present [1, 137]. Alloy 725 was developed

with comparable strength to Alloy 718, however, with improved corrosion resistance particularly to pitting and crevice corrosion. The attractive properties makes this alloy applicable in challenging environments, such as sea water and deep sour gas wells and mineral acids [134]. Applications for Alloy 725 in the O&G industries include hangers, landing nipples, side pocket mandrels where the environment contains a high level of H_2S, CO_2 and chlorides. The composition range of Alloy 725 is listed in Table 3-2. A typical TTT diagram for Alloy 725 is illustrated in Figure 3-2 [138]. Similar to Alloy 718, age-hardened Alloy 725 contains strengthening phases γ' and γ'' in the FCC matrix. The δ phase can potentially precipitate when Nb content is relatively high. Additionally, η phase, Ni_3Ti with ordered hexagonal $D0_{24}$ crystal structure, has been reported when aged at higher temperatures and longer times [139]. By solution annealing at 1040 °C with a rapid water quenching prior to aging, the formation of η phase can be avoided [140]. In addition, MC (Nb/Ti-rich) and $M_{23}C_6$ (Cr-rich) types of carbides usually form in the matrix.

Table 3-2: Composition range of Alloy 725 [139].

Element	Ni	Cr	Fe	Nb	Mo	Ti
wt. %	55-59	19-22.5	Balance	2.75-4.00	9.50-7.00	1.00-1.70
Element	Al	C	Mg	Si	P	S
wt. %	<0.35	<0.03	<0.35	<0.20	<0.015	<0.01

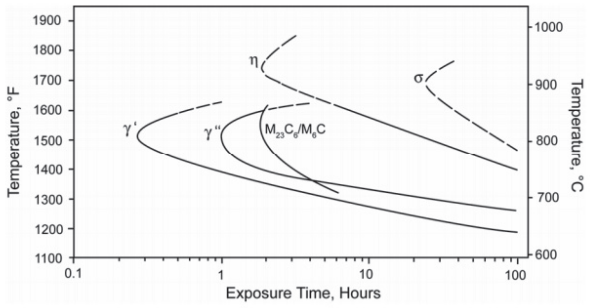

Figure 3-2: A Typical TTT diagram for Alloy 725. Adapted from Ref. [138].

3.2 Hydrogen diffusivity in nickel-based superalloys

In order to study the HE effects on nickel-based superalloys, hydrogen is introduced into the materials by either electrochemical charging in molten salt or through exposing to a high-pressurized hydrogen gas. Hydrogen penetration depth should be large enough to observe the HE effects, and it is an important data during post analysis. Some researchers have focused on the hydrogen diffusion and permeation in nickel-based superalloys for decades [8, 141, 142]. Normally when cathodic charging is applied, the penetration depth of hydrogen can be estimated according to eq. (3.1):

$$x = \sqrt{2Dt} \tag{3.1}$$

Where x is the penetration depth of hydrogen measured from the surface, t is the charging time. The temperature dependence of D fully agrees with the Arrhenius law, as shown by eq. (2.11). It is widely accepted that hydrogen diffusion rate is very low in FCC materials [143, 144]. Jebaraj [145] investigated the hydrogen diffusion coefficient of Alloy 718 under different metallurgical conditions and concluded that the effective hydrogen diffusion coefficient for solution annealed specimens ($5.3 - 6.8 \times 10^{-11} cm^2/s$) is higher than cold rolled ($3.3 - 4.2 \times 10^{-11} cm^2/s$) and precipitation hardened ($2.1 - 2.9 \times 10^{-11} cm^2/s$) ones. Two of the most widely used equations in recent papers for calculating the diffusion coefficient D come from Robertson [142] and Xu [8]:

$$D = 6.8 \times 10^{-7} \exp\left(-\frac{49.5 \times 10^3}{RT}\right) m^2/s \tag{3.2}$$

$$D = 4.06 \times 10^{-7} \exp\left(-\frac{48.63 \times 10^3}{RT}\right) m^2/s \tag{3.3}$$

3.3 HE in nickel-based superalloys

The investigations of HE in nickel-based superalloys traced back to 1960s [146], where Walter discussed the important roles of hydrogen adsorption and absorption in hydrogen-assisted cracking initiation and propagation. Hence forward, intensive studies on hydrogen-related failure in nickel alloys were carried out due to their importance as components parts in O&G fields. The following

sections focus on the two main failure modes in nickel-based superalloys, i.e. IG and TG cracking. The effect of precipitates on HE is discussed as well.

3.3.1 Hydrogen-induced IG cracking

GBs are always susceptible sites for crack initiation in hydrogen environment since hydrogen is easily to segregate at GBs [147], where hydrogen has a relatively high diffusion rate [148]. Crack initiation and propagation along GBs have already been reported in nickel-based alloys [19, 40, 149]. An example of hydrogen induced intergranular cracking on the age hardened Inconel 718 during slow strain rate tensile test (SSRT) is shown in Figure 3-3 [19].

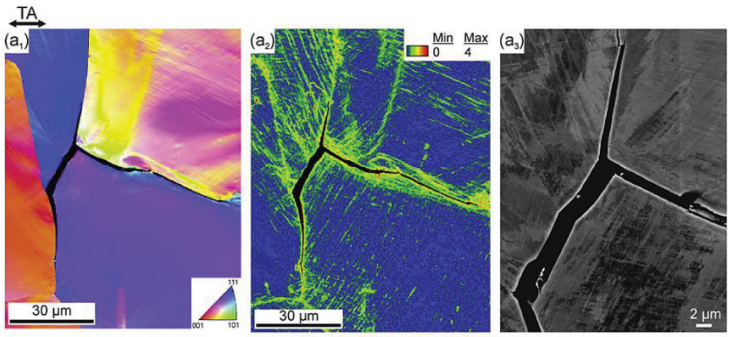

Figure 3-3: Hydrogen induced intergranular cracking at grain boundary triple junction: (a) and (b) Electron backscatter diffraction (EBSD) images, (c) Electro contrast channeling (ECC) image. Adapted from Ref. [19].

It was reported that the precipitation of δ phase along GBs may initiate crack when it is coarse enough [22, 150]. Other effects, such as the segregation of B, S, P, C etc. elements in Inconel 718 would change the morphology of GBs [150-152] and probably have some effect on the hydrogen diffusion process under loading. Besides segregation, GB misorientation angle was proved by Jothi [28] to affect the crack nucleation and propagation. He proposed that cracking was likely to appear at GBs having misorientations between 15° and 50° and no cracks were observed at low angle GB misorientations. The HAGBs are fast diffusion pipes for hydrogen due to their disordered structure, while the diffusion mechanisms are more complex at special GBs (Σ3-Σ29) because of the accommodation of defects [78]. Albeit GBs can be weak sites, the accumulation of a critical amount of hydrogen is the prerequisite for crack initiation [141].

3.3.2 Hydrogen induced TG cracking

Although IG cracking is usually observed, TG cracking is also frequently reported in the hydrogenated or non-hydrogenated nickel-based superalloys [18, 19, 28, 38]. It was proposed that TG crack may originated from carbides that distribute in the matrix, but more evidence showed that it is the localized slip deformation that plays the most critical role [153].

In the age hardened alloys, coherent precipitations (γ' and γ'') or ordering phases promote the planar slip since the gliding plane is softened when leading dislocations shear the precipitates and destroy the ordering [154]. As a result, the following dislocations prefer to stay on the same plane, which is easier to glide, e.g. {111} plane in nickel-based superalloys. In the presence of hydrogen, slip planarity is promoted due to the dragging effect of hydrogen. Besides, hydrogen lowers the stacking fault energy (SFE) to further impede dislocation cross-slip and enhance planar slip [102]. Hydrogen is preferred to accumulate at the stress concentrated areas, like crack tips or easy gliding planes where dislocation slip bands (DSB) exist [18]. Consequently, the synergetic effect of hydrogen and plastic deformation would lead to vacancies formation [155]. An example of hydrogen-enhanced nano-voids formation along DSBs is illustrated in Figure 3-4, which will further develop into quasi-cleavage failure and form TG fracture surface [18].

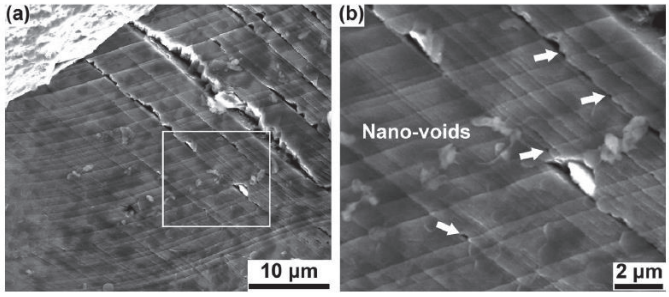

Figure 3-4: Fractography obtained by SEM from the regions with hydrogen in presence: (a) image showing the DSBs-like features on the fracture surface; (b) a magnified image from (a) showing the nano-voids formed along the traces. Adapted from Ref. [18]

3.3.3 Effect of precipitates on HE behavior

Among the most commonly observed precipitates in nickel-based superalloys, γ', γ'' and δ phases can be classified as reversible trapping sites with the binding energy of traps between 23-37 kJ/mol

[9]. In contrast, the carbides were proved to be irreversible trapping sites with de-binding energy of 77-87 kJ/mol, which is much higher than the threshold value for hydrogen to escape (58 kJ/mol) [9]. A schematic illustration of different traps was shown in Figure 2-1. The precipitation of δ phase along GBs show a deleterious effect when hydrogen accumulates at δ/matrix interface and results in a reduction in the bonding strengthen and crack initiation [19, 22]. In comparison, Galliano [16] proposed that the role of γ' and γ'' precipitates overweight δ phase and carbides on the HE susceptibility of Alloy 718 by conducting mechanical tests at different temperatures. For carbides, the precipitation location is critical in hydrogen-assisted cracking. The decoration of carbides along GBs frequently lead to IG cracks [156]. However, carbides in the matrix might not induced TG cracks due to the depletion of hydrogen at the incoherent interface between precipitates and the matrix [21]. Due to the complex microstructure of nickel-based superalloys, the role of each precipitate is expected to be further studied.

4 Experimental

4.1 Materials and sample preparation

Two types of nickel-based superalloys were used in this PhD thesis, i.e. Alloy 718 and Alloy 725. Alloy 718 was supplied by Aker Solutions (Norway), and Alloy 725 was provided by Böhler Edelstahl GmbH (Austria). The nominal compositions of these two alloys provided by the suppliers are listed in Table 4-1. These two alloys underwent standard API heat treatment processes. As received from the supplier, Alloy 718 was aged at 782 °C for 6.5 h followed by air cooling. The laboratory melt Alloy 725 was produced by vacuum induction melting and forged to a 133 mm bar. The Alloy 725 was aged with two steps: 732°C for 8 h and 621°C for 8h followed by air cooling. In addition, a homogenized interstitial equimolar CoCrFeMnNi high entropy alloy (HEA) with nominal composition (at. %) $Co_{19.9}Cr_{19.9}Fe_{19.9}Mn_{19.9}iNi_{19.9}C_{0.5}$ was used as a model material to study the hydrogen-assisted TG cracking. The HEA was supplied by Max-Planck Institute für Eisenforschung GmbH (Germany). The material was prepared by casting and hot-rolling at 900 °C, followed by homogenization at 1200 °C for 2 hours and water-quenching.

Table 4-1: Nominal compositions of Alloy 718 and Alloy 725 provided by the suppliers.

Alloy 718	Element	C	Fe	Cr	Nb	Mo	Ti	Al	Co	Ni
	wt. %	0.018	19.14	17.62	4.98	2.87	0.95	0.52	0.05	53.8
	Element	Si	S	P	B					
	wt. %	0.07	<0.0003	0.008	0.004					
Alloy 725	Element	C	Fe	Cr	Nb	Mo	Ti	Al	Mn	Ni
	wt. %	<0.01	10.1	19.7	3.6	7.3	1.4	<0.1	<0.02	57.6
	Element	Si	S	P						
	wt. %	<0.1	<0.001	<0.005						

Both Alloy 718 and Alloy 725 were cut into two-step dog-bone shape for SSRT by electrical discharge machining (EDM), as shown in Figure 4-1(a). Part of Alloy 725 and HEA were fabricated into round disk samples for micro-scale tests (Figure 4-1(b)).

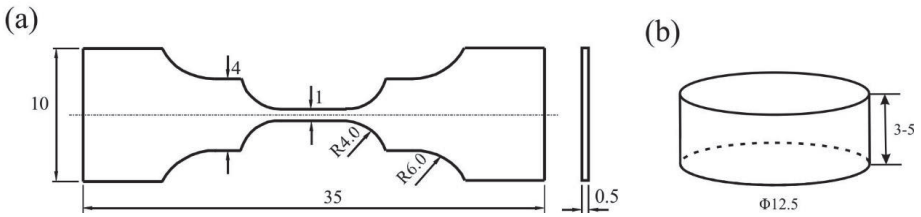

Figure 4-1: Specimen geometries for (a) two-step dog-bone and (b) disk samples (all dimensions are shown in mm).

All the samples were ground sequentially from 220 to 4000 grit SiC papers followed by mechanical polishing up to 1 μm diamond paste. Electropolishing was conducted in a methanolic H_2SO_4 solution at 26 V 30 s as the final step to obtain a deformation-free surface. For post-mortem analysis, the samples were mechanical polished and finished with a 0.04 μm colloidal silica suspension (OPS polishing).

4.2 Microcantilever and micropillar fabrication

The micro-sized cantilevers and pillars were fabricated using FIB (Helios Nanolab DualBeam FIB, Thermo Fisher Inc., USA) at 30 kV with a changing ion beam current. The microcantilevers were milled in a single grain with pentagonal cross-sections. Due to the lack of available data for the crystal planes that are most fragile to cracking, all the cantilevers were pre-notched to study the plane of {111} with the lowest surface energy. Dimensions of cantilevers are listed in the Appendix paper IV. The micropillars were bi-crystal (BC) pillars containing three types of GBs, i.e. twin boundary (TB), HAGB and low-angle GB (LAGB). Detailed parameters of the selected GBs can be found in the Appendix paper III. The pristine microcantilever and BC micropillar are shown in Figure 4-2.

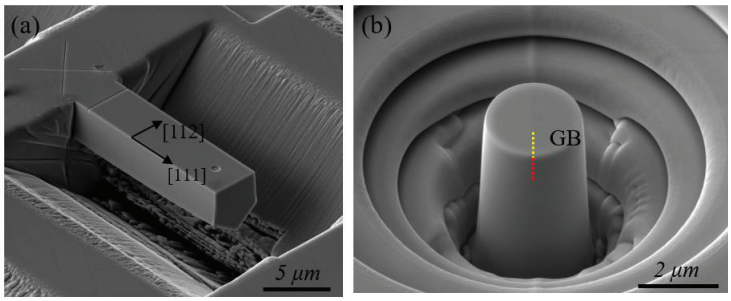

Figure 4-2: SEM images of the fabricated (a) microcantilever and (b) BC micropillar.

4.3 Electrochemical hydrogen charging

Regarding the samples for tensile test, ex-situ hydrogen pre-charging was performed in a three-electrode electrochemical cell. A platinum net was used as the counter electrode and Ag/AgCl (3 M KCl) was used as the reference electrode due to its wide working temperature range. The charging was performed at 75 °C at a constant potential of –1050 mV (equals to a cathodic current density of 15 mA/cm^2) in an electrolyte consisting of 2:1 mixture of glycerol and H_3PO_4 [59]. Different charging times were chosen according to the objective of the current study.

Regarding the samples for microcantilever and micropillar tests, in-situ hydrogen charging was conducted in a miniaturized three-electrode electrochemical charging cell at room temperature. A platinum wire was used as the counter electrode and $Hg/HgSO_4$ reference electrode (0.6 M K_2SO_4) was chosen for in-situ charging. Details of the electrochemical cell can be found in Ref. [129]. The electrolyte used for in-situ hydrogen charging consists of glycerol-based borax with 0.002 mol/L $Na_2S_2O_3$ to promote hydrogen adsorption [157]. In microcantilever bending test, two different charging potentials were applied to investigate the mechanical property degradation with different hydrogen content, i.e. -1400 mV (40 h) and -1600 mV (20 h). In micropillar compression test, pillars were charged for 5 h at a much higher potential of -2150 mV before the test to introduce sufficient hydrogen. In both tests, the electrolyte was changed every 30 min to avoid any disturbance from hydrogen bubbles. The electrolytes used for tensile test and micro-scale test can preserve the surface integrity, which offers the possibility for direct surface observation after tests.

4.4 Slow strain rate tensile test

Ex-situ slow strain rate tensile test (SSRT) was performed at a constant nominal strain rate of 2×10^{-5} s^{-1} on a Kammrath & Weiss tensile/compression module inside SEM (Quanta FEG 650, Thermo Fisher Scientific Inc., USA) for a real-time observation. The specimens were loaded to fracture in both vacuum condition (4.7×10^{-3} Pa) and hydrogen-charged conditions. The time-lag between finish hydrogen charging and start testing was controlled within 30 min. Hydrogen loss within this period was neglected due to the low hydrogen diffusivity in FCC metals.

4.5 Micro-scale cantilever bending and pillar compression tests

Both micro-scale cantilever bending and pillar compression tests were conducted on a Hysitron TI 950TriboIndenter. For microcantilever bending, a conical tip with a nominal tip radius of 0.5 μm was used. The load function was designed by integrating partial-loading-unloading sequences after yielding at a loading rate of 2 nm/s [45]. For micropillar compression, a diamond flat-punch with a diameter of 5.5 μm was chosen. All pillars were compressed in a displacement-control mode at a displacement rate of 20 nm/s followed by a holding time of 1 s before unloading. Both tests were performed in hydrogen-free and hydrogen-charged conditions.

4.6 Post-mortem analysis

4.6.1 Scanning electron microscopy and electron backscatter diffraction

Scanning electron microscopy (SEM) was applied to analyze the sample surface microstructure, fractography, deformation morphology and cross-section cracks. Similarly, electron backscatter diffraction (EBSD) was used to investigate the microstructure, misorientation and plastic deformation on the loaded samples. The collected signals from NORDIF camera were analyzed by the OIM software. For cross-section inspections using SEM and EBSD, special treatment was conducted. In order to study the possible damage below the fracture surface for tensile samples, the fractured parts were electrodeposited with nickel to provide appropriate edge retention. For visualizing plastic deformation inside microcantilevers and micropillars, FIB thinning at 30 kV from high current (2.8 nA) to low current (90 pA) was conducted on the cross-sections.

4.6.2 Electron channeling contrast imaging

The electron channeling contrast imaging (ECCI) technique was employed to reveal deformation structure with a resolution down to dislocation level. The SEM was installed with a backscatter electron (BSE) detector to collect BSE signals from the sample surface. In the current study, electron channeling contrast (ECC) micrographs were collected at an accelerating voltage of 30 kV and a working distance about 6 mm at a proper tilting and rotation angle.

4.6.3 Transmission Kikuchi diffraction

Transmission Kikuchi diffraction (TKD), also known as transmission EBSD (t-EBSD), has a significant improvement in the spatial resolution up to one order of magnitude compared to normal EBSD [158]. Unlike the normal EBSD with a sample tilt angle by 70° towards the detector, the tilt angle for TKD sample is about 20°. TKD is normally conducted on thin foil which has to be transparent to electrons, e.g. TEM lamella, free standing films and crystalline nanoparticles. This technique offers a better resolution of plastic deformation. In the present study, thin lamellae of tested cantilevers and pillars were prepared using FIB thinning process until the sample thickness reached to about 200 nm. TKD was performed inside SEM at an accelerating voltage of 30 kV and a tilt angle of 20°. The step size varies from 10 to 20 nm. The collected signals from NORDIF camera were analyzed by the OIM software.

4.6.4 Thermal desorption spectroscopy

To determine hydrogen content in the hydrogen-charged samples, thermal desorption spectroscopy (TDS) test was conducted on a Bruker G4 PHONIX DH analyzer with a mass spectroscopy detector. The current flow of hydrogen was precisely recorded by the mass spectrometer and presented as a function of temperature and time. The heating range varies from 50 °C-800 °C and the heating rate was chosen to be 10 °C/min or 25 °C/min according to different charging conditions. The dwell time before the test after hydrogen charging was controlled within 25 min, thus hydrogen diffusing out is neglected.

4.6.5 Transmission electron microscopy

In this study, to visualize dislocation structures on the cross-sections of microcantilevers deformed in air and hydrogen-charged conditions, transmission electron microscopy (TEM) characterization was conducted on a cold FEG Joel, JEM-2100 TEM, operating at 200 kV.

4.6.6 Atom probe tomography

In this study, to gain deep understanding of the strengthening phases and GB precipitates in Alloy 718 and Alloy 725, atom probe tomography (APT) technique was employed, which enables a three-dimensional mapping of the atom distribution and chemical composition. The needle shaped APT samples were prepared using FEI® Helios™ Nanolab™ 660 FIB instrument. APT characterization was performed on Local Electrode Atom Probe (LEAP) 4000X HR instrument, operated in pulsed laser mode (pulse frequency 200 kHz), at a base temperature of 60 K. The three-dimensional reconstructions were carried out using commercial software Integrated Visualization and Analysis Software package (IVAS, CAMECA Scientific Instruments, Madison, WI).

5 Summary of main results and discussion

This chapter summarizes the main results obtained in this PhD thesis based on four papers that have been published in or that are to be submitted to peer-reviewed journals. Full-tests of these papers are provided in Part II of this PhD thesis.

5.1 The effect of electrochemical charging on the microstructure change of Alloy 718 (Paper I)

Precipitation-hardened nickel-based superalloys are widely used for subsea oil and gas (O&G) industries. However, they are susceptible to hydrogen embrittlement (HE) when they are used in the hydrogenated environment. Although many research works have focused on the mechanisms for the intergranular (IG) and transgranular (TG) failures in these alloys, the effect of hydrogen charging method, particularly electrochemical charging, is rarely documented. Thus far, most of the solutions used for hydrogen charging have been water-based, which could cause corrosion and conceal the useful information of charging. Therefore, a glycerol-based electrolyte was used in this study to preserve the surface integrity of the alloy, which enabled a direct observation of the microstructure change after charging.

By choosing different charging time that ranges from 20 h to 168 h, the results show that electrochemical hydrogen charging could cause slip lines. Additionally, surface and subsurface cracks could be observed when the charging time reached 60 h (see Graphical abstract 5.1(a)). In this study, 40 h charging was the threshold for hydrogen-induced surface cracking in the charging conditions described in paper I, where the electrolyte consisted of a mixture of glycerol and H_3PO_4 and a constant potential of -1050 mV at 75 °C was applied. Due to the low diffusivity of hydrogen in Alloy 718, it is reasonable to infer that a gradient in hydrogen concentration from the edge to the inner region was developed during electrochemical charging. And the internal stress due to hydrogen distribution inhomogeneity plays a critical role. Therefore, hydrogen concentration gradient beneath the sample surface was simulated according to the Fick's second law. The result is shown in Graphical abstract 5.1(b), where a steep concentration gradient was generated along the sample thickness.

To give an estimation of the internal stress induced by the electrochemical charging, the volume expansion by hydrogen was calculated using eq. (5.1):

$$\frac{\Delta V}{V_0} = \frac{H_a}{M_a}\frac{\Delta v}{\Omega} \tag{5.1}$$

where H_a/M_a represents the atomic ratio between hydrogen and metal near to the surface during charging, Δv is the volume change per hydrogen atom, and Ω is the mean volume of metal atom. H_a/M_a relates to the surface hydrogen concentration using eq. (5.2):

$$H_a/M_a = \frac{C_0 \times N_A/M_H}{(10^6 - C_0) \times N_A/M_A} \tag{5.2}$$

where N_A is the Avogadro constant, M_H and M_A are the molar mass of hydrogen (1 g/mol) and the studied Alloy 718 (59.5 g/mol), respectively. Additionally, hydrogen surface concentration C_0 can be estimated from the total hydrogen concentration in the sample C_M using eq. (5.3):

$$C_0 = \frac{\omega C_M}{4}\sqrt{\frac{\pi}{Dt}} \tag{5.3}$$

where ω equals to the sample thickness, D is the hydrogen diffusion constant of Alloy 718 (2.05×10^{-14} m^2/s). By performing thermal desorption spectroscopy (TDS) test on 20 h charged sample, the total dissolved hydrogen equaled to 36.5 weight ppm (wppm). Thus, the internal stress near the surface was estimated by the volume expansion times the bulk modulus of Alloy 718, which yielded a value of 665.7 MPa. This value is higher than the critical resolved shear stress (218.9 MPa) for slip in a single crystal that is deduced from the measured polycrystalline yield stress (669.8 MPa for 20 h charging, presented in paper I) using the Taylor factor (3.06). The above calculations confirm that the internal stress generated during electrochemical charging is high enough to be the driving force for the hydrogen-induced damages.

This is the first time that electrochemical hydrogen charging alone could cause slip lines and cracks in Alloy 718 is reported. Those damages were proven to invade the mechanical properties of this alloy upon loading (paper I). Since hydrogen diffusion is sluggish in nickel-based superalloys and austenitic steels, it is considered as a phenomenon that can happen when the materials are exposed to harsh hydrogenated environments. It is important to pay attention to this behavior when dealing with failures in hydrogen-related mechanical tests, since those damages are potential sources of

cracking that can be easily ignored by researchers. In future HE studies, it is therefore recommended to perform neat tests with all the information observable by choosing a proper hydrogen charging media, e.g. considering that glycerol-based electrolyte is a proper replacement for aqueous-based solution, especially when dealing with small-scale tests, as proposed in Ref .

Graphical abstract 5.1:

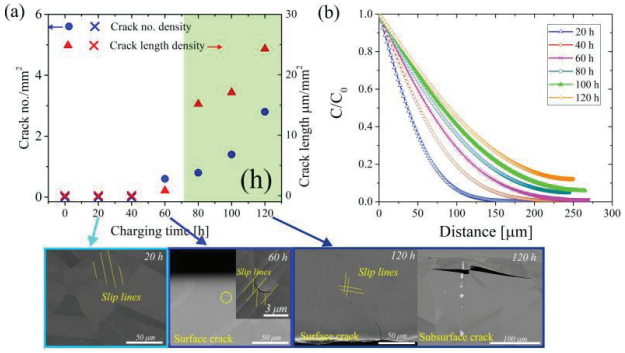

5.2 Comparison of hydrogen embrittlement (HE) behavior between Alloy 718 and Alloy 725 (Paper II)

Alloy 718 and Alloy 725 are commonly used materials in the O&G industries. Due to their differentiation in chemical compositions and heat treatments, they exhibit different mechanical properties and HE behavior. In Paper II, the effect of hydrogen on mechanical degradation of two precipitation-hardened nickel-based superalloys, i.e. Alloy 718 and Alloy 725, was studied. From section 5.1, we know that 40 h is the threshold time for electrochemical charging-induced surface cracks. Thus, in this study, the electrochemical charging time was controlled within 40 h to avoid any damage by the charging process. The same charging process was applied to both alloys. Slow strain rate tensile test (SSRT) was conducted to study the mechanical properties of each alloy. Microstructure and post-mortem characterization of the alloys were realized by different microscopy techniques, i.e. scanning electron microscopy (SEM), electron backscatter diffraction (EBSD) and atom probe tomography (APT).

APT and SEM analysis showed that Alloy 718 matrix contained γ’ and γ’’ strengthening phases and only a small fraction of GBs was covered with δ phase. In contrast, Alloy 725 matrix contained only γ’’ precipitates and a large fraction of GBs was decorated by the (Cr, Mo)-rich precipitates. The decoration of (Cr, Mo)-rich precipitates curved the GBs into irregular shapes.

In the hydrogen-free condition, SSRT results showed that Alloy 725 exhibited higher yield strength and ultimate tensile strength than Alloy 718 (see Graphical abstract 5.2(a)). This attributes to the reduced size of the strengthening phase in Alloy 725. Fractography showed that Alloy 718 was failed through microvoid coalescence (MVC) ductile fracture mode, while Alloy 725 was failed through a combination of MVC and IG cracking.

With the presence of hydrogen, Alloy 725 was more susceptible to hydrogen embrittlement compared to Alloy 718 (see Graphical abstract 5.2(a)). Both IG and TG cracking features were detected in Alloy 718, while IG failure dominated in Alloy 725 (see Graphical abstract 5.2(b)-(c)). The cross-section analysis also showed clear IG cracking in Alloy 725. The differentiation in mechanical responses and HE behavior were attributed to their different microstructures.

Compared to Alloy 718, the dense decoration of (Cr, Mo)-rich precipitates along the GBs of Alloy 725 (see Graphical abstract 5.2(c2)-(c3)) changed the GB structures such that the lattice field

became distorted. Upon deformation, dislocations piled up but were not able to transmit through or be absorbed by the disordered structures. Therefore, the local stress was elevated, and the formation of micro-cracks was promoted. This behavior was more pronounced with hydrogen, since trapped hydrogen lowered the defects formation energy and promoted the generation of vacancies. As a result, Alloy 725 was more susceptible to IG cracking during plastic deformation with a relatively low ductility than Alloy 718.

It is difficult to quantify the local stress state around the precipitate-decorated GBs by performing tensile test alone. In order to study the local deformation behavior, in-situ small-scale tests combined with advanced characterization techniques, i.e. focused ion beam (FIB) milling and transmission electron microscopy (TEM), are needed for further study. However, this study is important as it points out what should be the concerning factors when designing HE tolerant alloys.

Graphical abstract 5.2:

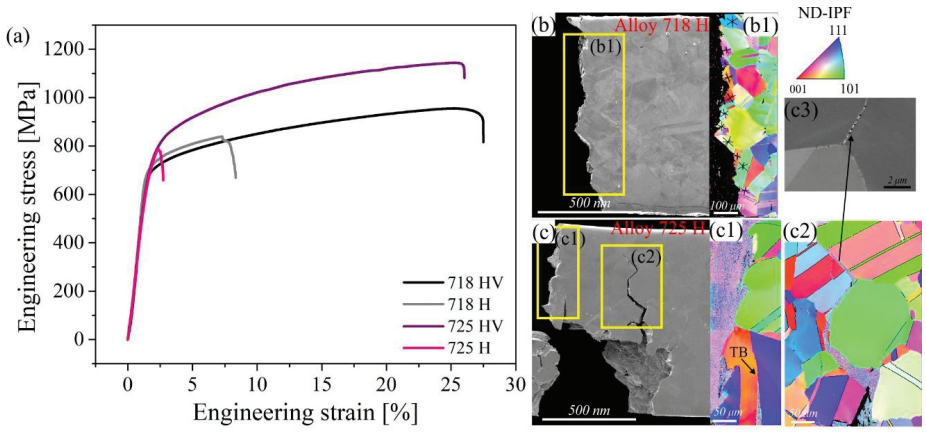

5.3 Hydrogen-assisted intergranular cracking (IG) revisited by slow strain rate tensile test (SSRT) and in-situ micropillars compression test (Paper I and III)

Hydrogen-assisted IG cracking was normally observed at delta (δ) phase decorated GBs, GB triple junctions and high-angle GBs in nickel-based superalloys. However, the cracking mechanism of no-precipitate-decorated GBs remains unknow. And the measurement of misorientation alone, which is based on the two-dimensional information, is far from being adequate due to the complex structure of GBs and the synergistic effect of adjacent grains upon deformation. Therefore, in Paper I, the STRONG (Slip Transfer Resistance of Neighbouring Grains) model was adopted with the intent of uncovering the relationship between slip system compatibility and hydrogen-assisted IG cracking behavior. Following the electrochemical charging procedures described in section 5.1, SSRT was performed in the precipitation-hardened Alloy 718. The GB trace information was collected using FIB by cutting trenches across the GBs. Basically, in the STRONG model, the resistance of GB to slip transmission can be expressed as eq. (5.4):

$$\omega_{ij} = 1 - \cos\alpha_{ij} \cdot \cos\beta_{ij} \tag{5.4}$$

where α is the angle between the intersection lines of the active slip plane in each grain with the GB and β is the angle between the corresponding slip directions in adjacent grains. Comparing the results of several cracked and non-cracked GBs (the ones without the decoration of precipitates), we were able to show that the GB transferability of dislocations is an important factor determining the tendency for IG cracking. In the presence of hydrogen, GBs with high resistance to slip transmission increased the probability for crack initiation upon loading due to the synergistic effect of hydrogen and local stress incompatibility, and GBs with lower resistance to slip transmission were less susceptible to cracking. This study provides new insights in understanding the hydrogen-assisted IG cracking mechanisms. This approach can be used in not only nickel-based alloys, but also other steels and alloys that suffer from hydrogen-induced IG failures.

However, the complex nature of GBs makes it difficult to disentangle the role of different GB types in the HE effects. Thus, small scale tests including only specific GBs are necessary. In Paper III, in-situ micropillar compression tests containing three types of GBs, i.e. low-angle GB (LAGB), high-angle GB (HAGB) and twin boundary (TB), were performed on a nickel-based Alloy 725 to investigate the HE behavior of each GB type. To eliminate the influence of matrix and GB

precipitates, the solution annealed sample was used as the studied material. The micropillars were fabricated using FIB. The in-situ electrochemical compression test was performed with Hysitron TI950 TriboIndenter integrated with a miniaturized three-electrode electrochemical cell. The electrolyte consisted of a glycerol-based borax solution with 0.002 mol/L $Na_2S_2O_3$ to assist hydrogen absorption. This electrolyte was proven to keep the surface integrity during the whole test. Afterwards, a thorough characterization of the deformed pillars was performed by using SEM and high-resolution transmission EBSD (t-EBSD).

Micropillar compression results showed that the presence of hydrogen drastically increased the stress and strain hardening of pillars regardless of the GB types (see the example in Graphical abstract 5.3(a)). Hydrogen enhances dislocation multiplication and interactions were proposed to contribute to the stress elevation. Other possible factors include hydrogen-enhanced lattice friction and hydrogen pins dislocation motion.

A more detailed characterization by conducting t-EBSD illustrated that hydrogen had no obvious effect on the dislocation activities at the TBs. In contrast, for micropillars containing HAGBs and LAGBs, stress concentration areas with higher dislocation densities along the GBs were observed (see Graphical abstract 5.3(c2)-(c3) for LAGB). In comparison, dislocations could transmit smoothly through the GBs in the hydrogen-free condition (see Graphical abstract 5.3(b2)-(b3)). It means that the presence of hydrogen transformed the GB into a barrier for dislocation transmission. This phenomenon also contributed to the elevated stress in the stress-strain curves. This is the first experimental study showing that hydrogen could hinder dislocation transmission at both HAGBs and LAGBs. One related explanation might be that hydrogen disordered the atomic structure during dislocation-GB interactions and eased the formation of vacancies. Hydrogen-vacancy complex was relatively stable that could effectively pin dislocations from motion or penetration through the GBs. Thus, a higher stress was needed to unpin dislocations or to generate new dislocations to accommodate the plastic deformation. To experimentally verify this assumption, a more elaborated test with the application of high-resolution TEM is needed. Nevertheless, this study still provides valuable insights into the mechanisms for IG cracking in nickel-based superalloys.

Graphical abstract 5.3:

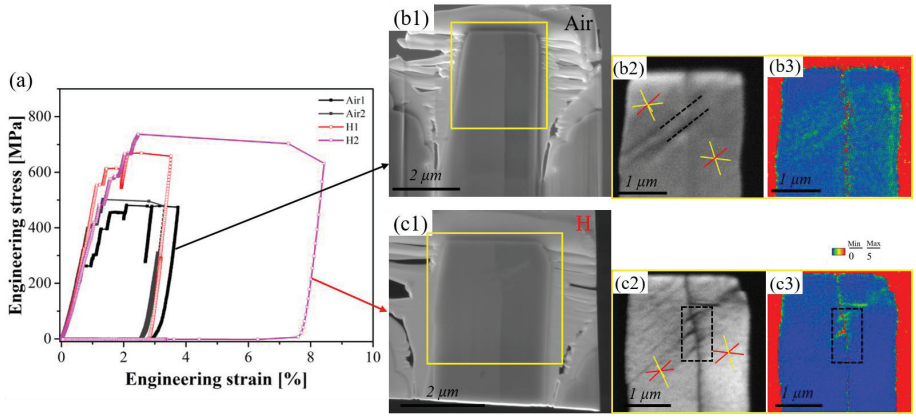

5.4 Hydrogen-assisted transgranular cracking (TG) revisited by SSRT and in-situ electrochemical microcantilever bending test (Paper I and IV)

In Paper I, it was shown that electrochemical hydrogen charging could cause pre-damages when the charging time is higher than 60 h. After performing SSRT on the charged samples, a reduction of yield strength and an increment of embrittlement factor were observed with prolonged charging time. By analyzing surface cracks and the fractography of the failed samples, two main reasons for the formation of TG cracks were proposed: (a) pre-damages caused by electrochemical charging before loading promoted the initiation and propagation of TG cracks, which highlighted again the importance of hydrogen charging; (b) intersections of dislocation slip bands on {111} planes act as stress concentrators that attracted hydrogen and led to void nucleation, which finally resulted in cracking.

To further visualize the local cracking behavior at stress concentrated areas, Paper IV covered the in-situ micro-cantilever bending test that was conducted on a face-centered cubic (FCC) structured interstitial high entropy alloy (HEA), a model material of which nominal composition (at. %) is $Co_{19.9}Cr_{19.9}Fe_{19.9}Mn_{19.9}Ni_{19.9}C_{0.5}$. All the cantilevers were pre-notched to study the plane of {111} with the lowest surface energy. Mechanical testing in hydrogen-free and hydrogen-charged conditions were performed and compared. Hydrogen charging in two cathodic polarization conditions (-1400 mV and -1600 mV) were selected to study the effect of hydrogen content on the mechanical degradation of cantilevers. The electrolyte used for micro-cantilever bending test was the same as in micropillar compression test in section 5.3. Post-mortem characterization on the deformation behavior was realized through a combination of SEM, t-EBSD and high-resolution TEM.

Load-displacement curves showed that the flow stress of cantilevers bent in hydrogen-charged conditions decreased gradually after several loading-unloading cycles compared to those bent in the hydrogen-free condition (see Graphical abstract 5.4(a)). To study the most noticeable effect of hydrogen, electrochemical charging at the potential of -1600 mV was selected for the post-mortem beam cross-section analysis. In the hydrogen-free condition, notch blunting accompanied by a large plastic zone was observed (see Graphical abstract 5.4(b1)-(b2)). Three slip systems were activated to accommodate the plastic deformation. In comparison, hydrogen-assisted cracking bisecting two {111} slip planes with a confined plastic zone was detected in the hydrogenated

cantilevers (see Graphical abstract 5.4(c1)-(c2)). The final cracking path was aligned with (001) plane trace. The initiation and propagation of micro-cracks were attributed to the synergistic effect of hydrogen-assisted defects formation and the pinning effect of hydrogen to dislocation motion, which caused the local stress intensity to reach to the critical value for micro-crack formation.

This study provides insights into the hydrogen-dislocation interactions during mechanical loading, which is an effective approach to unravel the underlying HE mechanism at small-scale level. To further understand the effect of grain orientations, different crack systems should be designed and tested in the future HE studies.

Graphical abstract 5.4:

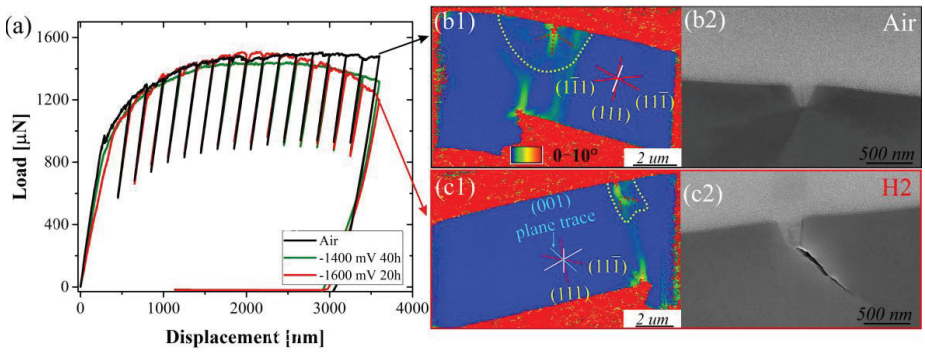

6 Conclusions and future work

The goal of this PhD thesis was to dig into the mechanisms for hydrogen-assisted failure in nickel-based superalloys using advanced testing and characterization techniques. Two types of nickel-based superalloys and a high entropy alloy were thoroughly studied by conducting slow train rate tensile test (SSRT), micropillar compression and microcantilever bending test in both hydrogen-free and hydrogen-charged conditions. Firstly, the effect of electrochemical charging on the microstructure change of nickel-based superalloy 718 was studied by considering the stress concentration gradient beneath the metal surface. Afterwards, novel ideas explaining the generation of intergranular (IG) and transgranular (TG) fracture were proposed. By choosing a proper electrochemical charging condition to avoid any damage on the metal surface, hydrogen effect on the mechanical degradation behavior of Alloy 718 and Alloy 725 were studied and compared. The major conclusions can be summarized as follows:

- In Alloy 718, electrochemical charging alone could cause slip lines, surface and subsurface cracks, which were the cracking sources during mechanical loading and assisted the pre-mature failure. Those pre-damages were proposed to be induced by the internal stress due to hydrogen concentration gradient near the surface.
- The presence of hydrogen has a detrimental effect on the mechanical properties of both Alloy 718 and Alloy 725. Alloy 725 showed less resistance to hydrogen embrittlement compared to Alloy 718. Different from Alloy 718 where a mixture of IG and TG cracking feature were observed, Alloy 725 showed IG fracture dominant behavior. Such differentiation originates from their unique microstructures. Compared to the grain boundaries (GBs) with a small fraction of δ phase in Alloy 718, most of the GBs in Alloy 725 were decorated with (Cr, Mo)-rich precipitates, which disordered the GB structures and assisted the initiation of IG cracks and early fracture.
- The GB transferability of dislocations is an important factor determining the propensity for IG cracking. In the hydrogen-charged condition, GBs with high resistance to dislocation slip transmission increased the probability for crack initiation upon loading due to the synergistic effect of hydrogen and local stress incompatibility. In contrast, GBs with lower resistance to slip transmission were less susceptible to cracking. In-situ micropillar compression tests showed that, both low-angle GB and high-angle GB exhibited a suppression effect on

dislocation transmission in presence of hydrogen and resulted in a raise of local stress concentration along the GBs. This phenomenon provides valuable insights into the mechanisms for intergranular cracking in nickel-based superalloys.

- The generation of TG cracks in presence of hydrogen could be attributed to several aspects: (a) pre-damages caused during electrochemical charging promoted the initiation and propagation of TG cracks; (b) intersections of dislocation slip bands on {111} planes were the stress concentrators that attracted hydrogen and led to void nucleation, and finally to cracking; (c) the nucleation of micro-cracks could also be attributed to hydrogen-assisted defects formation and the pinning effect of hydrogen to dislocation motion, which led to an elevation in local stress intensity to reach to the critical value for continuous micro-cracks formation. As a result, a localized plasticity was observed.

The current PhD work provides insights into the mechanisms for the hydrogen-assisted cracking in nickel-based superalloys by proposing several novel ideas. However, due to the limitation of time and the available characterization techniques, there are still some unsolved questions that could be focused in the future research of hydrogen embrittlement (HE) in nickel-based alloys:

- The interaction of dislocations with GB involving the formation of defects in presence of hydrogen needs to be characterized by higher resolution techniques, e.g. transmission electron microscopy (TEM).
- To statistically resolve the effect of GB type and misorientation on hydrogen susceptibility, a number of tests on different GBs should be performed. Besides micro-pillar compression test, micro-scale tensile test including specific GB is another good option.
- The role of strengthening phases γ’ and γ’’ on dislocation multiplication and interactions in presence of hydrogen needs further investigation. Also, the influence of fine precipitate size on the hydrogen trapping behavior should be considered.
- Since GB precipitates are deleterious to alloy’s mechanical properties, how to eliminate them using alloy elements or heat treatments in the frame of GB engineering is of vital importance for future applications in the O&G industry.

7 Reference

[1] M. Iannuzzi, A. Barnoush, R. Johnsen, Materials and corrosion trends in offshore and subsea oil and gas production, npj Materials Degradation 1(1) (2017) 2.
[2] S.P. Lynch, Failures of engineering components due to environmentally assisted cracking, Practical Failure Analysis 3(5) (2003) 33-42.
[3] B. Lee, R.L. Karkkainen, Failure investigation of hydrogen induced cracking of stabilator skin in jet aircraft, Eng Fail Anal 92 (2018) 182-194.
[4] W.H. Johnson, On Some Remarkable Changes Produced in Iron and Steel by the Action of Hydrogen and Acids, Proc. Royal Soc. Lond. 23 (1874) 168-179.
[5] P.D. Hicks, Altstetter, C.J. , Comparison of internal hydrogen embrittlement of superalloys 718 and 625, JOM (1991) pp 635–651.
[6] W.J. Boesch, H.B. Canada, Precipitation Reactions and Stability of Ni3cb in Inconel Alloy-718, Jom-J Min Met Mat S 21(10) (1969) 34-&.
[7] I.M. Robertson, H.K. Birnbaum, An Hvem Study of Hydrogen Effects on the Deformation and Fracture of Nickel, Acta Metall. 34(3) (1986) 353-366.
[8] J. Xu, X.K. Sun, Q.Q. Liu, W.X. Chen, Hydrogen permeation behavior in In718 and Gh761 superalloys, Metall. Mater. Trans. A 25(3) (1994) 539-544.
[9] A. Turnbull, R.G. Ballinger, I.S. Hwang, M.M. Morra, M. Psailadombrowski, R.M. Gates, Hydrogen Transport in Nickel-Base Alloys, Metallurgical Transactions a-Physical Metallurgy and Materials Science 23(12) (1992) 3231-3244.
[10] A. Hirose, Y. Arita, Y. Nakanishi, K.F. Kobayashi, Decrease in hydrogen embrittlement sensitivity of INCONEL 718 by laser surface softening, Materials Science and Engineering a-Structural Materials Properties Microstructure and Processing 219(1-2) (1996) 71-79.
[11] J. Chene, A.M. Brass, Role of temperature and strain rate on the hydrogen-induced intergranular rupture in alloy 600, Metall. Mater. Trans. A 35a(2) (2004) 457-464.
[12] L.F. Liu, K. Tanaka, A. Hirose, K.F. Kobayashi, Effects of precipitation phases on the hydrogen embrittlement sensitivity of Inconel 718, Science and Technology of Advanced Materials 3(4) (2002) 335-344.
[13] C.M. Kuo, Y.T. Yang, H.Y. Bor, C.N. Wei, C.C. Tai, Aging effects on the microstructure and creep behavior of Inconel 718 superalloy, Materials Science and Engineering: A 510-511 (2009) 289-294.
[14] K. Prasad, R. Sarkar, P. Ghosal, V. Kumar, Tensile deformation behaviour of forged disc of IN 718 superalloy at 650°C, Mater. Des. 31(9) (2010) 4502-4507.
[15] F. Galliano, E. Andrieu, C. Blanc, J.M. Cloue, D. Connetable, G. Odemer, Effect of trapping and temperature on the hydrogen embrittlement susceptibility of alloy 718, Materials Science and Engineering a-Structural Materials Properties Microstructure and Processing 611 (2014) 370-382.
[16] F. Galliano, E. Andrieu, J.-M. Cloué, G. Odemer, C. Blanc, Effect of temperature on hydrogen embrittlement susceptibility of alloy 718 in Light Water Reactor environment, Int. J. Hydrog. Energy 42(33) (2017) 21371-21378.
[17] V. Demetriou, J.D. Robson, M. Preuss, R. Morana, Effect of hydrogen on the mechanical properties of alloy 945X (UNS N09945) and influence of microstructural features, Mater. Sci. Eng. A 684 (2017) 423-434.
[18] Z.B. Zhang, G. Obasi, R. Morana, M. Preuss, Hydrogen assisted crack initiation and propagation in a nickel-based superalloy, Acta Mater. 113 (2016) 272-283.

[19] Z. Tarzimoghadam, D. Ponge, J. Klower, D. Raabe, Hydrogen-assisted failure in Ni-based superalloy 718 studied under in situ hydrogen charging: The role of localized deformation in crack propagation, Acta Mater. 128 (2017) 365-374.
[20] M.C. Rezende, L.S. Araujo, S.B. Gabriel, D.S. dos Santos, L.H. de Almeida, Hydrogen embrittlement in nickel-based superalloy 718: Relationship between γ′ + γ″ precipitation and the fracture mode, Int. J. Hydrog. Energy 40(47) (2015) 17075-17083.
[21] Z.B. Zhang, K.L. Moore, G. McMahon, R. Morana, M. Preuss, On the role of precipitates in hydrogen trapping and hydrogen embrittlement of a nickel-based superalloy, Corros. Sci. 146 (2019) 58-69.
[22] V. Demetriou, J.D. Robson, M. Preuss, R. Morana, Study of the effect of hydrogen charging on the tensile properties and microstructure of four variant heat treatments of nickel alloy 718, Int. J. Hydrog. Energy (2017).
[23] L.F. Liu, C.Q. Zhai, C. Lu, W.J. Ding, A. Hirose, K.F. Kobayashi, Study of the effect of delta phase on hydrogen embrittlement of Inconel 718 by notch tensile tests, Corros. Sci. 47(2) (2005) 355-367.
[24] M.P. LaCoursiere, D.K. Aidun, D.J. Morrison, Slow Strain Rate Testing for Hydrogen Embrittlement Susceptibility of Alloy 718 in Substitute Ocean Water, J. Mater. Eng. Perform. 26(5) (2017) 2337-2345.
[25] L. Fournier, D. Delafosse, T. Magnin, Cathodic hydrogen embrittlement in alloy 718, Mater. Sci. Eng. A 269(1-2) (1999) 111-119.
[26] F. Lecoester, J. Chene, D. Noel, Hydrogen embrittlement of the Ni-base Alloy 600 correlated with hydrogen transport by dislocations, Materials Science and Engineering a-Structural Materials Properties Microstructure and Processing 262(1-2) (1999) 173-183.
[27] S.K. Lawrence, Y. Yagodzinskyy, H. Hänninen, E. Korhonen, F. Tuomisto, Z.D. Harris, B.P. Somerday, Effects of grain size and deformation temperature on hydrogen-enhanced vacancy formation in Ni alloys, Acta Mater. 128 (2017) 218-226.
[28] S. Jothi, S.V. Merzlikin, T.N. Croft, J. Andersson, S.G.R. Brown, An investigation of micro-mechanisms in hydrogen induced cracking in nickel-based superalloy 718, J. Alloys Compd. 664 (2016) 664-681.
[29] J.P. Hanson, A. Bagri, J. Lind, P. Kenesei, R.M. Suter, S. Gradecak, M.J. Demkowicz, Crystallographic character of grain boundaries resistant to hydrogen-assisted fracture in Ni-base alloy 725, Nat. Commun. 9 (2018).
[30] Z. Zhang, G. Obasi, R. Morana, M. Preuss, In-situ observation of hydrogen induced crack initiation in a nickel-based superalloy, Scr. Mater. 140 (2017) 40-44.
[31] S. Bechtle, M. Kumar, B.P. Somerday, M.E. Launey, R.O. Ritchie, Grain-boundary engineering markedly reduces susceptibility to intergranular hydrogen embrittlement in metallic materials, Acta Mater. 57(14) (2009) 4148-4157.
[32] S. Brian, Offshore bolt failures provide chance to display safety culture, Offshore (2016).
[33] D.P. Escobar, T. Depover, L. Duprez, K. Verbeken, M. Verhaege, Combined thermal desorption spectroscopy, differential scanning calorimetry, scanning electron microscopy and X-ray diffraction study of hydrogen trapping in cold deformed TRIP steel, Acta Mater. 60(6-7) (2012) 2593-2605.
[34] T. Depover, D.P. Escobar, E. Wallaert, Z. Zermout, K. Verbeken, Effect of hydrogen charging on the mechanical properties of advanced high strength steels, Int. J. Hydrog. Energy 39(9) (2014) 4647-4656.

[35] T. Depover, E. Wallaert, K. Verbeken, Fractographic analysis of the role of hydrogen diffusion on the hydrogen embrittlement susceptibility of DP steel, Materials Science and Engineering a-Structural Materials Properties Microstructure and Processing 649 (2016) 201-208.
[36] M. Sundararaman, P. Mukhopadhyay, S. Banerjee, Deformation-Behavior of Gamma" Strengthened Inconel-718, Acta Metall. 36(4) (1988) 847-864.
[37] G.A. Young, J.R. Scully, Evidence that carbide precipitation produces hydrogen traps in Ni-17Cr-8Fe alloys, Scr. Mater. 36(6) (1997) 713-719.
[38] H. Andersson, In-situ SEM study of fatigue crack growth behaviour in IN718, Int. J. Fatigue 26(3) (2004) 211-219.
[39] D.H. Ping, Y.F. Gu, C.Y. Cui, H. Harada, Grain boundary segregation in a Ni–Fe-based (Alloy 718) superalloy, Materials Science and Engineering: A 456(1-2) (2007) 99-102.
[40] Y. Yao, X. Pang, K. Gao, Investigation on hydrogen induced cracking behaviors of Ni-base alloy, Int. J. Hydrog. Energy 36(9) (2011) 5729-5738.
[41] S. Chen, M. Zhao, L. Rong, Hydrogen-induced cracking behavior of twin boundary in γ′ phase strengthened Fe–Ni based austenitic alloys, Materials Science and Engineering: A 561 (2013) 7-12.
[42] Z. Li, K.G. Pradeep, Y. Deng, D. Raabe, C.C. Tasan, Metastable high-entropy dual-phase alloys overcome the strength-ductility trade-off, Nature 534(7606) (2016) 227-30.
[43] H. Luo, Z. Li, D. Raabe, Hydrogen enhances strength and ductility of an equiatomic high-entropy alloy, Sci. Rep. 7(1) (2017) 9892.
[44] H. Luo, W. Lu, X. Fang, D. Ponge, Z. Li, D. Raabe, Beating hydrogen with its own weapon: Nano-twin gradients enhance embrittlement resistance of a high-entropy alloy, Mater. Today (2018).
[45] X. Lu, D. Wang, Z. Li, Y. Deng, A. Barnoush, Hydrogen susceptibility of an interstitial equimolar high-entropy alloy revealed by in-situ electrochemical microcantilever bending test, Materials Science and Engineering: A 762 (2019) 138114.
[46] D. Wang, X. Lu, Y. Deng, D. Wan, Z. Li, A. Barnoush, Effect of hydrogen-induced surface steps on the nanomechanical behavior of a CoCrFeMnNi high-entropy alloy revealed by in-situ electrochemical nanoindentation, Intermetallics 114 (2019) 106605.
[47] E. Tal-Gutelmacher, D. Eliezer, The hydrogen embrittlement of titanium-based alloys, Jom-Us 57(9) (2005) 46-49.
[48] E. Tal-Gutelmacher, D. Eliezer, Hydrogen-assisted degradation of titanium based alloys, Mater. Trans. 45(5) (2004) 1594-1600.
[49] H.K. Birnbaum, Hydrogen Related Fracture of Metals, in: R.M. Latanision, J.R. Pickens (Eds.), Atomistics of Fracture, Springer US, Boston, MA, 1983, pp. 733-769.
[50] H.K. Birnbaum, Mechanisms of hydrogen related fracture of metals, Illinois University at Urbana department of materials science and engineering, 1989.
[51] H.K. Birnbaum, P. Sofronis, Hydrogen-enhanced localized plasticity - a mechanism for hydrogen-related fracture, Mater. Sci. Eng. A 176(1-2) (1994) 191-202.
[52] S.P. Lynch, Interpreting hydrogen-induced fracture surfaces in terms of deformation processes: A new approach, Scr. Mater. 65(10) (2011) 851-854.
[53] M.L. Martin, B.P. Somerday, R.O. Ritchie, P. Sofronis, I.M. Robertson, Hydrogen-induced intergranular failure in nickel revisited, Acta Mater. 60(6-7) (2012) 2739-2745.
[54] I.M. Robertson, P. Sofronis, A. Nagao, M.L. Martin, S. Wang, D.W. Gross, K.E. Nygren, Hydrogen Embrittlement Understood, Metallurgical and Materials Transactions B 46(3) (2015) 1085-1103.

[55] M.L. Martin, M. Dadfarnia, A. Nagao, S. Wang, P. Sofronis, Enumeration of the hydrogen-enhanced localized plasticity mechanism for hydrogen embrittlement in structural materials, Acta Mater. 165 (2019) 734-750.
[56] A. Barnoush, H. Vehoff, In situ electrochemical nanoindentation: A technique for local examination of hydrogen embrittlement, Corros. Sci. 50(1) (2008) 259-267.
[57] Y. Deng, T. Hajilou, D. Wan, N. Kheradmand, A. Barnoush, In-situ micro-cantilever bending test in environmental scanning electron microscope: Real time observation of hydrogen enhanced cracking, Scr. Mater. 127 (2017) 19-23.
[58] Y. Deng, T. Hajilou, A. Barnoush, Hydrogen-enhanced cracking revealed by in situ micro-cantilever bending test inside environmental scanning electron microscope, Philos. Trans. Royal Soc. A 375(2098) (2017).
[59] R. Kirchheim, Hydrogen Solubility and Diffusivity in Defective and Amorphous Metals, Prog. Mater. Sci. 32(4) (1988) 261-325.
[60] R. Kirchheim, Reducing grain boundary, dislocation line and vacancy formation energies by solute segregation. I. Theoretical background, Acta Mater. 55(15) (2007) 5129-5138.
[61] R. Kirchheim, Reducing grain boundary, dislocation line and vacancy formation energies by solute segregation II. Experimental evidence and consequences, Acta Mater. 55(15) (2007) 5139-5148.
[62] M. Nagumo, K. Takai, N. Okuda, Nature of hydrogen trapping sites in steels induced by plastic deformation, J. Alloys Compd. 293 (1999) 310-316.
[63] M. Nagumo, Hydrogen related failure of steels - a new aspect, Mater. Sci. Technol. 20(8) (2004) 940-950.
[64] K. Takai, H. Shoda, H. Suzuki, M. Nagumo, Lattice defects dominating hydrogen-related failure of metals, Acta Mater. 56(18) (2008) 5158-5167.
[65] A. Tehranchi, W.A. Curtin, Atomistic study of hydrogen embrittlement of grain boundaries in nickel: II. Decohesion, Model. Simul. Mater. Sci. Eng. 25(7) (2017).
[66] A. Tehranchi, W.A. Curtin, Atomistic study of hydrogen embrittlement of grain boundaries in nickel: I. Fracture, J Mech Phys Solids 101 (2017) 150-165.
[67] A. Barnoush, Hydrogen embrittlement revisited by in situ electrochemical nanoindentation, Universität des Saarlandes, Saarbrücken, 2009, p. 2.
[68] T.P. Perng, J.K. Wu, A brief review note on mechanisms of hydrogen entry into metals, Mater. Lett. 57(22-23) (2003) 3437-3438.
[69] T.J. Carter, L.A. Cornish, Hydrogen in metals, Eng Fail Anal 8(2) (2001) 113-121.
[70] A. Sieverts, Die Löslichkeit von Wasserstoff in Kupfer, Eisen und Nickel, J. Phys. Chem. 77 (1911).
[71] M.H. Armbruster, The Solubility of Hydrogen at Low Pressure in Iron, Nickel and Certain Steels at 400 to 600°, J. Am. Chem. Soc. 65(6) (1943) 1043-1054.
[72] D. Wan, Y. Deng, J.I.H. Meling, A. Alvaro, A. Barnoush, Hydrogen-enhanced fatigue crack growth in a single-edge notched tensile specimen under in-situ hydrogen charging inside an environmental scanning electron microscope, Acta Mater. 170 (2019) 87-99.
[73] Y. Deng, A. Barnoush, Hydrogen embrittlement revealed via novel in situ fracture experiments using notched micro-cantilever specimens, Acta Mater. 142 (2018) 236-247.
[74] D. Xie, S. Li, M. Li, Z. Wang, P. Gumbsch, J. Sun, E. Ma, J. Li, Z. Shan, Hydrogenated vacancies lock dislocations in aluminium, Nat. Commun. 7 (2016) 13341.
[75] J. Crank, The Mathematics of Diffusion, 2nd ed., Clarendon, Oxford, 1975.

[76] A. Turnbull, 4 - Hydrogen diffusion and trapping in metals, in: R.P. Gangloff, B.P. Somerday (Eds.), Gaseous Hydrogen Embrittlement of Materials in Energy Technologies, Woodhead Publishing2012, pp. 89-128.
[77] M. Koyama, M. Rohwerder, C.C. Tasan, A. Bashir, E. Akiyama, K. Takai, D. Raabe, K. Tsuzaki, Recent progress in microstructural hydrogen mapping in steels: quantification, kinetic analysis, and multi-scale characterisation, Mater. Sci. Technol. 33(13) (2017) 1481-1496.
[78] A. Oudriss, J. Creus, J. Bouhattate, E. Conforto, C. Berziou, C. Savall, X. Feaugas, Grain size and grain-boundary effects on diffusion and trapping of hydrogen in pure nickel, Acta Mater. 60(19) (2012) 6814-6828.
[79] C.D. Beachem, A new model for hydrogen-assisted cracking (hydrogen "embrittlement"), Metallurgical and Materials Transactions B 3(2) (1972) 441-455.
[80] J. Eastman, T. Matsumoto, N. Narita, F. Heubaum, H.K. Birnbaum, Hydrogen Effects in Nickel-Embrittlement or Enhanced Ductility, in: I.M. Bernstein, A.W. Thompson (Eds.), Hydrogen in Metals, Metallurgical Society of AIME, New York, 1981, pp. 397-400.
[81] T. Matsumoto, J. Eastman, H.K. Birnbaum, Direct Observations of Enhanced Dislocation Mobility Due to Hydrogen, Scripta Metall Mater 15(9) (1981) 1033-1037.
[82] T. Tabata, H.K. Birnbaum, Direct Observations of Hydrogen Enhanced Crack-Propagation in Iron, Scripta Metall Mater 18(3) (1984) 231-236.
[83] P. Rozenak, I.M. Robertson, H.K. Birnbaum, Hvem Studies of the Effects of Hydrogen on the Deformation and Fracture of Aisi Type 316 Austenitic Stainless-Steel, Acta Metall. Mater. 38(11) (1990) 2031-2040.
[84] H.E. Hanninen, T.C. Lee, I.M. Robertson, H.K. Birnbaum, In-Situ Observations on Effects of Hydrogen on Deformation and Fracture of A533b Pressure-Vessel Steel, J. Mater. Eng. Perform. 2(6) (1993) 807-817.
[85] P. Sofronis, H.K. Birnbaum, Mechanics of the Hydrogen-Dislocation-Impurity Interactions .1. Increasing Shear Modulus, J Mech Phys Solids 43(1) (1995) 49-90.
[86] D.G. Ulmer, C.J. Altstetter, Hydrogen-Induced Strain Localization and Failure of Austenitic Stainless-Steels at High Hydrogen Concentrations, Acta Metall. Mater. 39(6) (1991) 1237-1248.
[87] W.A. Mcinteer, A.W. Thompson, I.M. Bernstein, The Effect of Hydrogen on the Slip Character of Nickel, Acta Metall. 28(7) (1980) 887-894.
[88] M.L. Martin, I.M. Robertson, P. Sofronis, Interpreting hydrogen-induced fracture surfaces in terms of deformation processes: A new approach, Acta Mater. 59(9) (2011) 3680-3687.
[89] S. Wang, A. Nagao, K. Edalati, Z. Horita, I.M. Robertson, Influence of hydrogen on dislocation self-organization in Ni, Acta Mater. 135 (2017) 96-102.
[90] S. Wang, M.L. Martin, P. Sofronis, S. Ohnuki, N. Hashimoto, I.M. Robertson, Hydrogen-induced intergranular failure of iron, Acta Mater. 69 (2014) 275-282.
[91] J. Song, W.A. Curtin, A nanoscale mechanism of hydrogen embrittlement in metals, Acta Mater. 59(4) (2011) 1557-1569.
[92] J. Song, W.A. Curtin, Atomic mechanism and prediction of hydrogen embrittlement in iron, Nat. Mater. 12(2) (2013) 145-151.
[93] M.A. Bhatia, S. Groh, K.N. Solanki, Atomic-scale investigation of point defects and hydrogen-solute atmospheres on the edge dislocation mobility in alpha iron, J. Appl. Phys. 116(6) (2014).
[94] Y.X. Zhu, Z.H. Li, M.S. Huang, H.D. Fan, Study on interactions of an edge dislocation with vacancy-H complex by atomistic modelling, Int. J. Plasticity 92 (2017) 31-44.

[95] D. Wan, A. Alvaro, V. Olden, A. Barnoush, Hydrogen-enhanced fatigue crack growth behaviors in a ferritic Fe-3wt%Si steel studied by fractography and dislocation structure analysis, Int. J. Hydrog. Energy 44(10) (2019) 5030-5042.
[96] L.B. Pfeil, The effect of occluded hydrogen on the tensile strength of iron, Proc. Royal Soc. Lond. 112 (1926) 182-195.
[97] A.R. Troiano, The Role of Hydrogen and Other Interstitials in the Mechanical Behavior of Metals (1959 Edward De Mille Campbell Memorial Lecture), Metallogr Microstruc 5(6) (2016) 557-569.
[98] R.A. Oriani, A mechanistic theory of hydrogen embrittlement of steels, Berichte der Bunsengesellschaft für physikalische Chemie 76(8) (1972) 848-857.
[99] C.J. McMahon, Hydrogen-induced intergranular fracture of steels, Eng. Fract. Mech. 68(6) (2001) 773-788.
[100] W.W. Gerberich, Modeling hydrogen induced damage mechanisms in metals, Gaseous Hydrogen Embrittlement of Materials in Energy Technologies 2 (2012) 209-246.
[101] W.W. Gerberich, R.A. Oriani, M.J. Lii, X. Chen, T. Foecke, The necessity of both plasticity and brittleness in the fracture thresholds of iron, Philos. Mag. A 63(2) (1991) 363-376.
[102] S. Lynch, Hydrogen embrittlement phenomena and mechanisms, Corros. Rev. 30(3-4) (2012) 105-123.
[103] Y.J.A. Du, L. Ismer, J. Rogal, T. Hickel, J. Neugebauer, R. Drautz, First-principles study on the interaction of H interstitials with grain boundaries in alpha- and gamma-Fe, Phys. Rev. B 84(14) (2011).
[104] I.H. Katzarov, A.T. Paxton, Hydrogen embrittlement II. Analysis of hydrogen-enhanced decohesion across (111) planes in alpha-Fe, Phy Rev Mater 1(3) (2017).
[105] X. Lu, D. Wang, D. Wan, Z.B. Zhang, N. Kheradmand, A. Barnoush, Effect of electrochemical charging on the hydrogen embrittlement susceptibility of alloy 718, Acta Mater. 179 (2019) 36-48.
[106] A. Nagao, M. Dadfarnia, B.P. Somerday, P. Sofronis, R.O. Ritchie, Hydrogen-enhanced-plasticity mediated decohesion for hydrogen-induced intergranular and "quasi-cleavage" fracture of lath martensitic steels, J Mech Phys Solids 112 (2018) 403-430.
[107] A. Nagao, M.L. Martin, M. Dadfarnia, P. Sofronis, I.M. Robertson, The effect of nanosized (Ti,Mo)C precipitates on hydrogen embrittlement of tempered lath martensitic steel, Acta Mater. 74 (2014) 244-254.
[108] A. Nagao, C.D. Smith, M. Dadfarnia, P. Sofronis, I.M. Robertson, The role of hydrogen in hydrogen embrittlement fracture of lath martensitic steel, Acta Mater. 60(13-14) (2012) 5182-5189.
[109] A. Nagao, C.D. Smith, M. Dadfarnia, P. Sofronis, I.M. Robertson, Interpretation of hydrogen-induced fracture surface morphologies for lath martensitic steel, Proc Mat Sci 3 (2014) 1700-1705.
[110] J.R. Rice, J.S. Wang, Embrittlement of Interfaces by Solute Segregation, Materials Science and Engineering a-Structural Materials Properties Microstructure and Processing 107 (1989) 23-40.
[111] A. Doruk, D. Rémi, S. Douglas, An embedded-atom method potential parameterized for sulfur-induced embrittlement of nickel, Model. Simul. Mater. Sci. Eng. (2019).
[112] T.C. Lee, I.M. Robertson, H.K. Birnbaum, An Hvem Insitu Deformation Study of Nickel Doped with Sulfur, Acta Metall. 37(2) (1989) 407-415.
[113] D.H. Lassila, H.K. Birnbaum, Intergranular Fracture of Nickel - the Effect of Hydrogen-Sulfur Co-Segregation, Acta Metall. 35(7) (1987) 1815-1822.

[114] S.M. Bruemmer, R.H. Jones, M.T. Thomas, D.R. Baer, Influence of Sulfur, Phosphorus, and Antimony Segregation on the Intergranular Hydrogen Embrittlement of Nickel, Metallurgical Transactions a-Physical Metallurgy and Materials Science 14(2) (1983) 223-232.
[115] S.P. Lynch, Environmentally assisted cracking - overview of evidence for an adsorption-induced localized-slip process, Acta Metall. 36(10) (1988) 2639-2661.
[116] J.A. Clum, The role of hydrogen in dislocation generation in iron alloys, Scripta Metall Mater 9(1) (1975) 51-58.
[117] S. Lynch, A review of underlying reasons for intergranular cracking for a variety of failure modes and materials and examples of case histories, Eng Fail Anal 100 (2019) 329-350.
[118] M. Nagumo, K. Takai, The predominant role of strain-induced vacancies in hydrogen embrittlement of steels: Overview, Acta Mater. 165 (2019) 722-733.
[119] H. Fuchigami, H. Minami, M. Nagumo, Effect of grain size on the susceptibility of martensitic steel to hydrogen-related failure, Philos. Mag. Lett. 86(1) (2006) 21-29.
[120] M. Nagumo, H. Matsuda, Function of hydrogen in intergranular fracture of martensitic steels, Philosophical Magazine a-Physics of Condensed Matter Structure Defects and Mechanical Properties 82(17-18) (2002) 3415-3425.
[121] T. Doshida, K. Takai, Dependence of hydrogen-induced lattice defects and hydrogen embrittlement of cold-drawn pearlitic steels on hydrogen trap state, temperature, strain rate and hydrogen content, Acta Mater. 79 (2014) 93-107.
[122] H. Momida, Y. Asari, Y. Nakamura, Y. Tateyama, T. Ohno, Hydrogen-enhanced vacancy embrittlement of grain boundaries in iron, Phys. Rev. B 88(14) (2013).
[123] R. Matsumoto, N. Nishiguchi, S. Taketomi, N. Miyazaki, First-Principles Calculation of Hydrogen Effects on the Formation and Diffusion of Vacancies in Alpha Iron: Discussion of the Hydrogen-Enhanced Strain-Induced Vacancy Mechanism, Journal of the Society of Materials Science, Japan 63(2) (2014) 182-187.
[124] A. Metsue, A. Oudriss, X. Feaugas, Trapping/detrapping kinetic rates of hydrogen around a vacancy in nickel and some consequences on the hydrogen-vacancy clusters thermodynamic equilibrium, Comp. Mater. Sci. 151 (2018) 144-152.
[125] A. Oudriss, J. Creus, J. Bouhattate, C. Savall, B. Peraudeau, X. Feaugas, The diffusion and trapping of hydrogen along the grain boundaries in polycrystalline nickel, Scr. Mater. 66(1) (2012) 37-40.
[126] I.M.A. Ghermaoui, A. Oudriss, A. Metsue, R. Milet, K. Madani, X. Feaugas, Multiscale analysis of hydrogen-induced softening in f.c.c. nickel single crystals oriented for multiple-slips: elastic screening effect, Sci. Rep. 9 (2019).
[127] R. Kirchheim, Revisiting hydrogen embrittlement models and hydrogen-induced homogeneous nucleation of dislocations, Scr. Mater. 62(2) (2010) 67-70.
[128] A. Barnoush, M. Asgari, R. Johnsen, Resolving the hydrogen effect on dislocation nucleation and mobility by electrochemical nanoindentation, Scr. Mater. 66(6) (2012) 414-417.
[129] A. Barnoush, H. Vehoff, Recent developments in the study of hydrogen embrittlement: Hydrogen effect on dislocation nucleation, Acta Mater. 58(16) (2010) 5274-5285.
[130] A. Barnoush, H. Vehoff, Electrochemical nanoindentation: A new approach to probe hydrogen/deformation interaction, Scr. Mater. 55(2) (2006) 195-198.
[131] X.F. Fang, A. Kreter, M. Rasinski, C. Kirchlechner, S. Brinckmann, C. Linsmeier, G. Dehm, Hydrogen embrittlement of tungsten induced by deuterium plasma: Insights from nanoindentation tests, J. Mater. Res. 33(20) (2018) 3530-3536.

[132] M. Deutges, I. Knorr, C. Borchers, C.A. Volkert, R. Kirchheim, Influence of hydrogen on the deformation morphology of vanadium (100) micropillars in the alpha-phase of the vanadium-hydrogen system, Scr. Mater. 68(1) (2013) 71-74.
[133] J.R. Davis, Nickel, cobalt, and their alloys, ASM international2000.
[134] R.B. Bhavsar, A. Collins, S. Silverman, Use of alloy 718 and 725 in oil and gas industry, Superalloys 718, 625, 706 and Various Derivatives (2001) 47-55.
[135] A. Oradei-Basile, J.F. Radavich, A Current T-T-T Diagram for Wrought Alloy 718, in: E.A. Loria (Ed.) TMS, Warrendale, PA, 1991, pp. 325-336.
[136] Inconel alloy 718, Special Metals Corporation2007.
[137] H.S. Klapper, J. Klower, O. Gosheva, Hydrogen embrittlement: the game changing factor in the applicability of nickel alloys in oilfield technology, Philos. Trans. Royal Soc. A 375(2098) (2017).
[138] L.E. Shoemaker, Alloys 625 and 725: Trends in properties and applications, Superalloys 718, 625, 706 and Derivatives, Proceedings (2005) 409-418.
[139] M. Detrois, K.A. Rozman, P.D. Jablonski, J.A. Hawk, Compositional Design and Mechanical Properties of INCONEL (R) Alloy 725 Variants, Mineral Met Mat Ser (2018) 421-437.
[140] G.D. Smith, S.J. Patel, The role of niobium in wrought precipitation-hardened nickel-base alloys, Superalloys 718, 625, 706 and Derivatives, Proceedings (2005) 135-154.
[141] A. Kimura, H.K. Birnbaum, Hydrogen induced grain-boundary fracture in high-purity nickel and its alloys - enhanced hydrogen diffusion along grain-boundaries, Acta Metall. 36(3) (1988) 757-766.
[142] W.M. Robertson, Hydrogen Permeation and Diffusion in Inconel-718 and Incoloy-903, Metallurgical Transactions a-Physical Metallurgy and Materials Science 8(11) (1977) 1709-1712.
[143] R.P. Gangloff, R.P. Wei, Gaseous Hydrogen Embrittlement of High-Strength Steels, Metallurgical Transactions a-Physical Metallurgy and Materials Science 8(7) (1977) 1043-1053.
[144] M.D. Danford, Hydrogen trapping and the interaction of hydrogen with metals, (1987).
[145] J.J.M. Jebaraj, D.J. Morrison, I.I. Suni, Hydrogen diffusion coefficients through Inconel 718 in different metallurgical conditions, Corros. Sci. 80 (2014) 517-522.
[146] R.J. Walter, R.P. Jewett, W.T. Chandler, On the mechanism of hydrogen-environment embrittlement of iron- and nickel-base alloys, Mater. Sci. Eng. 5(2) (1970) 99-110.
[147] D.H. Lassila, H.K. Birnbaum, The Effect of Diffusive Hydrogen Segregation on Fracture of Polycrystalline Nickel, Acta Metall. 34(7) (1986) 1237-1243.
[148] B. Ladna, H.K. Birnbaum, Sims Study of Hydrogen at the Surface and Grain-Boundaries of Nickel Bicrystals, Acta Metall. 35(10) (1987) 2537-2542.
[149] S.K. Lawrence, Y. Yagodzinskyy, H. Hanninen, E. Korhonen, F. Tuomisto, Z.D. Harris, B.P. Somerday, Effects of grain size and deformation temperature on hydrogen-enhanced vacancy formation in Ni alloys, Acta Mater. 128 (2017) 218-226.
[150] W. Chen, M.C. Chaturvedi, N.L. Richards, G. McMahon, Grain boundary segregation of boron in INCONEL 718, Metallurgical and Materials Transactions a-Physical Metallurgy and Materials Science 29(7) (1998) 1947-1954.
[151] D.H. Ping, Y.F. Gu, C.Y. Cui, H. Harada, Grain boundary segregation in a Ni-Fe-based (Alloy 718) superalloy, Materials Science and Engineering a-Structural Materials Properties Microstructure and Processing 456(1-2) (2007) 99-102.

[152] J.X. Dong, M.C. Zhang, X.S. Xie, R.G. Thompson, Interfacial segregation and cosegregation behaviour in a nickel-base alloy 718, Materials Science and Engineering a-Structural Materials Properties Microstructure and Processing 328(1-2) (2002) 8-13.
[153] P.D. Hicks, C.J. Altstetter, Internal hydrogen effects on tensile properties of iron-base and nickel-base superalloys, Metall. Mater. Trans. A 21(2) (1990) 365-372.
[154] L. Xiao, D.L. Chen, M.C. Chaturvedi, Shearing of gamma " precipitates and formation of planar slip bands in Inconel 718 during cyclic deformation, Scr. Mater. 52(7) (2005) 603-607.
[155] Y. Yagodzinskyy, T. Saukkonen, S. Kilpelainen, F. Tuomisto, H. Hanninen, Effect of hydrogen on plastic strain localization in single crystals of austenitic stainless steel, Scr. Mater. 62(3) (2010) 155-158.
[156] T. Cassagne, M. Bonis, D. Hills, C. Duret, Understanding field failures of alloy 718 forging materials in HP/HT wells, in: E.V. Dechema (Ed.) EUROCORR, European Corrosion Cogress, Edinburgh, 2008.
[157] D. Wang, X. Lu, Y. Deng, X. Guo, A. Barnoush, Effect of hydrogen on nanomechanical properties in Fe-22Mn-0.6C TWIP steel revealed by in-situ electrochemical nanoindentation, Acta Mater. 166 (2019) 618-629.
[158] G.C. Sneddon, P.W. Trimby, J.M. Cairney, Transmission Kikuchi diffraction in a scanning electron microscope: A review, Mat Sci Eng R 110 (2016) 1-12.

7. Reference

Part II

Paper I

Effect of electrochemical charging on the hydrogen embrittlement susceptibility of Alloy 718

Xu Lu, Dong Wang, Di Wan, Zhenbo Zhang, Nousha Kheradmand, Afrooz Barnoush

Acta Materialia 179 (2019) 36-48

Effect of electrochemical charging on the hydrogen embrittlement susceptibility of Alloy 718

Xu Lu, Dong Wang, Di Wan, Zhenbo Zhang, Nousha Kheradmand, Afrooz Barnoush

Acta Materialia 179 (2019) 36-48

Abstract: The susceptibility of age-hardened nickel-based 718 superalloy to hydrogen embrittlement was studied by the controlled electrochemical charging combined with slow strain-rate tensile tests (SSRT) and advanced characterization techniques. We proposed some novel ideas of explaining hydrogen embrittlement mechanisms of the studied material in regard to two cracking morphologies: transgranular and intergranular cracking. It is for the first time to report that electrochemical charging alone could cause slip lines, surface and subsurface cracks on nickel-based superalloys. The formation of pre-damages was discussed by calculating the hydrogen concentration gradient generated during cathodic charging. Pre-damages were proved to result in transgranular cracks and lead to the evident reduction of mechanical properties. In addition, the STRONG (Slip Transfer Resistance of Neighbouring Grains) model was used to analyze the dependence of hydrogen-assisted intergranular cracking on the microscopic incompatibility of the grain boundaries. The results show that in the presence of hydrogen, grain boundaries with a lower dislocation slip transmission are more prone to cracking during loading and vice versa.

Keywords: Hydrogen embrittlement; nickel-based superalloy; hydrogen-induced cracking; electrochemical hydrogen charging; slip transmission.

1. Introduction

Precipitation-hardened nickel-based superalloys, with their combination of excellent mechanical properties, good corrosion resistance, and wide working temperature range, are some of the best candidates used for subsea oil and gas industries. Despite their good mechanical properties, these high-strength alloys are susceptible to hydrogen embrittlement (HE) when they are used in a hydrogen-containing environment [1-9]. The mechanism of HE has been extensively debated for decades [10]. Both experimental techniques and computational models were applied to unravel the hydrogen-assisted failure process [11-13]. Several acceptable mechanisms proposed thus far include hydrogen-enhanced localized plasticity (HELP) [12, 14, 15], hydrogen-enhanced

decohesion (HEDE) [7, 16-18], hydrogen adsorption-induced dislocation emission (AIDE) [11, 19-22], hydrogen-enhanced strain-induced vacancy (HESIV) [23] and crack induction by hydride formation [6, 24-26]. Through years of understanding the role of hydrogen in nickel-based superalloys, particularly precipitation-hardened alloys, several prevalent mechanisms were proposed. When this alloy is deformed in hydrogen containing environment, two types of cracking prevail: transgranular and intergranular cracking, which are explained by HELP [3, 27] and HEDE [28, 29] the most. On one hand, recent studies [8, 28, 30] concluded that transgranular cracking originated from the intersections of slip bands. The local stress concentrations and strain discontinuities at the intersection points attract hydrogen, and the local plastic instability in combination with non-uniform hydrogen concentration lead to the primary cracking. On the other hand, hydrogen-assisted intergranular cracking was observed at delta (δ) phase decorated grain boundaries (GBs) [30], GB triple junctions [28], and high angle GBs [31]. The δ phase was proved to promote GB cracking through forming micro-cracks along its interfaces with the matrix in the framework of HEDE mechanism [7, 28, 29]. In addition, high elastic mismatch and strain localization at GBs and triple junctions facilitate decohesion and crack formation [28]. Kimura and Birnbaum [6] reported that a critical amount of hydrogen is a prerequisite for generating intergranular cracks in nickel alloys depending on the nature of the GBs and the corresponding stress state. Additionally, it has been documented that the cracking behavior of GBs is highly dependent on the misorientation angle [32, 33]. In other words, cracks are likely to initiate at high-angle GBs, while low-angle or low-Σ boundaries are more resistant to fracture [34]. However, to determine whether a GB has a high propensity to cracking or not, the measurement of misorientation alone, which is based on the 2D surface information, is far from being adequate due to the complex structure of GBs and the synergetic effect of adjacent grains upon deformation. During deformation of a polycrystalline metal, some GBs act as barriers for dislocation slip that causes dislocation pile-ups and local stress concentrations [35, 36]. Other GBs allows partial or full transmission of dislocations depending on the deformation behavior of adjacent grains and the character of GBs. By considering this, the concept of slip transferability and its impact on crack initiation along GBs was brought up to analyze the fatigue crack initiation and growth [37, 38]. And 3D characterization of the GB makes it possible to analyze the incompatibility stresses and reveal the transmission of the plasticity across the GB. However, this idea has not been involved in uncovering the underlying mechanisms of materials that failed in the hydrogenating

environment. Analyzing stress compatibility of GBs is of great help to understand hydrogen-assisted intergranular cracking behavior.

Moreover, in most of the previous studies, hydrogen was introduced into the material through electrochemical charging. And it is known that harsh charging conditions, especially electrochemical charging, can cause surface damage in the form of blisters on steel and pure iron [39-42]. However, in face-centered-cubic (FCC) metals, where hydrogen diffusion is sluggish, the impact of hydrogen absorption and its influence on the cracking behavior during deformation is rarely documented. The most important reason for this is the difficulty of preserving a clean surface after long electrochemical hydrogen charging. Thus far, most of the solutions used for electrochemical charging have been water-based, which could cause surface corrosion after charging. In ex-situ tests, further surface polishing before loading would introduce new stresses and thus conceal the useful information of charging. In the case of in-situ tests, what we observe is a combined effect of cathodic charging and mechanical loading, from which it is more difficult to disentangle the HE mechanisms responsible for each type of cracking behavior.

In the present study, a systematic analysis was conducted on the effect of cathodic charging and its subsequent impact on the mechanical properties of age-hardened Alloy 718 superalloys. We used a glycerol-based electrolyte to preserve the surface integrity of the alloy. Thus, direct observations and studies of the influence of electrochemical charging could be realized. The material was cathodically charged and then subjected to direct-surface and subsurface-damage characterization. A linkage between hydrogen-induced pre-cracking and mechanical properties was set up. Later, the 3D information of GBs was collected using Focused ion beam (FIB) cross section milling technique on the failed hydrogenated samples after mechanical loading. We adopted the STRONG (Slip Transfer Resistance of Neighbouring Grains) model proposed by Knorr [43] to analyze the relationship between the slip system compatibility and hydrogen-assisted intergranular cracking behavior. In this manner, we conducted a thorough analysis of the failure behavior of Ni-based superalloys and tried to figure out the factors controlling transgranular and intergranular cracking in the electrochemical charging conditions.

2. Materials and experimental procedure

In this work, the standard UNS N07718 (Alloy 718) alloy was used; its main chemical composition is listed in Table 1. As received from the supplier, the alloy went through standard API heat treatment with an aging temperature of 782 °C for 6.5 h before air cooling. Two-step dog-bone tensile test specimens for the slow strain-rate tensile test (SSRT) were cut by electrical discharge machining (EDM) as shown in Fig. 1(a).

Table 1 Chemical composition of Alloy 718 alloy

Element	C	Fe	Cr	Nb	Mo	Ti	Al	Co	Ni
wt. %	0.018	19.14	17.62	4.98	2.87	0.95	0.52	0.05	Balance

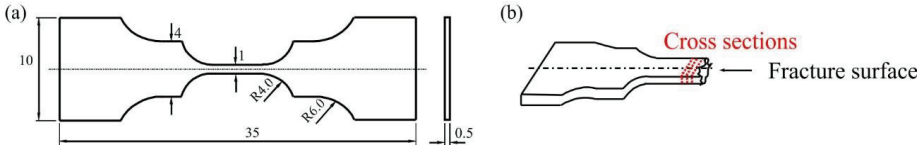

Fig. 1 (a) Specimen geometry for slow strain rate tensile test (all dimensions are shown in mm) and (b) schematic of subsurface characterization direction.

Before charging, the specimens were ground sequentially from 220 grit to 4000 grit SiC papers and then polished with 3 μm and 1 μm diamond pastes. Electropolishing was conducted in a methanolic H_2SO_4 solution at 26 V 30 s as the final step to remove the deformed layer by previous mechanical polishing. Ex-situ hydrogen charging was performed in a three-electrode electrochemical charging cell. A platinum net was used as the counter electrode and Ag/AgCl was used as the reference electrode due to its wide working temperature range. The charging process was performed in a 2:1 mixture of glycerol and H_3PO_4 [44, 45] at 75 °C at a constant potential of –1050 mV (equals to a cathodic current density of 15 mA/cm^2). This solution offers the possibility of preserving a corrosion-free surface after electrochemical charging. Later, the specimens were washed with distilled water and ethanol and dried in circulating air flow. The dwell time between finishing hydrogen charging and the damage characterization was controlled within 10 min. In order to study the effect of electrochemical charging, different charging times of 20, 40, 60, 80, 100, 120 and 168 h were chosen.

SSRT was performed at a constant nominal strain rate of 2×10^{-5} s^{-1} on a Kammrath & Weiss tensile/compression module inside the high-resolution Quanta FEG 650 scanning electron microscope (SEM, Thermo Fisher Scientific Inc., USA) for a real-time recording. The specimens were loaded until fracture to study the deformation process and crack evolution in vacuum condition (4.7×10^{-3} Pa) and hydrogen-charged condition. The dwell time before testing was controlled within 30 min. As the diffusion rate of hydrogen in the FCC material is low (about 10^{-15} m^2/s) [46], hydrogen loss within this period was negligible. In order to study the possible damage below the fracture surface, the fractured parts were electrodeposited in a Ni electroplating solution before subsurface analysis to provide appropriate edge retention and mechanical stability during sample preparation. A dense layer of Ni with about 40 μm thickness was deposited. Afterwards, the coated samples were mounted, grinded and polished. By using a caliper, the sample depth that was removed from the fracture surface was precisely controlled to be 50, 350, and 650 μm perpendicular to the tensile axis, as shown schematically in Fig 1(b). This sectioning process was proved to cause no subsurface damages on the analyzed cross-sections. To study the effect of hydrogen alone, the same subsurface characterization procedure was conducted on the hydrogenated specimens without further mechanical loading. A thorough microstructural characterization on both fracture surfaces and subsurfaces was conducted using SEM embedded with backscattered electron (BSE) and electron dispersive spectroscopy (EDS) detectors. Electron channeling contrast imaging (ECCI) was used to reveal deformation structures after fracture. Electron backscatter diffraction (EBSD) was conducted at an accelerating voltage of 20 kV with a step size of 200 nm-1 μm. Before EBSD characterization, the samples were mechanically polished and finished with a 0.04 μm colloidal silica suspension (OPS) to obtain deformation-free surfaces. FIB (Helios Nanolab DualBeam FIB, Thermo Fisher Inc., USA.) milling was performed to cut a trench across each boundary to achieve a complete grain boundary trace information on orthogonal planes to the sample surface. In addition, thermal desorption spectroscopy (TDS) test was carried out to determine the total hydrogen content in the sample after hydrogen charging. The TDS test was performed by a Bruker G4 PHONIX DH analyzer with a mass spectroscopy detector at a heating rate of 25 °C/min from 50 °C to 750 °C.

3. Results

3.1 Microstructural analysis

The initial microstructure of Alloy 718 after aging is shown in Fig. 2(a) with equiaxed grains and an average grain size of 73.5 μm. Annealing twins can be observed inside the grains, as highlighted by the yellow lines. Block-shaped nitrides (Nb, Ti)N and carbides (Nb, Ti)C are present in the matrix as illustrated in the EDS results, respectively. The coherent strengthening phases, spherical γ' and disc γ'', are homogeneously distributed in the matrix (Fig. 2(b)). A small fraction of the GBs is covered with needle-shaped intermetallic precipitate delta (δ) phases, which extend into the matrix (Fig. 2(c)) and left with a precipitation-free zone (PFZ) due to the local depletion of Nb.

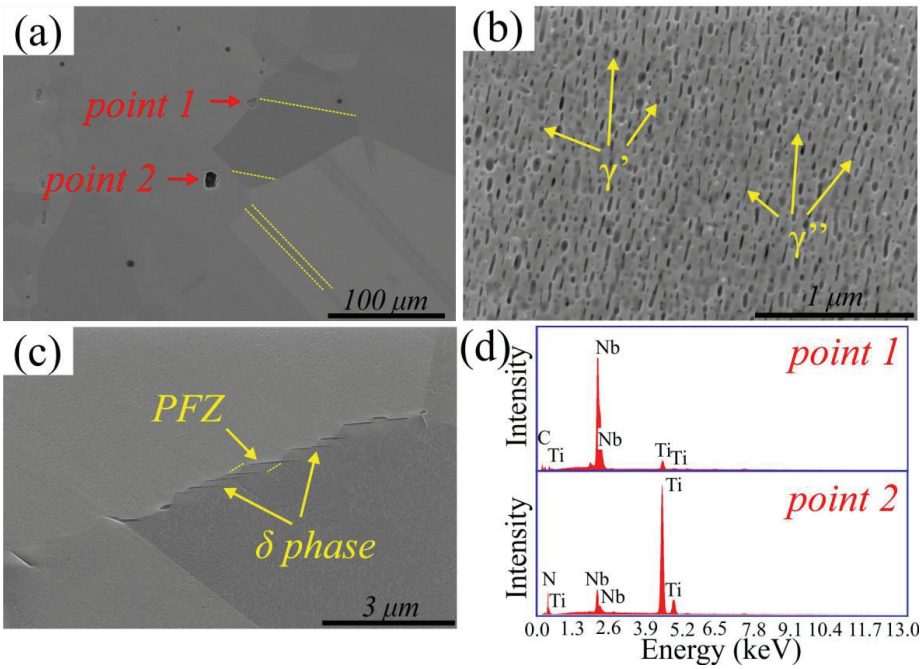

Fig. 2 Microstructure of Alloy 718 showing (a) carbides, (b) fine γ' and γ'' precipitates, and (c) the δ phase. (d) EDS information on incoherent (Nb, Ti)N nitrides and (Nb, Ti)C carbides.

3.2 Surface and subsurface response after electrochemical charging

The surface micrographs after charging are presented in Fig. 3, where we can see slip lines on the surfaces after charging. Besides, it was also possible to detect cracks on the surface after charging for more than 60 h (Fig. 3(c)–(g)). The entire formed cracks exhibit transgranular modes, as illustrated in Fig. 3(c1). Cracks larger than 15 μm/mm^2 started to form after charging the samples for more than 80 h. In severe cases, e.g., when the sample was hydrogenated for 168 h, its entire surface was filled with cracks with a tendency of peeling (Fig. 3(g)). As it is difficult to determine the exact number of cracks in this condition, the surface damage statistics excluding this case were characterized and summarized in Fig. 3(h); in this diagram, it can be observed that both the number density and the length density of surface cracks increase with charging time (≥ 40 h). And there is a crack length jump at 80 h charging. In the current study, a time period of 40 h is set as the threshold for hydrogen-induced surface cracking.

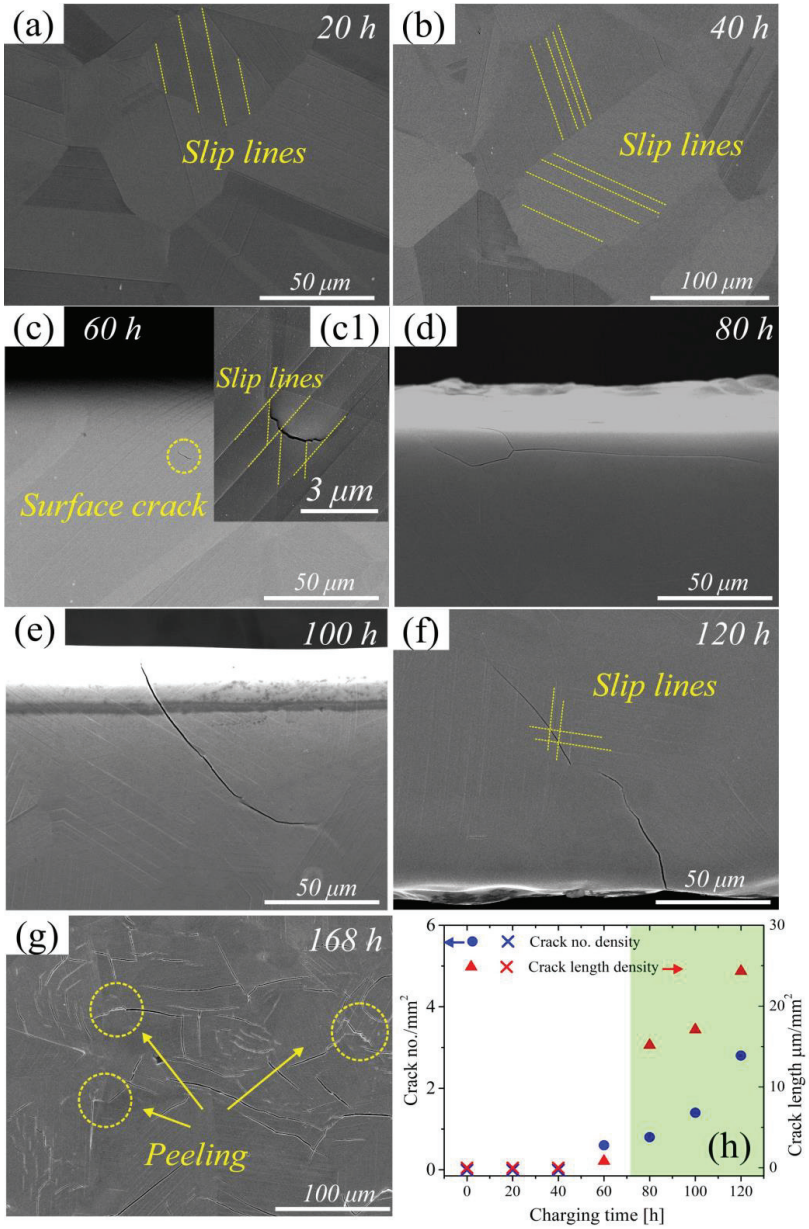

Fig. 3 BSE images ((a)-(c)), and SE images ((d)-(g)) showing slip lines and surface cracks on Alloy 718 samples after electrochemical charging. The magnified view of the area highlighted by the dashed circle in (c) is shown in (c1). (h) Statistical summary of the crack number and crack length densities on the surfaces after charging from 20 h to 120 h.

Apart from the surface damage induced by electrochemical charging, subsurface damages were also studied in hydrogen-charged samples alone without the application of any mechanical loading. Subsurface cracks can be observed after 100 h of charging. Take 120 h charged condition as an example, we found that the crack cut through carbides in a transgranular mode inside the grain (Fig. 4(a)). The crack path follows {111} plane trace (red dash lines in the slip traces in Fig. 4(b)) and exhibits a symmetric morphology across Σ3 annealing twin boundaries (TBs), but it is not deflected by carbides. The displacement and rotation of cracking attributes to their transmission through TBs. The formation of crack caused a large amount of plasticity, which results in a bulge on the surface (Fig. 4(a)) as shown by the kernel average misorientation (KAM) in Fig. 4(c). A misorientation of 2° to 8° is detected between the crack and the surface. When the crack reaches GBs, it is transmitted into another grain (Fig. 4(e)). However, the crack has a tendency to propagate along the GB which is decorated with precipitates (Fig. 4(d, d1)), and causes the debonding of δ phase-matrix interface.

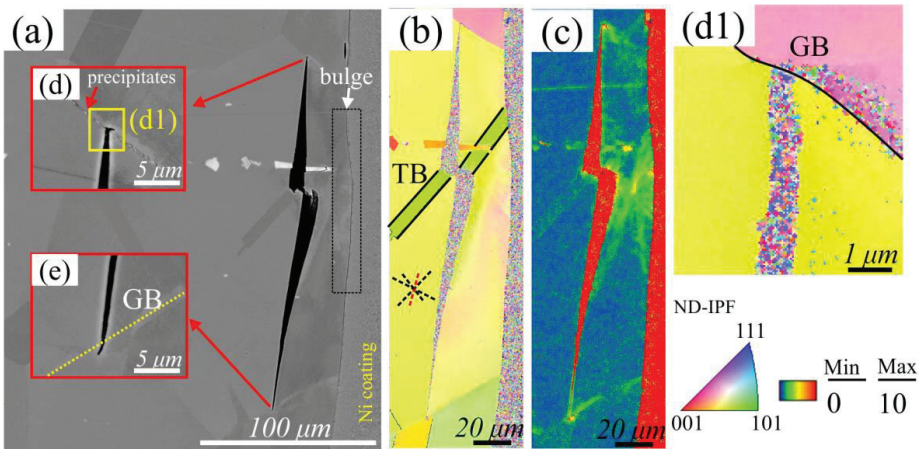

Fig. 4 SEM and EBSD analysis of subsurface cracks in the 120 h charged sample. (a), (d), and (e) Micrographs illustrating crack paths. (b) ND-IPF (inverse pole figure) map and (c) KAM map of the crack. (d1) is the ND-IPF map of the area highlighted by the yellow box in (d). (TB: twin boundary, GB: grain boundary. The color scale of the IPF maps is shown in the IPF triangle. The color scale of the KAM map is shown in the color bar.)

3.3 Slow strain rate tensile testing

To further investigate the effect of pre-formed cracks on the mechanical behavior of Alloy 718, SSRT was conducted after surface characterization. The engineering stress-strain curves generated under different charging conditions are presented in Fig. 5(a). The 168 h-charged sample was not considered as the sample was severely damaged during charging. Fig. 5(b) shows that hydrogen decreases the ultimate tensile strength (UTS) due to the reduction of the total elongation (from 27.6% without hydrogen to 2.06% after 120 h of charging). The yield strength (YS), defined as 0.2% offset stress, increases with hydrogen charging up to 60 h, after which it reduces gradually to a value lower than the YS in air at 120 h. The embrittlement factor (EF) is defined as eq. (1) [31, 47] and its evolution with respect to the charging time is presented in Fig. 5(c). It describes the relative elongation loss of the hydrogenated samples in comparison to the non-charged samples.

$$\mathrm{EF} = \left(1 - \frac{\varepsilon_{\mathrm{H}}}{\varepsilon_{\mathrm{no\ H}}}\right) \times 100\% \tag{1}$$

where ε_{H} is the engineering strain of a precharged sample after fracture and $\varepsilon_{\mathrm{no\ H}}$ represents the engineering strain of a hydrogen-free sample. The EF increases with charging time and becomes almost constant after 80 h of hydrogenation.

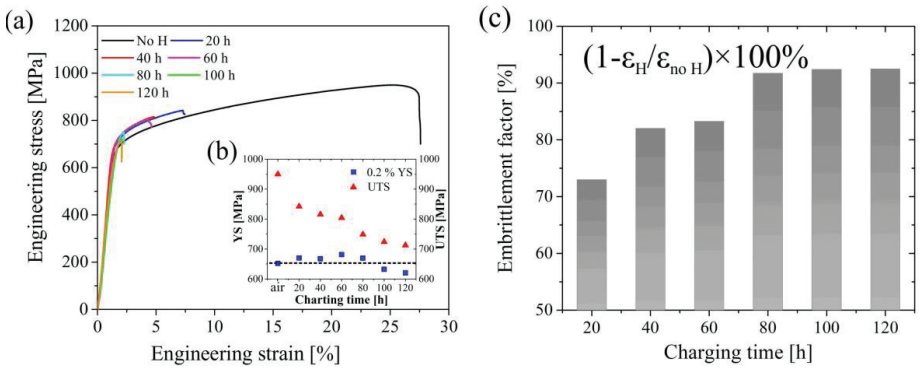

Fig. 5 (a) Engineering stress-strain curves of the tested specimens under different charging conditions. Effect of hydrogen on (b) 0.2 % YS and UTS (b) and (c) EF.

3.4 Fractography

Postmortem fractography characterization with and without hydrogen exposure was done after tensile tests. Fig. 6(a1)–(a2), (a4) show the fractography of hydrogen-free samples; the fracture surface exhibited microvoid coalescence (MVC)-assisted failure in a ductile fracture mode. Necking is a distinct feature of the ductile failure process (Fig. 6(a1)). Higher magnification images of carbonitride cracks and dimples are presented in Fig. 6(a2) and (a4). Micrographs in the vicinity of necking region show severely deformed grains with secondary cracks across carbonitrides (Fig. 6(a3)). Two activated slip systems revealed by ECCI are shown in Fig. 6(a5).

Conversely, the hydrogenated samples displayed a multi-mode failure process. A representative fracture surface of 20 h electrochemically charged sample is shown in Fig. 6(b1): it consists of a brittle area near the sample surface, a ductile region in the sample interior enclosed by the red dotted line, and a transition from brittle to ductile regions in between. In the brittle region, both intergranular and transgranular cracks are observed. Ridges, steps, and river patterns in the brittle region display transgranular features, and nanovoids along the GBs exhibit a tendency for intergranular cracking (Fig. 6(b2)). The steps and cleavage facets in Fig. 6(b3) show that dislocation slip preferred along certain slip planes. Nanovoids are observed at slip line intersections (Fig. 6(b4)). In addition, secondary transgranular cracks on the surface follow the direction of slip bands and exhibit zig-zag morphologies (Fig. 6(b5)). The same case as in the non-charged sample, most carbides on the surface are cracked.

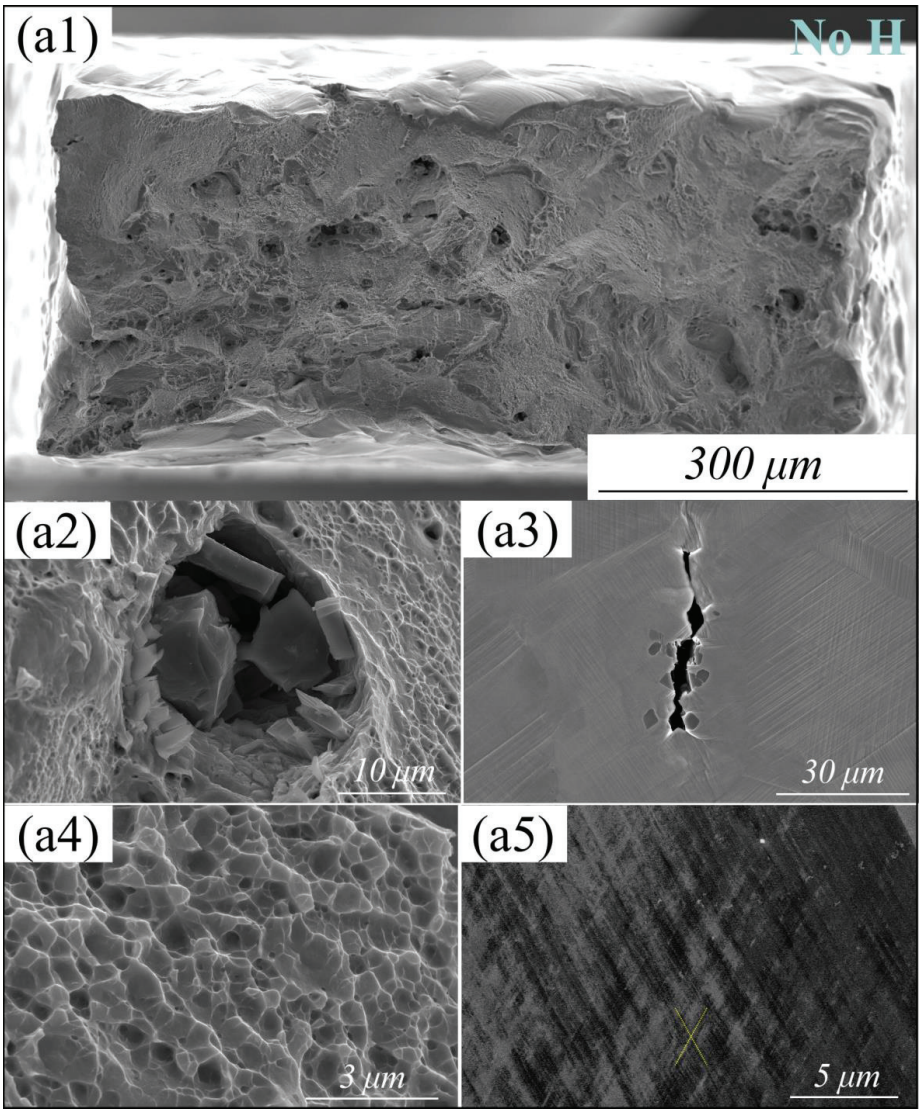
(a1)
No H
300 μm
(a2)
10 μm
(a3)
30 μm
(a4)
3 μm
(a5)
5 μm

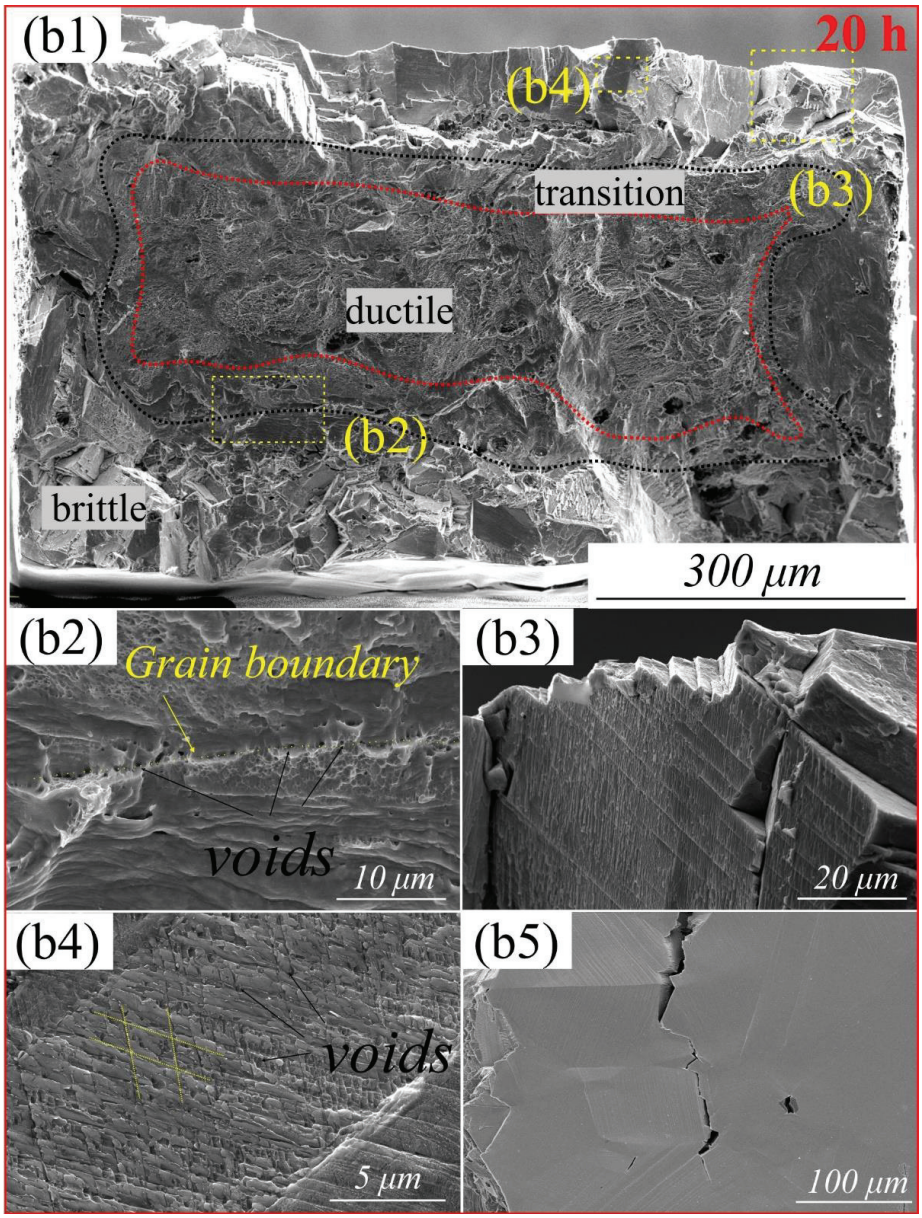

Fig. 6 (a1)-(a5): Micrograph analysis of no-hydrogen sample after failure showing (a1, a4) ductile fracture features, (a2, a3) carbonitride cracks, and (a5) surface slip lines; (b1)-(b5): micrograph analysis of a fractured sample with 20 h-charging showing (b1) transition from brittle to ductile fracture, (b2) GB microvoids, (b3) transgranular steps, (b4) microvoids at slip lines intersections, and (b5) surface secondary cracks.

Percentage of brittle area (POB) is introduced to visualize the effect of hydrogenation time on the fracture mode and assess HE sensitivity:

$$\mathrm{POB} = \frac{A_T - A_D}{A_T} \times 100\% \quad (2)$$

where A_T is the total area of the fracture surface and A_D is the area of the ductile region. The results in Fig. 7(a) indicate an increase in POB with charging time. A drastic increase in POB happened between 60 and 80 h. After 120 h of charging, the fracture surface exhibits a fully brittle fracture mode. The corresponding brittle depths of the areas showing brittle fracture in each charging condition are summarized in Fig. 7(b), which are consistent with the changes in POB.

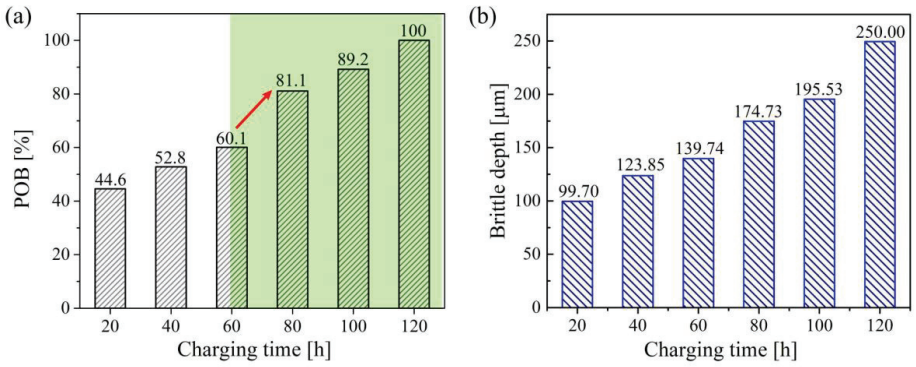

Fig. 7 Effect of hydrogen on (a) POB and (b) the corresponding brittle depth.

3.5 Subsurface crack analysis after loading

Subsurface cracks on three cross section layers were analyzed after loading the samples to fracture. In the non-charged sample, the subsurface shown in Fig. 8(a) exhibits cracks in the secondary-phase particles without intruding into the matrix, which is fully consistent with the fractography in Fig. 6(a1). In comparison, both intergranular and transgranular cracks are observed on the hydrogenated samples. Representative subsurface cracks with their ND-IPF maps are shown in Fig. 8(b)–(e). In accordance with previous studies [37, 48, 49], TBs show great resistance to crack propagation. An intergranular crack is deflected and a transgranular crack becomes blunted when they reach TBs as shown in Fig. 8(c).

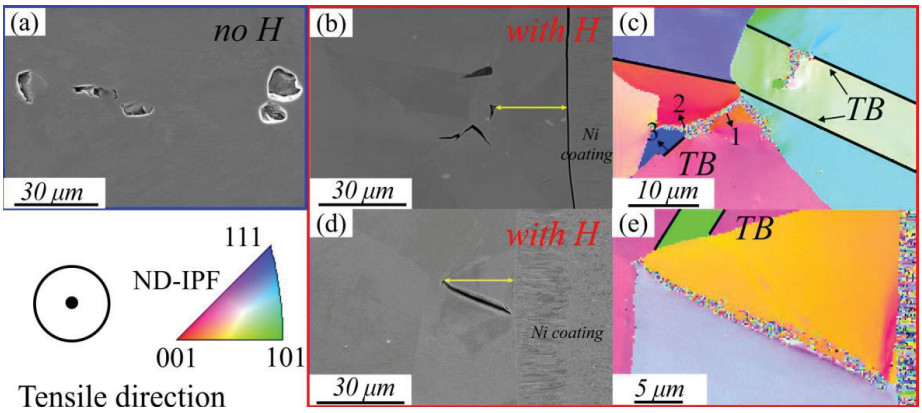

Fig. 8 Micrographs of the cross sections of (a) a hydrogen-free sample showing carbides cracks. (b)-(c) BSE images and ND-IPF maps, respectively, of a hydrogen-charged sample showing both intergranular and transgranular cracks. (d)-(e) BSE images and ND-IPF maps, respectively, of a hydrogen-charged sample showing only intergranular cracks, step size: 0.2 μm.

For a statistic analysis of these cracks, we divide them into three categories: transgranular cracks, low-Σ (Σ = 1–29) [49], and general GB (all other GBs) cracks, as shown in Fig. 9(a). Only one subsurface crack is observed at 40 h of hydrogen charging and three at 60 h of the examined cross-sections. The total number of intergranular cracks remains almost constant after charging the samples for more than 80 h, while that of transgranular cracks increases drastically with respect to the charging time. Here we assumed that intergranular cracks originate from the nearest triple junctions to the surface, and transgranular cracks initiation points are measured by the distance from the surface to the nearest cracking point. Examples of the above measurements are highlighted by the yellow arrows in Fig. 8(b)–(d). Fig. 9(b) summarizes the results and indicates that most transgranular cracks are formed near free surfaces. For samples charged for 100 h and 120 h, half of the cracks connect to the surfaces. In comparison, intergranular cracks tend to nucleate deeper in the material matrix. For samples charged between 80 to 120 h, the outermost intergranular cracks occur at an average distance of (21.50 ± 4.99) μm to the free surface, which is in agreement with the average outermost triple junction sites distance of (26.83 ± 4.56) μm. A detailed discussion of both transgranular and intergranular cracking will be presented in sections 4.3 and 4.4.

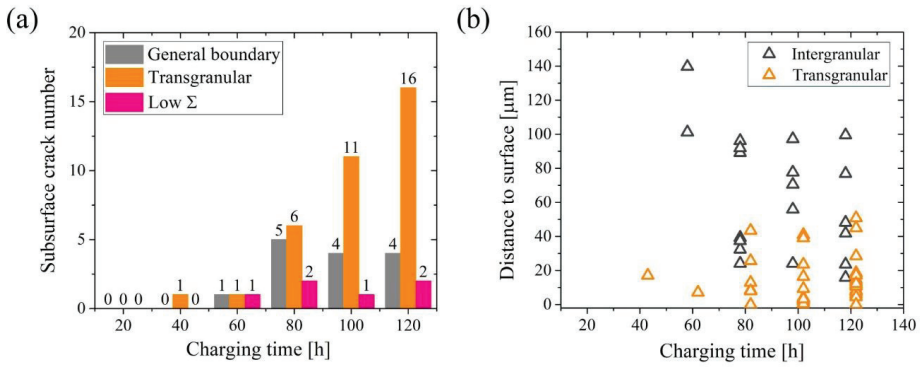

Fig. 9 Statistical analysis of subsurface cracks: (a) the number of different types of cracks on the cross-sections; and (b) distance between surface and cracks.

3.6 Slip transferability at GBs

Take a close look at the intergranular cracks and to understand the cracking mechanism in a new perspective, 3D information of GBs was collected using FIB cross section milling technique. Basically, in the STRONG model, a GB is described by two pairs of Euler angles (φ1 Φ φ2) in adjacent grains and two angles (η, ε) determining the direction of GB, as illustrated in Fig. 10. The resistance of GB to slip transmission can be expressed as eq. (3) [37]:

$$\omega_{ij} = 1 - \cos\alpha_{ij} \cdot \cos\beta_{ij} \tag{3}$$

where α is the angle between the intersection lines of the active slip plane in each grain with the GB and β is the angle between the corresponding slip directions in adjacent grains. A schematic of the residual Burges vector $\overrightarrow{b_r}$ is defined by the difference of Burgers vector of both slip systems. The matrix ω_{ij} contains in total 144 single slip systems couplings, which yield a comprehensive description of the GB resistance to slip transmission. Fig. 11 shows two examples of GB cracks and the necessary parameters needed for ω calculation. The depth tilt angle ε can be obtained from the cross sections of the GBs (Fig. 11(a3) and (b4)). To measure the surface trace angle η, the direction parallel to the gauge length was used as the reference line. The {111} slip traces are marked in Fig. 11(a2) and (b2)–(b3) with different colors indicating Schmid factor (SF) variation from the highest to the lowest value (red-blue-light blue-dark). The active slip systems can be

determined by comparing the SFs with {111} slip traces that were unambiguously measured by ECCI (Fig. 11(a2) and (b2)–(b3)), and they are marked by dot lines.

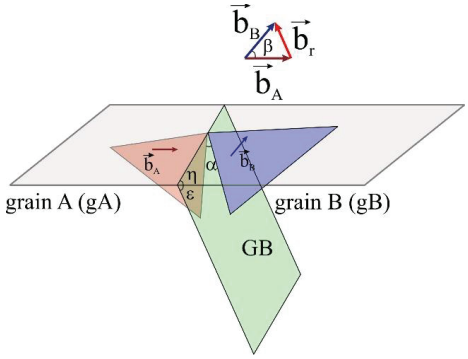

Fig. 10 Schematic of slip system coupling at a GB, together with GB traces, represented by angles (η, ε).

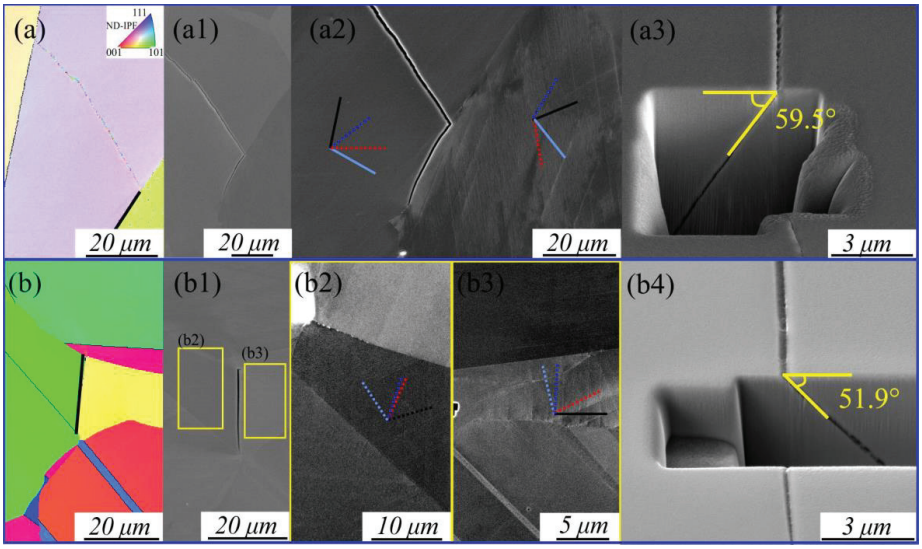

Fig. 11 ND-IPF maps (a) (b), and corresponding SE images (a1) and (b1) showing GB cracks. The ECC micrographs (a2) (b2)-(b3) indicate active slip lines that represent {111} traces (the magnitude of Schmid factors varies from the highest to the lowest value: red, blue, light blue, black; the active slip planes are marked in dotted lines), (b2)-(b3) are magnified ECC images of areas in (b1) that are marked in yellow. (a3) (b4) The FIB cross sections show GB depth tilt angles.

A summary of the measured GB parameters (including GB misorientation axes and angles), calculated SFs, GB resistance on several cracked GBs (C-GBs) of a sample that fractured after hydrogen charging is presented in Table 2. Non-cracked GBs (NC-GBs) next to the C-GBs, which are assumed to have similar stress level as those C-GBs, are presented as well. Since low-Σ GBs are relatively resistance to cracking compared to general GBs, we focused only on general GBs for the current study. The highest SF for each slip plane was calculated and presented in Table 2. The analyzed C-GBs and NC-GBs are in the range of high misorientation angles. For each of the grains adjacent to the GB, at least two slip planes were activated. When the divergence between the intersection lines of active slip planes with the GBs (α angle) is lower than 15°, there is a higher probability of slip transferability [50]. All the NC-GBs shown in Table 2 have at least one coupling slip plane with relatively low α (≤15°). In comparison, α angles of the C-GBs are much higher, with only one exception (gA-3/gB-3). Also, the parameter representing the resistance of GB to slip transmission, ω, for C-GBs are higher than those for NC-GBs. This indicates that, in the presence of hydrogen, GBs that possess low slip transmission have high stress incompatibility and can initialize crack easily.

Table 2 Measured GB parameters, active slip planes with corresponding SFs, and GB resistance calculated from eq. (3). (U V W)/ θ represents the misorientation axis and angle between adjacent grains.

C-GB	Euler angle (φ1 Φ φ2)	GB parameter (U V W)/θ	η, ε	Active slip plane (hkl)	SF	α (≤ 15°) $(h_ak_al_a)$–$(h_bk_bl_b)$	Min. ω $(h_ak_al_a)$–$(h_bk_bl_b)$
gA1	(12.1 60.7 287.2)	(-5 0 -1) /55.4	63.3, 59.5	(-1-11)	0.48	no	0.83 (-1-11)–(-111)
				(-111)	0.39		
gB1	(250.4 151.6 353.6)			(111)	0.48		
				(-111)	0.47		
gA2	(194.8 27.9 33.1)	(1 -1 -1) /49.3	26.6, 90.0	(-111)	0.47	no	0.23 (1-11)–(1-11)
				(1-11)	0.40		
				(111)	0.39		
gB2	(98.4 46.5 340)			(1-11)	0.46		
				(-1-11)	0.40		
gA3	(308.9 24.5 98.6)	(-1 1 -1) /29.9	51.9 51.9	(111)	0.49	14.4 (111)–(1-11) 5.5 (1-11)–(1-11)	0.14 (1-11)–(1-11)
				(1-11)	0.48		
				(-1-11)	0.31		
gB3	(249.9 90.1 317.7)			(1-11)	0.43		
				(-111)	0.42		
				(111)	0.05		
				(-1-11)	0.02		

NC-GB	Euler angle (φ1 Φ φ2)	GB parameter (U V W)/θ	η, ε	Active slip plane	SF	α (≤ 15°) $(h_ak_al_a)$–$(h_bk_bl_b)$	Min. ω $(h_ak_al_a)$–$(h_bk_bl_b)$
gA4	(12.1 60.7 287.2)	(-7 -1 0) /46.8	64.0, 88.8	(-1-11) (-111)	0.48 0.39	11.5 (-1-11)–(111)	0.09 (-1-11)–(111)
gB4	(59.4 158.5 266.0)			(111) (1-11)	0.49 0.49		
gA5	(225.6 87.2 302.0)	(7 1 0) /16.4	13.2, 89.0	(1-11) (-111)	0.48 0.47	1.1 (-111)–(-111)	0.01 (-111)–(-111)
gB5	(239.0 77.8 297.8)			(1-11) (-111) (-1-11)	0.49 0.42 0.33	12.2 (1-11)–(-1-11)	
gA6	(12.1 60.7 287.2)	(-1 1 -1) /51.9	26.3, 76.4	(-1-11) (-111)	0.48 0.39	1.3 (-111)–(1-11)	0.04 (-111)–(1-11)
gB6	(239.0 77.8 297.8)			(1-11) (-111) (-1-11)	0.49 0.42 0.33	12.8 (-111)–(-1-11)	
gA7	(308.9 24.5 98.6)	(0 -1 -1) /34.8	82.6, 44.2	(111) (1-11) (-1-11)	0.49 0.48 0.31	1.8 (111)–(-1-11)	0.1 (-1-11)–(-111)
gB7	(76.8 82.1 3.8)			(-111) (111) (-1-11)	0.46 0.45 0.42	3.3 (-1-11)–(-111)	

4. Discussion

The aim of this study is to perform a systematic hydrogen charging process to analyze the impact of electrochemical charging alone on the microstructure change of Alloy 718, and the relation between hydrogen-induced pre-damages and the cracking behaviors in the process of mechanical loading. In the discussion part, firstly hydrogen concentration profile along the sample was calculated to help explain the hydrogen-induced slip lines and cracks during hydrogen adsorption. Subsequently, the possible reasons for transgranular cracking and intergranular cracking were discussed in detail.

4.1 Pre-damages induced by cathodic charging

The results presented above show that slip lines were formed on the surface of Alloy 718 followed by surface and subsurface cracking in the process of electrochemical charging. These phenomena

were rarely detected and documented. The most probable reason for not being able to detect them can be attributed to the surface condition after charging, which exhibits a relatively high surface roughness or corrosion. In the present study, the sample surface was electropolished before hydrogen charging to guarantee a surface with no residual stress and the usage of a glycerol-based electrolyte ensured surface integrity. Therefore, the microstructure change on the sample in the process of cathodic charging could be recorded. The formation of surface and subsurface cracks shows severe damage caused by hydrogen ingress alone. Due to a low hydrogen diffusivity in Alloy 718, it is reasonable to infer that a gradient in hydrogen concentration from the edge to the inner region is developed with the highest concentration at the surface. And the internal stress due to hydrogen distribution inhomogeneity plays a crucial role. To visualize hydrogen concentration distribution during different charging time, the plane sheet diffusion model [51] with a fixed diffusion coefficient was used. In this context, we need to solve the one-dimensional form of Fick's second law, which is represented by eq. (4):

$$\frac{\partial \mathrm{C}}{\partial \mathrm{t}} = \mathrm{D}\frac{\partial^2 \mathrm{C}}{\partial^2 \mathrm{x}} \tag{4}$$

where C is the hydrogen concentration at a specific time t and distance x from the center of the specimen along the thickness direction. D is the hydrogen diffusion constant, which is independent of hydrogen concentration and local stress state, and can be calculated as eq. (5) [52]:

$$\mathrm{D} = 4.06 \times 10^{-7} \exp\left(-\frac{48.63\mathrm{kJ}\ /\ \mathrm{mol}}{\mathrm{RT}}\right) \mathrm{m}^2/\mathrm{s} \tag{5}$$

where R is the gas constant, and T is the charging temperature (348.15 K in the present study). This yields the value of D 2.05×10^{-14} m^2/s. Considering that the specimen is symmetric at x = 0 in the center, the boundary conditions in the region of $-L \leq x \leq L$ (L equals half length of the thickness) for this equation can therefore be written as eqs. (6)-(8):

$$\mathrm{C} = \mathrm{C}_0, \mathrm{x} = \mathrm{L}, \mathrm{t} \geq 0 \tag{6}$$

$$\mathrm{C} = \mathrm{C}_0, \mathrm{x} = -\mathrm{L}, \mathrm{t} \geq 0 \tag{7}$$

$$\frac{\partial \mathrm{C}}{\partial \mathrm{x}} = 0, \mathrm{x} = 0, \mathrm{t} \geq 0 \tag{8}$$

where C_o is the concentration of hydrogen adsorbed at the surface. Assuming that hydrogen concentration in the specimen before charging is 0 and use Laplace transformation, the solution of eq. (4) can be expressed as eq. (9):

$$\frac{C}{C_o} = \sum_{n=0}^{\infty}(-1)^n \mathrm{erfc}\frac{(2n+1)L - x}{2\sqrt{Dt}} + \sum_{n=0}^{\infty}(-1)^n \mathrm{erfc}\frac{(2n+1)L + x}{2\sqrt{Dt}} \quad (9)$$

The solution of eq. (9) is schematically shown in Fig. 12(a) in section 4.2. The calculated hydrogen concentration ratio terminates at different points, corresponding to a variation in samples' thickness. Obviously, a steep concentration gradient is generated along the sample, which is a common feature in FCC metals during cathodic charging [30, 53, 54]. In this alloy, the aging process annealed out most of the internal stress induced by water quenching, and electropolishing before hydrogen charging guaranteed the surfaces free from residual stresses. By hydrogen charging, the lattice expands, and stress evolves in the crystal. As soon as the stress reaches the level required for activation of dislocations, dislocation loops are emitted to accommodate the strain gradient in the sample and those dislocations can be assumed to be geometrically necessary dislocations (GND). Besides, the introduction of hydrogen can reduce the dislocation line energy, which further contributes to the activation of Frank-Read source [55-57]. And a high supersaturation of hydrogen accompanied by the high stresses near the surface [12] act as a driving force for dislocations to slip and leave slip traces at free surfaces (Fig. 3). This phenomenon was also reported in an austenitic phase of a super duplex stainless steel during in-situ electrochemical hydrogen charging [55]. It is also reasonable to infer that, at longer hydrogen charging time, cracks on the surface can generate at slip band intersections where stress concentration is high (Fig. 3(c1)). A similar process occurred during the pulsed plasma nitriding (PPN) of austenitic stainless steel [58]; in that case, the nitrogen content across the PPN layer was measured using an electron probe micro-analyzer, which is responsible for the observed dislocation density gradient. However, in the present study, a direct measurement of hydrogen content along the sample was difficult due to the limitations of achieving resolution within the available techniques.

It was previously proposed that subsurface cracks are caused by the accumulation of hydrogen atoms at microscopic defects, such as voids, second phase particles, and grain boundaries [59]. However, a recent study by Griesche et al. [60] stated that the presence of a second phase is not a prerequisite for cracks formation. And no hydrogen segregation was detected at the interfaces of

carbonitrides by using Nanoscale Secondary Iron Mass Spectrometry [29]. In this case, hydrogen-induced subsurface cracks could be related to hydrogen segregation at pre-existing voids or grain boundaries. Meanwhile, hydrogen-induced cracking with a noticeable opening displacement beneath the surface were reported to be caused by surface blisters [39-41, 61]. However, most of the studies were on body-centered cubic (BCC) metals. Only one paper mentioned the hydrogen-induced blister on aluminum alloys [62], but subsurface characterization was not performed. Moreover, none of these studies reported the formation of slip traces on the surface before blister formation. To determine whether such internal crack (Fig. 4) is a hydrogen-induced blister or not, hydrogen fugacity inside the crack and on the surface was discussed. On one hand, assuming that the internal gas pressure P_{H_2} at the internal cavity that was caused by the recombination of hydrogen atoms into hydrogen molecules around the defects can be roughly estimated from eq. (10) [63]:

$$P_{H_2} = \frac{K_{IC}\sqrt{\pi}}{2\sqrt{a}} \tag{10}$$

where K_{IC} is the fracture toughness of Alloy 718 alloy (95.8 MPa$\sqrt{m}$) [64] and a is the radius of the crack, which is assumed to be half size of the crack length. Here we chose the 120 h-charged sample for an estimation of the internal hydrogen pressure. This yields P_{H_2} the value of 8.5 GPa. And the hydrogen fugacity in the cavity can be calculated by using the Abel-Noble equation (eq. (11)) [65]:

$$f = P_{H_2} \cdot \exp\left(P_{H_2}\frac{b}{RT}\right) \tag{11}$$

where $b = 1.584 \cdot 10^{-5} m^3 mol^{-1}$, and this results in the extremely high values of f (order of 10^{25} atm). On the other hand, the hydrogen fugacity on the sample surface f_s is proportional to the hydrogen surface concentration C_0 during electrochemical charging, as described by the Sivert's law [66]:

$$C_0 = S_H\sqrt{f_s} \tag{12}$$

where S_H is the solubility limit of hydrogen during charging, which can be measured from eq. (13) [67]:

$$S_H = 8.8 \cdot \exp\left(\frac{-8.1\ \mathrm{kJ/mol}}{RT}\right) \mathrm{wt\ ppm\ H}/\sqrt{\mathrm{atm}} \tag{13}$$

And the hydrogen surface concentration can be estimated from the total hydrogen concentration in the sample C_M by using eq. (14) [68]:

$$C_0 = \frac{\omega C_M}{4}\sqrt{\frac{\pi}{Dt}} \tag{14}$$

where ω equals to the sample thickness. As shown in Fig. 3, 20 h is the least hydrogen charging time that can generate slip lines on the surface without causing any surface and subsurface damages. Therefore, TDS test has been performed after the sample was hydrogenated for 20 h, which yields C_M as 36.5 wt. ppm. The corresponding hydrogen surface concentration C_0 and the hydrogen fugacity f_s yield the values of 189.4 wt. ppm and 1.2×10^5 bar, respectively. The huge difference between hydrogen fugacity in the cavity and on the surface indicates that the internal crack generated during cathodic charging is not a high internal pressure-induced blister. If the blister formation were assumed, the hydrogen fugacity in the cavity and on the surface should be in a comparable level due to the continuous equilibrium of the hydrogen activities near to the surface. Thus, it is reasonable to infer that these cracks were initiated at stress concentrated areas such as GBs and TBs due to the formation of internal stress during charging.

To substantiate that the surface slip lines and cracks are caused by the internal stress due to hydrogen distribution inhomogeneity along the sample, the internal stress σ is calculated and compared with the critical resolved shear stress (CRSS) for dislocation slip. The internal stress induced by abundant dissolved hydrogen can be estimated by eq. (15):

$$\sigma = B \cdot \frac{\Delta V}{V_0} \tag{15}$$

where B is the bulk modulus of Alloy 718, and $\Delta V/V_0$ is the lattice volume change by hydrogen. The value of B cannot be obtained directly from the literature, however, one can estimate it from the bulk modulus of γ'' phase (211 GPa) and γ' phase (229 GPa) in Inconel 718 [69]. In addition, the lattice expansion $\Delta V/V_0$ has a linear relationship with the dissolved hydrogen [70]:

$$\frac{\Delta V}{V_0} = \frac{H_a}{M_a}\frac{\Delta v}{\Omega} \tag{16}$$

where H_a/M_a represents the atomic ratio between hydrogen and metal near to the surface during charging, Δv is the volume change per hydrogen atom, and Ω is the mean volume of metal atom. For Ni, this ratio was reported as 0.28 [71]. The atomic ratio H_a/M_a can be calculated by eq. (17):

$$H_a/M_a = \frac{C_0 \times N_A/M_H}{(10^6 - C_0) \times N_A/M_A} \quad (17)$$

Where N_A is the Avogadro constant, M_H and M_A are the molar mass of hydrogen (1 g/mol) and the studied Alloy 718 (59.5 g/mol), respectively. As a result, the internal stress σ near to the surface in 20 h charging condition yields 665.7 MPa. This value is higher than the CRSS (218.9 MPa) for slip in a single crystal that is deduced from the measured polycrystalline yield stress σ_Y (669.8 MPa for 20 h charging) using the Taylor factor (3.06) [72]. The above calculations confirm that the internal stress generated during electrochemical charging is high enough to be the driving force for the hydrogen-induced surface damages. Worthy of note, the estimated value of the internal stress, which is only an approximation based on the Hook's law, though not accurate, is able to qualitatively testify the mechanism for the plastic deformation during hydrogen charging. This deduction also applies to the longer time charging conditions.

4.2 Failure mode of Alloy 718 with the presence of hydrogen

The deformation mechanism in hydrogen-charged samples is different from that of hydrogen-free samples. The failure mode of Alloy 718 transfers from ductile to brittle fracture. Both transgranular and intergarnular fracture modes were found on samples failed in a hydrogenation environment. By introducing hydrogen, YS increased at first due to the solid solution strengthening effect of hydrogen, which was also reported for iron [73] and FCC high-entropy alloys [74, 75]. During the increment of charging time, YS after 80 h charging reduced, which might be caused by the internal and external pre-damages generated during hydrogen charging (Fig. 3). This resulted in a rapid fracture after reaching the yield point. At the same time, there is a drastic change of EF and POB results between 60 and 80 h (Fig. 7(a)), which fits well with the sudden increment in surface crack length density after charging (Fig. 3(h)), indicating again that pre-damages induced by cathodic charging assist both the formation and growth of cracks in the process of mechanical loading. Once a pre-crack is large enough, it propagates readily at a lower stress level, which results in the early brittle fracture of the sample.

It is worth mentioning that the brittle depth at each charging condition measured from fractography corresponds well to the hydrogen concentration at approximately 0.12 C_0 (Fig. 12 (a)) that obtained from the simulation, as illustrated in Fig. 12(b). This result means that the sample region with a hydrogen concentration reaches to this level (22.7 wt. ppm) during electrochemical charging can cause a brittle fracture upon mechanical loading. Although hydrogen charging solution in Ref. [67] is different from the current study, the usage of both acidic electrolytes can, to some extent, give a hint for the amount of hydrogen that can initiate brittleness.

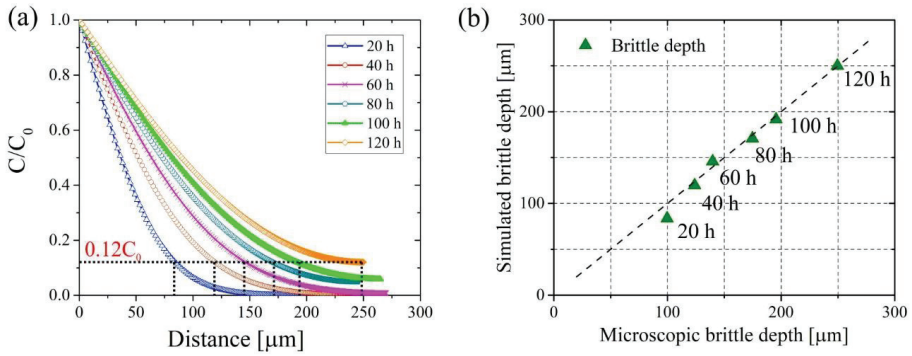

Fig. 12 (a) Hydrogen concentration profile for different charging time and (b) comparison of hydrogen effect on brittle depth measured from fracture surface and the simulated 0.12 C_0 results.

4.3 Hydrogen-assisted transgranular cracking during deformation

Concentration gradient during hydrogen charging results in compressive stresses in the outer regions of the sample [12], which in turn causes slip lines and surface/subsurface cracks even without mechanical loading. Once the sample is loaded, those pre-damages can easily propagate with the assistance of hydrogen accumulated at these stress concentration regions. Since part of the transgranular cracks were surface cracks, and there is a drastic increment of transgranular cracks between 80 h and 120 h (Fig. 9(a)) even though they fractured at similar deformation level, it is reasonable to infer that surface cracks induced by hydrogen charging promoted the formation and propagation of transgranular cracks. Concomitantly, intersections of slip lines act as strain concentration areas that attract hydrogen, and the formation of embryos of nanovoids becomes

easier (Fig. 6(b4)) [8, 28, 30]. Quasi-cleavage is a commonly reported fracture feature in the hydrogenated precipitation-hardened Alloy 718 [9, 29, 76, 77]. Hydrogen-induced cracking along dislocation slip bands (DSBs), particularly at nonparallel DSBs intersections near the surface [8, 9, 76], has been claimed to be the reason for the observed quasi-cleavage feature. Hydrogen atmospheres reduce the tendency for dislocation cross-slip by stabilizing the edge component [78]. Furthermore, the reduction of SFE due to the presence of hydrogen [68, 79, 80] promotes slip planarity and enhances the stress concentration at the intersections of {111} slip planes. In the current study, another possible reason for the occurrence of surface transgranular cracking upon loading is the difference in the stress conditions between surfaces and subsurfaces. At regions close to the surface where plane stresses dominate, grains experience relatively lower incompatibility stresses and constraints from neighbouring grains. Thus, surface GBs are tougher and show less cracking compared to the grain interior. This in return promotes the possibility of transgranular cracking on the surface. To the authors' knowledge, this is for the first time to report that hydrogen charging alone causes slip lines and cracks in nickel-based superalloys. It is worth mentioning that the charging condition is relatively moderate and without any hydrogen poison. Compared to the room temperature (25 °C), the current charging temperature (75 °C) increases the hydrogen diffusion rate and solubility by 16.7 and 1.6 times, respectively, according to eqs. (5) and (13). Thus, one would expect a more severe hydrogen charging condition with a steeper hydrogen concentration gradient at room temperature. Compared to pure Ni and other nickel-based alloys showing intergranular failure, the pronounced transgranluar fracture in the tested Alloy 718 could be attributed to several reasons. It was reported that the failure mode of Alloy 718 is highly dependent on the virgin microstructure [7, 8, 30]. When the GBs are heavily decorated with δ phase, intergranular failure is more frequently observed, which is not the case in the current material with merely small fraction of δ phase. Additionally, hydrogen-induced internal stress initiates dislocation slips and possible transgranular cracks with prolonged charging time. Those pre-damages act as pre-existing stress concentrators that can substantially promote transgranular cracking upon loading. Moreover, the pronounced localized planar slip due to the high volume of nano-sized precipitates facilitates the slip planes as the sources of cracks rather than the GBs. With mechanical loading, transgranular crack evolves more, albeit both types of cracks are evolving. The results showed that hydrogen-charging induced pre-damages had a detrimental effect on the

mechanical behavior of nickel-based superalloys. And it is necessary to consider this effect on HE in future experimental studies.

4.4 Hydrogen-assisted intergranular cracking during deformation

Hydrogen-assisted intergranular cracking was observed in the precipitation hardened nickel-based superalloys. Different from the debonding mechanism proposed for intergranular cracking in the presence of δ phase [28, 30, 53], in this study, we introduced a new parameter, i.e. GB resistance to slip transmission, to understand the stress incompatibility between the adjacent grains and its impact on the propensity for GB cracking. In general, GBs will block dislocations from intragranular movement and enhance local stress incompatibility, which in turn increases the risk of crack initiation [81]. The transferability of slip systems through GBs has been proven to play a crucial role in the evaluation of local GB flow stress in pure Ni [82] and GB crack initiation in mild steels [43]. To predict which slip system is favorable for slip transfer, Lee, Robertson and Birnbaum [83] proposed three criteria: (a) the angle between the intersection lines of the slipping planes with the GB plane should be minimal; (b) the component of the residual Burgers vector that protrudes from the grain boundary should be minimal; (c) the resolved shear stress acting on the active slipping system should be maximum. The introduction of GB resistance to slip transmission, ω_{ij}, provides the possibility of describing dislocations transferability at GBs by considering conditions (a) and (b). Condition (c) is not so easy to determine due to the superimposed local stress caused by the anisotropic elastic incompatibility of the two neighbouring grains. The normalized effective normal stress acting on a GB can be described by the Schmid-Modified Grain Boundary Stress (SMGBS) model [84]. However, it does not provide quantitative results, but rather an indication of the stress field variation with a discrepancy in grain orientations. Meanwhile, one should consider the synergetic effect of all these factors, since the slip system experiencing the maximum resolved shear stress need not be activated if conditions (a) and (b) are not satisfied [85]. In the current study, we focused on conditions (a) and (b), which are more important when more than one active incoming or outgoing slip system operates. Assuming that the critical value for ω_{ij} is $\omega = 1 - \cos 15° \cdot \cos 15° = 0.067$, which is in line with the suggestions made by Davis [50] and Werner [86], it is quite obvious that in the hydrogen-charged samples, ω_{ij} of C-GBs is much higher than the critical value (Table 2). This means that the transferability of slip at those

GBs is much more difficult, and a high stress incompatibility will arise at those regions. An intuitive example of the non-transferrable slip is the high flow stress and local buckling at GBs due to dislocation pileups, which was reported on the deformed high-angle GB bi-crystal micropillars [82]. Furthermore, molecular dynamic simulations of iron in Ref. [87] claimed that hydrogen atoms segregating along the GB distort the lattice structure, thus consistently increase the energy barrier to slip transmission. Meanwhile, slip planarity is enhanced in FCC metals in the presence of hydrogen owing to the reduction of SFE [79, 80]. Hence, local flow stress increases at the intersections of GBs with {111} sliding planes. The accumulation of hydrogen atoms at those stress concentration areas further reduces the defect-formation energy in the framework of "the Defactant" model proposed by Kirchheim [57, 88]. As a result, cracks occur readily. On the other hand, the GB resistance of NC-GBs is very close to the critical value, which indicates that a slip can pass through more easily in those GBs with higher microscopic compatibility. It is worth mentioning that all the analyzed GBs in Table 2 are free of δ phase, which eliminates the detrimental effect of δ phase when assessing slip transferability at GBs. The δ phase was proposed to exert a nontrivial effect on the intergranular GB cracking by initializing micro-cracks [28, 29], since a soft PFZ around δ enhances stress localization. In addition to avoiding the formation of the δ phase through optimizing the heat treatment processes, attention should also be paid on how to achieve GBs that hold high slip transferability in the concept of GB engineering.

5. Conclusions

Hydrogen embrittlement in electrochemically charged Alloy 718 was investigated using slow strain rate tensile test (SSRT) in combination with advanced characterization techniques, i.e. secondary electron microscopy (SEM), electron channeling contrast imaging (ECCI), electron backscatter diffraction (EBSD), and electron dispersive spectroscopy (EDS). Focused ion beam (FIB) was used to collect 3D information of GBs. A systematic study was conducted on the impact of hydrogen charging on the alloy's microstructure change and its mechanical properties during mechanical loading. The transgranular cracking mechanism was discussed in detail by calculating hydrogen concentration profiles. In this study, GB compatibility, i.e., dislocation slip transferability was considered for the first time to explain the intergranular fracture in nickel-based superalloys by using STRONG model. The major conclusions can be summarized as:

1) The presence of hydrogen has a strong detrimental effect on the mechanical properties of Alloy 718; the mechanical property degradation is accompanied by a transition from microvoid coalescence (MVC)-induced ductile failure to hydrogen-assisted brittle fracture. Both transgranular and intergranular cracks could be observed. In the current material, sample regions with a hydrogen concentration reaches to 22.7 wt. ppm during electrochemical charging can initiate brittleness upon mechanical loading.
2) Electrochemical charging has a prominent effect on the cracking behavior of Alloy 718. Cathodic charging alone caused slip lines, surface and subsurface cracks. The formation of pre-damages results in a reduction of yield strength, an increment of embrittlement factor and percent of brittle area, and finally assists an early failure of the alloy. Hydrogen concentration gradient accompanied by the high stresses near the surface is responsible for the initiation of the pre-damages. These damages are cracking sources in the process of mechanical loading.
3) The formation of transgranular cracks resides in two reasons: (a) pre-damages caused by electrochemical charging before loading promote the initiation and propagation of transgranular cracks; (b) intersections of dislocation slip bands on {111} planes act as stress concentrators that attract hydrogen and lead to void nucleation, which finally results in cracking.
4) The GB transferability of dislocations is an important factor determining the propensity for intergranular cracking. In the presence of hydrogen, GBs with high resistance to slip transmission increase the probability for crack initiation upon loading due to the synergetic effect of hydrogen and local stress incompatibility, and GBs with lower resistance to slip transmission are less susceptible to cracking.

Acknowledgements

The authors gratefully acknowledge the financial support from the Research Council of Norway through the project HyF-Lex (244068/E30). Aker Solutions is acknowledged for providing Alloy 718. The Research Council of Norway is acknowledged for the support to the Norwegian Micro- and Nano-Fabrication Facility, NorFab, project number 245963/F50.

References

[1] N. Totsuka, E. Lunarska, G. Cragnolino, Z. Szklarskasmialowska, Effect of hydrogen on the intergranular stress-corrosion cracking of Alloy-600 in high-temperature aqueous environments, Corrosion 43(8) (1987) 505-514.
[2] Y. Yao, X.L. Pang, K.W. Gao, Investigation on hydrogen induced cracking behaviors of Ni-base alloy, Int. J. Hydrog. Energy 36(9) (2011) 5729-5738.
[3] P.D. Hicks, C.J. Altstetter, Internal hydrogen effects on tensile properties of iron-base and nickel-base superalloys, Metall. Mater. Trans. A 21(2) (1990) 365-372.
[4] A.M. Brass, J. Chene, Influence of deformation on the hydrogen behavior in iron and nickel base alloys: a review of experimental data, Mater. Sci. Eng. A 242(1-2) (1998) 210-221.
[5] J. Chene, A.M. Brass, Role of temperature and strain rate on the hydrogen-induced intergranular rupture in alloy 600, Metall. Mater. Trans. A 35a(2) (2004) 457-464.
[6] A. Kimura, H.K. Birnbaum, Hydrogen induced grain-boundary fracture in high-purity nickel and its alloys - enhanced hydrogen diffusion along grain-boundaries, Acta Metall. 36(3) (1988) 757-766.
[7] Z. Tarzimoghadam, M. Rohwerder, S.V. Merzlikin, A. Bashir, L. Yedra, S. Eswara, D. Ponge, D. Raabe, Multi-scale and spatially resolved hydrogen mapping in a Ni–Nb model alloy reveals the role of the δ phase in hydrogen embrittlement of alloy 718, Acta Mater. 109 (2016) 69-81.
[8] Z.B. Zhang, G. Obasi, R. Morana, M. Preuss, Hydrogen assisted crack initiation and propagation in a nickel-based superalloy, Acta Mater. 113 (2016) 272-283.
[9] Z. Zhang, G. Obasi, R. Morana, M. Preuss, In-situ observation of hydrogen induced crack initiation in a nickel-based superalloy, Scr. Mater. 140 (2017) 40-44.
[10] W.H. Johnson, On some remarkable changes produced in iron and steel by the action of hydrogen and acids, Proc. Royal Soc. Lond. 23 (1875) 168-179.
[11] S.P. Lynch, Environmentally assisted cracking - overview of evidence for an adsorption-induced localized-slip process, Acta Metall. 36(10) (1988) 2639-2661.
[12] H.K. Birnbaum, P. Sofronis, Hydrogen-enhanced localized plasticity - a mechanism for hydrogen-related fracture, Mater. Sci. Eng. A 176(1-2) (1994) 191-202.
[13] A. Tehranchi, W.A. Curtin, Atomistic study of hydrogen embrittlement of grain boundaries in nickel: II. Decohesion, Model. Simul. Mater. Sci. Eng. 25(7) (2017).
[14] H.K. Birnbaum, Mechanisms of hydrogen related fracture of metals, Illinois University at Urbana department of materials science and engineering, 1989.
[15] Y. Jagodzinski, H. Hanninen, O. Tarasenko, S. Smuk, Interaction of hydrogen with dislocation pile-ups and hydrogen induced softening of pure iron, Scr. Mater. 43(3) (2000) 245-251.
[16] L.B. Pfeil, The effect of occluded hydrogen on the tensile strength of iron, Proc. Royal Soc. Lond. 112 (1926) 182-195.
[17] W.W. Gerberich, R.A. Oriani, M.J. Lii, X. Chen, T. Foecke, The necessity of both plasticity and brittleness in the fracture thresholds of iron, Philos. Mag. A 63(2) (1991) 363-376.
[18] C.J. McMahon, Hydrogen-induced intergranular fracture of steels, Eng. Fract. Mech. 68(6) (2001) 773-788.
[19] S. Lynch, Hydrogen embrittlement phenomena and mechanisms, Corros. Rev. 30(3-4) (2012) 90-130.
[20] S.P. Lynch, Metallographic contributions to understanding mechanisms of environmentally assisted cracking, Metallography 23(2) (1989) 147-171.

[21] S.P. Lynch, Comments on "A unified model of environment-assisted cracking", Scr. Mater. 61(3) (2009) 331-334.
[22] S.P. Lynch, Mechanisms of hydrogen-assisted cracking, Metals Forum 2(3) (1979) 189-200.
[23] M. Nagumo, Hydrogen related failure of steels - a new aspect, Mater. Sci. Technol. 20(8) (2004) 940-950.
[24] Y. Yao, X. Pang, K. Gao, Investigation on hydrogen induced cracking behaviors of Ni-base alloy, Int. J. Hydrog. Energy 36(9) (2011) 5729-5738.
[25] S. Hinotani, Y. Ohmori, F. Terasaki, Effect of nickel on hydride formation and hydrogen embrittlement in Ni-Cr-Fe alloys, Mater. Sci. Eng. 74(2) (1985) 119-131.
[26] O.A. El kebir, A. Szummer, Comparison of hydrogen embrittlement of stainless steels and nickel-base alloys, Int. J. Hydrog. Energy 27(7-8) (2002) 793-800.
[27] L. Xiao, D.L. Chen, M.C. Chaturvedi, Shearing of γ″ precipitates and formation of planar slip bands in Inconel 718 during cyclic deformation, Scr. Mater. 52(7) (2005) 603-607.
[28] Z. Tarzimoghadam, D. Ponge, J. Klower, D. Raabe, Hydrogen-assisted failure in Ni-based superalloy 718 studied under in situ hydrogen charging: The role of localized deformation in crack propagation, Acta Mater. 128 (2017) 365-374.
[29] Z.B. Zhang, K.L. Moore, G. McMahon, R. Morana, M. Preuss, On the role of precipitates in hydrogen trapping and hydrogen embrittlement of a nickel-based superalloy, Corros. Sci. 146 (2019) 58-69.
[30] V. Demetriou, J.D. Robson, M. Preuss, R. Morana, Study of the effect of hydrogen charging on the tensile properties and microstructure of four variant heat treatments of nickel alloy 718, Int. J. Hydrog. Energy (2017).
[31] S. Jothi, S.V. Merzlikin, T.N. Croft, J. Andersson, S.G.R. Brown, An investigation of micro-mechanisms in hydrogen induced cracking in nickel-based superalloy 718, J. Alloys Compd. 664 (2016) 664-681.
[32] T. Watanabe, An approach to frain-boundary design for strong and ductile polycrystals, Res. Mech. 11(1) (1984) 47-84.
[33] T. Watanabe, S. Tsurekawa, The control of brittleness and development of desirable mechanical properties in polycrystalline systems by grain boundary engineering, Acta Mater. 47(15-16) (1999) 4171-4185.
[34] S. Bechtle, M. Kumar, B.P. Somerday, M.E. Launey, R.O. Ritchie, Grain-boundary engineering markedly reduces susceptibility to intergranular hydrogen embrittlement in metallic materials, Acta Mater. 57(14) (2009) 4148-4157.
[35] E.O. Hall, The Deformation and Ageing of Mild Steel .2. Characteristics of the Luders Deformation, Proc. Phy. Soc. B 64(381) (1951) 742-747.
[36] N.J. Petch, The Cleavage Strength of Polycrystals, J. Iron Steel Inst. 174 (1953) 25-28.
[37] A.F. Knorr, M. Marx, F. Schaefer, Crack initiation at twin boundaries due to slip system mismatch, Scr. Mater. 94 (2015) 48-51.
[38] M.D. Sangid, H.J. Maier, H. Sehitoglu, The role of grain boundaries on fatigue crack initiation - An energy approach, Int. J. Plasticity 27(5) (2011) 801-821.
[39] A. Laureys, E. Van den Eeckhout, R. Petrov, K. Verbeken, Effect of deformation and charging conditions on crack and blister formation during electrochemical hydrogen charging, Acta Mater. 127 (2017) 192-202.
[40] D. Pérez Escobar, C. Miñambres, L. Duprez, K. Verbeken, M. Verhaege, Internal and surface damage of multiphase steels and pure iron after electrochemical hydrogen charging, Corros. Sci. 53(10) (2011) 3166-3176.

[41] S. Ayadi, Y. Charles, M. Gaspérini, I. Caron Lemaire, T. Da Silva Botelho, Effect of loading mode on blistering in iron submitted to plastic prestrain before hydrogen cathodic charging, Int. J. Hydrog. Energy 42(15) (2017) 10555-10567.
[42] C.F. Dong, Z.Y. Liu, X.G. Li, Y.F. Cheng, Effects of hydrogen-charging on the susceptibility of X100 pipeline steel to hydrogen-induced cracking, Int. J. Hydrog. Energy 34(24) (2009) 9879-9884.
[43] W. Schaf, M. Marx, A.F. Knorr, Influence of microstructural barriers on small fatigue crack growth in mild steel, Int. J. Fatigue 57 (2013) 86-92.
[44] R. Kirchheim, Hydrogen Solubility and Diffusivity in Defective and Amorphous Metals, Prog. Mater. Sci. 32(4) (1988) 261-325.
[45] T. Hajilou, M.S.B. Hope, A.H. Zavieh, N. Kheradmand, R. Johnsen, A. Barnoush, In situ small-scale hydrogen embrittlement testing made easy: An electrolyte for preserving surface integrity at nano-scale during hydrogen charging, Int. J. Hydrog. Energy 43(27) (2018) 12516-12529.
[46] J.J.M. Jebaraj, D.J. Morrison, I.I. Suni, Hydrogen diffusion coefficients through Inconel 718 in different metallurgical conditions, Corros. Sci. 80 (2014) 517-522.
[47] L. Fournier, D. Delafosse, T. Magnin, Cathodic hydrogen embrittlement in alloy 718, Mater. Sci. Eng. A 269(1-2) (1999) 111-119.
[48] T. Watanabe, The impact of grain-boundary-character-distribution on fracture in polycrystals, Mater. Sci. Eng. A 176(1-2) (1994) 39-49.
[49] M. Seita, J.P. Hanson, S. Gradecak, M.J. Demkowicz, The dual role of coherent twin boundaries in hydrogen embrittlement, Nat. Commun. 6 (2015).
[50] K.G. Davis, Teghtsoo.E, A. Lu, Slip Band Continuity across Grain Boundaries in Aluminum, Acta Metall. 14(12) (1966) 1677-1684.
[51] J. Crank, The Mathematics of Diffusion, 2nd ed., Clarendon, Oxford, 1975.
[52] J. Xu, X.K. Sun, Q.Q. Liu, W.X. Chen, Hydrogen permeation behavior in In718 and Gh761 superalloys, Metall. Mater. Trans. A 25(3) (1994) 539-544.
[53] V. Demetriou, J.D. Robson, M. Preuss, R. Morana, Effect of hydrogen on the mechanical properties of alloy 945X (UNS N09945) and influence of microstructural features, Mater. Sci. Eng. A 684 (2017) 423-434.
[54] D. Wang, X. Lu, Y. Deng, X. Guo, A. Barnoush, Effect of hydrogen on nanomechanical properties in Fe-22Mn-0.6C TWIP steel revealed by in-situ electrochemical nanoindentation, Acta Mater. 166 (2019) 618-629.
[55] A. Barnoush, M. Zamanzade, H. Vehoff, Direct observation of hydrogen-enhanced plasticity in super duplex stainless steel by means of in situ electrochemical methods, Scr. Mater. 62(5) (2010) 242-245.
[56] R. Kirchheim, Reducing grain boundary, dislocation line and vacancy formation energies by solute segregation II. Experimental evidence and consequences, Acta Mater. 55(15) (2007) 5139-5148.
[57] A. Pundt, R. Kirchheim, Hydrogen in metals: Microstructural aspects, Annu. Rev. Mater. Res. 36 (2006) 555-608.
[58] M. Asgari, A. Barnoush, R. Johnsen, R. Hoel, Microstructural characterization of pulsed plasma nitrided 316L stainless steel, Mater. Sci. Eng. A 529 (2011) 425-434.
[59] R. Gibala, A.J. Kumnick, Hydrogen Embrittlement and Stress Corrosion Cracking Edited by R. Gibala and R. F. Hehemann (1984) 61-77.

[60] A. Griesche, E. Dabah, T. Kannengiesser, N. Kardjilov, A. Hilger, I. Manke, Three-dimensional imaging of hydrogen blister in iron with neutron tomography, Acta Mater. 78 (2014) 14-22.
[61] M.C. Tiegel, M.L. Martin, A.K. Lehmberg, M. Deutges, C. Borchers, R. Kirchheim, Crack and blister initiation and growth in purified iron due to hydrogen loading, Acta Mater. 115 (2016) 24-34.
[62] E.P. Georgiou, V.P. Cevallos, T. Van der Donck, D. Drees, J. Meersschaut, N. Panagopoulos, J.P. Celis, Effect of cathodic hydrogen charging on the wear behavior of 5754 Al alloy, Wear 390-391 (2017) 295-301.
[63] Y.V. Banakhevych, O.V. Hembara, O.E. Andreikiv, Numerical analysis of the kinetics of propagation of hydrogen blisters in the oil-and-gas equipment, Mater. Sci. 45(5) (2009) 626-637.
[64] B. Farahmand, Virtual testing and predictive modeling: for fatigue and fracture mechanics allowables, Springer, Boston, MA2009.
[65] C.S. Marchi, B.P. Somerday, S.L. Robinson, Permeability, solubility and diffusivity of hydrogen isotopes in stainless steels at high gas pressures, Int. J. Hydrog. Energy 32(1) (2007) 100-116.
[66] J. Venezuela, C. Tapia-Bastidas, Q.J. Zhou, T. Depover, K. Verbeken, E. Gray, Q.L. Liu, Q. Liu, M.X. Zhang, A. Atrens, Determination of the equivalent hydrogen fugacity during electrochemical charging of 3.5NiCrMoV steel, Corros. Sci. 132 (2018) 90-106.
[67] P.D. Hicks, Altstetter, C.J. , Comparison of internal hydrogen embrittlement of superalloys 718 and 625, JOM (1991) pp 635–651.
[68] A.E. Pontini, J.D. Hermida, X-ray diffraction measurement of the stacking fault energy reduction induced by hydrogen in an AISI 304 steel, Scr. Mater. 37(11) (1997) 1831-1837.
[69] S.B. Dai, W.C. Liu, First-principles study on the structural, mechanical and electronic properties of delta and gamma " phases in Inconel 718, Comp. Mater. Sci. 49(2) (2010) 414-418.
[70] M. Hoelzel, S.A. Danilkin, H. Ehrenberg, D.M. Toebbens, T.J. Udovic, H. Fuess, H. Wipf, Effects of high-pressure hydrogen charging on the structure of austenitic stainless steels, Mater. Sci. Eng. A 384(1-2) (2004) 255-261.
[71] R. Kirchheim, A. Pundt, 25 - Hydrogen in Metals, in: D.E. Laughlin, K. Hono (Eds.), Physical Metallurgy (Fifth Edition), Elsevier, Oxford, 2014, pp. 2597-2705.
[72] W. Abuzaid, H. Sehitoglu, Critical resolved shear stress for slip and twin nucleation in single crystalline FeNiCoCrMn high entropy alloy, Mater. Charact. 129 (2017) 288-299.
[73] T. Depover, E. Wallaert, K. Verbeken, On the synergy of diffusible hydrogen content and hydrogen diffusivity in the mechanical degradation of laboratory cast Fe-C alloys, Mater. Sci. Eng. A 664 (2016) 195-205.
[74] H. Luo, Z.M. Li, W.J. Lu, D. Ponge, D. Raabe, Hydrogen embrittlement of an interstitial equimolar high-entropy alloy, Corros. Sci. 136 (2018) 403-408.
[75] K.E. Nygren, S. Wang, K.M. Bertsch, H.B. Bei, A. Nagao, I.M. Robertson, Hydrogen embrittlement of the equi-molar FeNiCoCr alloy, Acta Mater. 157 (2018) 218-227.
[76] G.C. Obasi, Z. Zhang, D. Sampath, R. Morana, R. Akid, M. Preuss, Effect of microstructure and alloy chemistry on hydrogen embrittlement of precipitation-hardened Ni-based alloys, Metall. Mater. Trans. A 49a(4) (2018) 1167-1181.
[77] G. Odemer, E. Andrieu, C. Blanc, Influence of hydrogen on electrochemical behavior of Ni-based superalloy 718, Int. J. Hydrog. Energy 43(2) (2018) 1006-1011.
[78] I.M. Robertson, The effect of hydrogen on dislocation dynamics, Eng. Fract. Mech. 68(6) (2001) 671-692.

[79] P.J. Ferreira, I.M. Robertson, H.K. Birnbaum, Influence of hydrogen on the stacking-fault energy of an austenitic stainless steel, Mater. Sci. Forum 207-209 (1996) 93-96.
[80] J.D. Hermida, A. Roviglione, Stacking fault energy decrease in austenitic stainless steels induced by hydrogen pairs formation, Scr. Mater. 39(8) (1998) 1145-1149.
[81] W.A.T. Clark, R.H. Wagoner, Z.Y. Shen, T.C. Lee, I.M. Robertson, H.K. Birnbaum, On the Criteria for Slip Transmission across Interfaces in Polycrystals, Scr. Metall. Mater. 26(2) (1992) 203-206.
[82] N. Kheradmand, A.F. Knorr, M. Marx, Y. Deng, Microscopic incompatibility controlling plastic deformation of bicrystals, Acta Mater. 106 (2016) 219-228.
[83] T.C. Lee, I.M. Robertson, H.K. Birnbaum, TEM in situ deformation study of the interaction of lattice dislocations with grain boundaries in metals, Philos. Mag. A 62(1) (1990) 131-153.
[84] E.A. West, G.S. Was, A model for the normal stress dependence of intergranular cracking of irradiated 316L stainless steel in supercritical water, J. Nucl. Mater. 408(2) (2011) 142-152.
[85] T.C. Lee, I.M. Robertson, H.K. Birnbaum, Prediction of Slip Transfer Mechanisms across Grain-Boundaries, Scr. Metall. Mater. 23(5) (1989) 799-803.
[86] E. Werner, W. Prantl, Slip transfer across grain and phase boundaries, Acta Metall. Mater. 38(3) (1990) 533-537.
[87] I. Adlakha, K.N. Solanki, Critical assessment of hydrogen effects on the slip transmission across grain boundaries in alpha-Fe, Proc. Math. Phys. Eng. Sci. 472(2185) (2016).
[88] R. Kirchheim, Reducing grain boundary, dislocation line and vacancy formation energies by solute segregation. I. Theoretical background, Acta Mater. 55(15) (2007) 5129-5138.

Paper II

On the study of hydrogen embrittlement behavior of nickel-based superalloys: Alloy 718 vs Alloy 725

Xu Lu, Yan Ma, Dong Wang

To be submitted.

This article is awaiting publication and is therefore not included.

Paper III

Hydrogen effect on the deformation behavior of Alloy 725 micropillars containing grain boundaries

Xu Lu, et al.

To be submitted.

This article is awaiting publication and is therefore not included.

Paper IV

Hydrogen susceptibility of an interstitial equimolar high-entropy alloy revealed by in-situ electrochemical microcantilever bending test

Xu Lu, Dong Wang, Zhiming Li, Yun Deng, Afrooz Barnoush

Materials Science and Engineering: A 762 (2019) 138114.

Hydrogen susceptibility of an interstitial equimolar high-entropy alloy revealed by in-situ electrochemical microcantilever bending test

Xu Lu, Dong Wang, Zhiming Li, Yun Deng, Afrooz Barnoush

Abstract: Hydrogen effect on an interstitial CoCrFeMnNi high-entropy alloy was investigated by micro-cantilever bending tests with pre-notched {111} plane as a case study. Results showed sharp mode I cracks on (001) plane bisecting two {111} planes in hydrogen-charged cantilevers, which was explained by hydrogen-assisted defects formation and hydrogen pins dislocation motion.

Keywords: Hydrogen embrittlement; micro-cantilever bending test; hydrogen enhanced localized plasticity; high-entropy alloy.

1. Introduction

The development of high-entropy alloys (HEAs) opened a new era of alloying design with multi-principal elements in equimolar or near-equimolar ratios [1-4]. These alloys show excellent mechanical properties at various temperatures [5-8], which offer HEA with promising applications in transportation, nuclear construction, etc [9]. However, hydrogen effect on the mechanical properties of HEA is critical and should be studied in detail before applications. This is due to the fact that hydrogen is generally presented in the service environment of engineering materials. The Cantor alloy [2], i.e., equimolar CoCrFeMnNi with a single-phase face-centered cubic (FCC) structure was recently reported to exhibit good resistance to hydrogen embrittlement at a relatively low hydrogen content less than 4290.1 at. ppm (76.5 mass ppm) [10-13]. However, when the hydrogen content reaches to a level more than 6337.0 at. ppm (113.0 mass ppm), this HEA is also susceptible to hydrogen embrittlement [14, 15]. More recently, the interstitial carbon doped equiatomic and non-equiatomic HEAs were reported to possess higher tensile strength with enhanced work hardening behavior compared to carbon-free reference materials [10, 11, 14]. Also, the hydrogen embrittlement behavior of a typical interstitial HEA with nominal composition $Co_{19.9}Cr_{19.9}Fe_{19.9}Mn_{19.9}Ni_{19.9}C_{0.5}$ (at. %) was studied in a macroscale level [16]. This interstitial HEA showed a mixture of intergranular and transgranular fracture as well as microvoid coalescence in presence of 315.6 at. ppm (5.65 mass ppm) hydrogen, companied by a 12 % reduction in fracture elongation [16]. However, macroscale tests are not capable of providing an

intuitive view of hydrogen-metal/defects interactions due to the unavoidable effects of grain boundaries and complex stress/strain states in each grain. Thus, we used the recently developed micro-cantilever bending test in combination with in-situ hydrogen charging [17-21] to reveal the effect of hydrogen on the cracking behavior of a FCC structured interstitial HEA. By using a controllable hydrogen charging method, the local cracking behavior at stress concentrated areas was traced and compared explicitly in both hydrogen-free and hydrogen-charged environment.

2. Materials and experimental procedure

The homogenized interstitial equimolar CoCrFeMnNi HEA with nominal composition $Co_{19.9}Cr_{19.9}Fe_{19.9}Mn_{19.9i}Ni_{19.9}C_{0.5}$ (at. %) and an average grain size of 226 μm was used. The material was prepared by casting and hot-rolling at 900 °C, followed by homogenization at 1200 °C for 2 hours and water-quenching [22]. The samples were prepared by grinding and mechanical polishing, followed by electropolishing in a methanolic H_2SO_4 solution as the final step to obtain a deformation-free surface [23]. Both high-resolution scanning electron microscopy (SEM, Thermo Fisher Scientific Inc., USA.) and electron backscatter diffraction (EBSD) were used to define the directions for milling cantilevers, as shown in Fig. 1 (a)-(b). Milling of cantilevers with pentagonal cross section was carried out by using focused ion beam (Helios Nanolab Dual Beam FIB, Thermo Fisher Scientific Inc., USA). Due to the lack of available data for the crystal planes that are most fragile to cracking, all the cantilevers were pre-notched to study the plane of {111} with the lowest surface energy. Fig. 1 (c) and Table 1 show the details of beam dimensions. By integrating a miniaturized three-electrode electrochemical cell into Hysitron TI950 TriboIndenter [17, 18, 20], in-situ micromechanical test revealing the effect of hydrogen upon deformation can be conducted. To introduce sufficient hydrogen, cantilevers were firstly charged at -1400 $mV_{/Hg/HgSO4}$ for 40 h (refers to H1), then further charged at -1600 $mV_{/Hg/HgSO4}$ for 20 h (refers to H2) in the electrolyte consisted of glycerol-based borax with 0.002 mol/L $Na_2S_2O_3$ [24]. This electrolyte is able to preserve the surface integrity and provide precise details of deformation after bending. We used a conical tip with a nominal tip radius of 0.5 μm to perform the bending tests. The load function was designed by integrating partial-loading-unloading sequences after yielding at a loading rate of 2 nm/s. Afterwards, SEM was used to visualize the microstructure evolution. Also, FIB thinning perpendicular to the notch plane was performed, and secondary electron (SE) images during each thinning step were taken at the cracking area. When the beams

were milled to a thickness of approximately 200 nm, a novel transmission EBSD (t-EBSD) was applied for high-resolution post-mortem microstructure analysis, and transmission electron microscopy (TEM, JEM-2100, JEOL, Inc.) technique was applied to characterize the deformation substructure after bending.

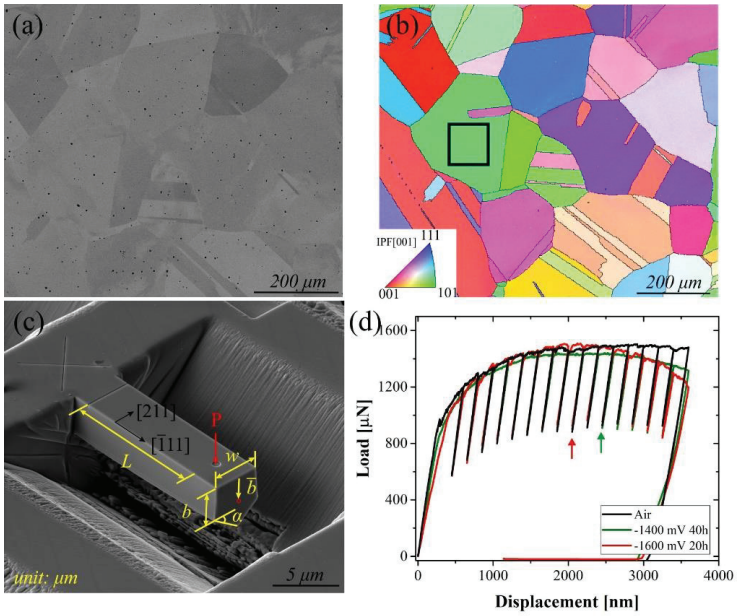

Fig. 1 (a) Back-scattered electron (BSE) micrograph of the studied interstitial HEA; (b) the corresponding inverse pole figure (IPF) map showing the selected grain orientation for milling cantilevers; (c) the characteristic dimensions of cantilevers; (d) load-displacement (L-D) curves of cantilevers bent in air and at two different hydrogen charging conditions, i.e., -1400 mV for 40 h (H1) and -1600 mV for 20 h (H2).

Table 1 Beam dimensions of cantilevers (dimensions in μm, angle in °). The symbols L, w, b, represent the length, width, side height of the beams. $\bar{b}$ is the distance from the upper surface to the geometric center, and α is the base angle of the isosceles triangle.

Beam	L	w	b	$\bar{b}$	α
Can_{air}	11.99±0.06	3.95±0.10	3.04±0.31	1.94±0.09	45
Can_{H}	11.99±0.02	4.00±0.05	2.86±0.04	1.89±0.04	45

3. Results and discussions

Fig. 1 (d) shows the representative load-displacement (L-D) curves obtained in air and at two charging conditions, i.e., H1 and H2. All beams exhibit linear elastic behavior in the first stage; the slight deviation in elastic properties could be caused by the small differentiation in beam geometries. Meanwhile, the absorption of hydrogen had no significant influence on the yield strength (YS, defined as 0.2% offset stress). After reaching the yield points, L-D curves show similar plastic strain hardening regimes, and cantilever bent in air reaches plateau till unloading at 3500 nm displacement, while the flow stresses of beams tested in H1 and H2 conditions start decreasing gradually from the 11th and 9th of the loading-unloading cycles, respectively, as marked by green and red arrows in Fig. 1 (d). The beam tested in H1 condition shows 8.4 % reduction in the flow stress compared to the maximum stress value. By further decreasing the charging potential to -1600 mV (H2 condition), which approximates to an increment of current density by one order of magnitude, a reduction of 20.5 % in flow stress is observed.

Fig. 2 shows the micrographs of beams after bending at different conditions. To study the most noticeable effect of hydrogen, we chose H2 charging condition for the following discussion. In Fig. 2 (a1), abundant slip lines (marked by black lines) on the beam surface bent in air elucidate a large amount of plasticity was generated during deformation. According to Schmid's law, dislocation slips on (111), $(11\bar{1})$, and $(1\bar{1}1)$ slip planes with an equal Schmid value of 0.272 were activated to compensate the plastic deformation, which is reflected by the slip traces on beam surface in Fig. 2 (a1). Here we use Schmid's law by assuming that on the top layer of the beams, uniaxial tensile stress dominated at the beginning of bending [25]. Notch blunting with a tip opening angle of 52.7° in air indicates a superior ductility and a high resistance to cracking of the studied interstitial HEA. The formation of microvoids at the crack tip, as pointed out by the white arrows in Fig. 2 (a1) and the magnified notch area in Fig. 2 (a2), elucidates a typical ductile fracture mode. On the contrary, beams bent in H2 condition had entirely different cracking behavior. Fig. 2 (b1) shows a sharp cracking of the notch plane (marked in red circle) with a smaller crack-tip opening angle of 27.2°. It is worth noting that the number of slip lines in Fig. 2 (b1) was remarkably reduced compared to that in Fig. 2 (a1), which indicates that the cracking process consumed part of the plasticity. And rugged fracture surfaces on the cracking plane shows a quasi-cleavage fracture behavior (Fig. 2 (b1)-(b2)). It is worth mentioning that due to the effect of beam size and

the space limitation beneath the beams, it was unable to obtain fracture surfaces in the current tests. Optimization will be made in the following studies.

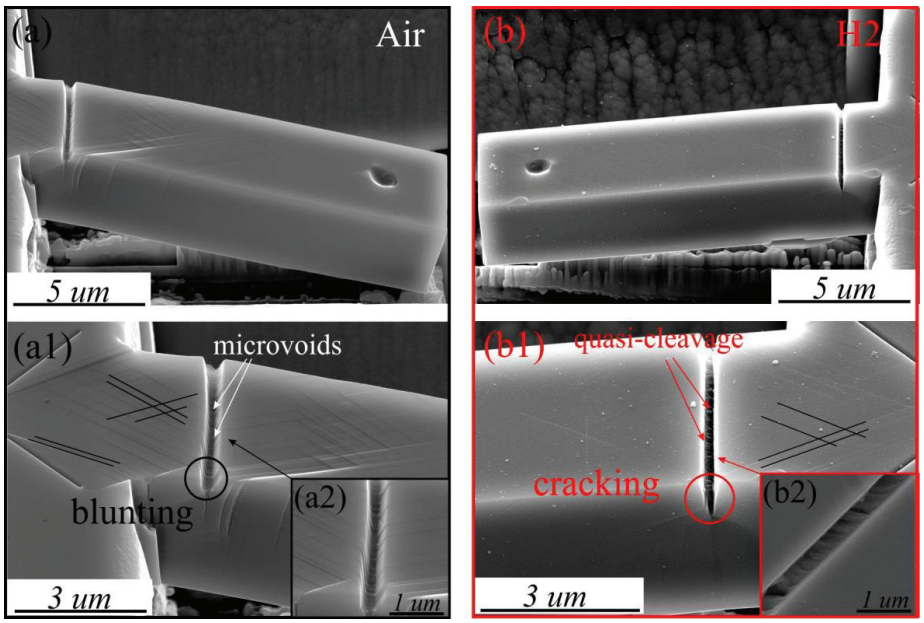

Fig. 2 (a), (a1) Secondary electron (SE) images showing deformation behavior of beams bent in air, and (b), (b1) in H2 charging condition; (a2) and (b2) magnified notch area in (a1) and (b1) after bending.

Fig. 3 shows the detailed characterization of beam cross sections after bending. Notch blunting is observed in the hydrogen-free condition (Fig. 3 (a1)-(a4)). At regions close to the beam surface, where plane stress condition prevails and plastic flow is relatively easy, the blunted notch shows a depth of 234.5 nm (Fig. 2 (a2)). This observation is consistent with the micrographs shown in Fig. 2 (a)-(a1). The notch crack becomes steep with an increase in depth of about 50 nm from beam surface (Fig. 3 (a2)) to the interior (Fig. 3 (a4)). In the central part of the beam, the notch tip sensed triaxial stress in a plane strain condition. And the more pronounced blunting behavior in the plane strain condition is caused by the difficulty of plastic flow and an enhanced stress concentration at the notch tip. Fig. 3 (a5) shows the Kernel Average Misorientation (KAM) map of the beam bent in air obtained from t-EBSD. Crystallographic misorientation beneath the notch tip indicates high geometrically necessary dislocation (GND) densities in three directions (marked with red dotted

lines), which correspond to the {111} slip traces marked in red. A large plastic zone is highlighted by the yellow dotted line. In comparison, hydrogen-assisted cracking happened on beams bent in H2 condition. In the plane stress condition, cracking propagated along the notch plane, followed by a deviation of the crack path into a non-specific-slip-plane (Fig. 3 (b2)). Fig. 3 (b3) shows the transition morphology of the crack from the surface to the middle region of the beam, i.e. cracking followed the notch plane for merely 80 nm then deviated as a sharp crack. In the plane strain condition, cracking deviated directly beneath the notch tip (Fig. 3 (b4)). Such variation in the cracking behavior on the beam surface and the center region is dependent on the local stress state. On the beam surface, the notch tip sensed less constraint from the material, thus hydrogen-assisted cracking grew parallel to the notch plane. In comparison, the notch crack in the center region of the beam sensed a triaxial stress and cracking accordingly. KAM map in Fig. 3 (b5) shows a confined plastic zone compared to Fig. 3 (a5). Dislocation activities dominant in two slip planes, i.e., $(11\bar{1})$ and (111) (marked with red dotted lines). The resultant crack bisecting those two planes is aligned with (001) plane trace. Additionally, Fig. 3 (c) shows a reduced GND density in presence of hydrogen by measuring the crystallographic misorientations beneath the notch crack tip, which are highlighted by the yellow arrows in Fig. 3 (a5) and (b5). Further dislocation analyses on beam cross sections were performed with TEM. Bright-field images (Fig. 4 (a) and (b)) in two test conditions are consistent with the t-EBSD results. Deformation in air induced a large amount of plasticity below the blunted notch, and the high density of dislocations expand through the whole beam (Fig. 4 (a)). It is difficult to figure out dislocation structures since massive dislocations interact and tangle after deformation. Despite this, three slip bands can be clearly observed, which correspond to the active slip planes in Fig. 3 (a5). By contrast, hydrogen leads to a reduced and more localized plastic zone at the cracking area in Fig. 4 (b), which is consistent with the KAM map shown in Fig. 3 (b5). The two slip bands with high dislocation densities at the notch tip correspond to $(11\bar{1})$ and (111) plane traces, respectively.

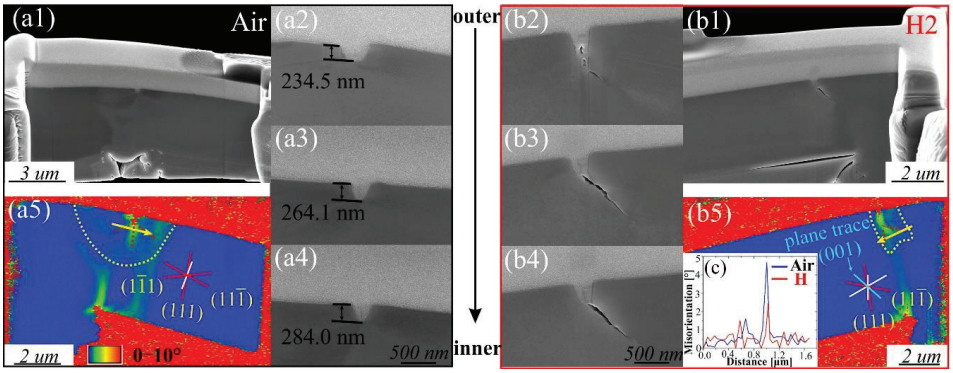

Fig. 3 SE images of beams cross-sections showing details of the cracking behavior (a1-a4) in air and (b1-b4) in H2 condition; (a5), (b5) KAM maps of two beams obtained from t-EBSD; and (c) misorientation data obtained close to the notch cracking.

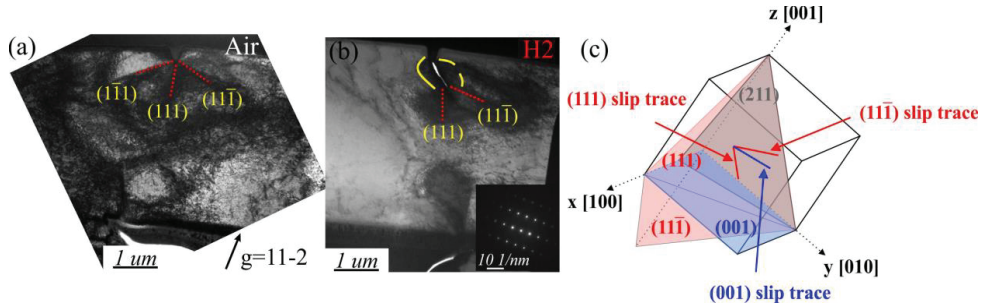

Fig. 4 Bright-field TEM micrographs showing dislocation morphologies of cantilevers bent in (a) air and (b) H2 condition; (c) a schematic showing the relation between the activated {111} slip planes and the (001) crack plane.

Based on the above results, the cracking behavior of the interstitial HEA is highly influenced by introducing hydrogen. In the hydrogen-free condition, when the plastic deformation began, the notch tip acted as a stress concentrator and dislocation nucleation started on the slip planes that reached the critical resolved shear stress. Dislocations generated at the notch tip continuously move away, which relieved the local stress effectively and the deformation process continued by notch blunting. All slip systems with the same Schmid factor were activated in the hydrogen-free beam to compensate the deformation process. As a result, a large plastic zone with a value of about 6.28 μm^2 was observed. In contrast, when hydrogen was presented at the notch tip, we observed a sharp crack with a reduced plastic zone (about 2.83 μm^2) instead of notch blunting. According to

the “Defactant” model proposed by Kirchheim [26, 27], the formation energy of dislocations [24, 28] and vacancies was reduced by adding hydrogen. Dislocation nucleation and multiplication started upon plastic deformation. With hydrogen absorbed into the material and segregated to the dislocations, massive dislocation-dislocation and dislocation-hydrogen interactions were triggered at the notch tip. Also, the creation of strain-induced vacancies was enhanced by hydrogen atoms [29]. Hydrogen and hydrogen-vacancy clusters were proposed to effectively pin dislocations from movement [17, 19, 20, 30], as reflected by the reduced plastic zone at both sides of the crack. With further deformation, dislocations were unable to move away, and local strain increased drastically due to pronounced dislocation interactions near the notch front. The local stress intensity gradually reached to the critical value for micro-cracks formation. As a result, the first micro-crack initiated, and the local deformation energy was released. The crack propagation was realized by operating multiple slips on alternating $(11\bar{1})$ and (111) planes, and a mode I crack on (001) plane was created bisecting two $\{111\}$ planes. In this way, the plastic deformation was continuously consumed by the cracking process. Also, the nucleation and growth of microvoids at slip-band interactions or other defects ahead of the crack tip further contribute to the crack growth and result in a small crack-tip opening angle [31]. A schematic summary is shown in Fig. 4 (c), where cracking happened along $< 110 >$ direction on (001) plane. The projection of slip planes and crack plane on the beam cross-section is highlighted. The comparable resolved shear stress values for two intersecting conjugate $\{111\}$ planes were proposed to cause the decohesion bisecting slip planes [32]. However, due to the complex stress state and dislocation activities at the notch tip, the values of resolved shear stress on each active slip plane cannot be obtained in the current study. Therefore, further study will be performed by combining elastic-plastic fracture mechanics and discrete dislocation dynamics simulations to analyze the local stress values in each testing conditions.

4. Conclusions

In summary, hydrogen assisted cracking behavior of a carbon-doped equimolar CoCrFeMnNi high-entropy alloy (HEA) was studied by performing in-situ micro-cantilever bending test in combination with advanced high-resolution characterizing techniques (transmission EBSD and TEM). Pre-notch on $\{111\}$ plane was chosen as a case study. Results showed that this alloy exhibited superior strength and ductility upon loading in air, notch blunting alone was observed

on the bent cantilevers. While in the hydrogen-charged cantilevers, a sharp cracking on (001) plane bisecting two {111} slip planes was observed. In this study, we show that the initiation and growth of micro-cracks were attributed to the synergetic effect of hydrogen-assisted defects formation and the pinning effect of hydrogen to dislocation motion, which causes the local stress intensity to reach to the critical value for micro-crack formation. As a result, a localized plasticity and a reduced average geometrically necessary dislocation (GND) density were observed. Worthy of mentioning, in order to understand the effect of grain orientation, different crack systems will be designed and tested to get a comprehensive view of hydrogen-assisted cracking in interstitial HEAs.

Acknowledgements

The Research Council of Norway is acknowledged for the support to the Norwegian Micro- and Nano-Fabrication Facility, NorFab, project number 245963/F50. The authors gratefully acknowledge the financial support from project HyF-Lex (244068/E30), and the European Research Council under the EU's 7th Framework Programme (FP7/2007-2013)/ERC grant agreement 290998. The TEM work was performed at TEM Gemini Center, Norwegian University of Science and Technology (NTNU), Norway.

Data availability

The raw/processed data required to reproduce these findings cannot be shared at this time as the data also forms part of an ongoing study.

References

[1] J.W. Yeh, S.K. Chen, S.J. Lin, J.Y. Gan, T.S. Chin, T.T. Shun, C.H. Tsau, S.Y. Chang, Nanostructured high-entropy alloys with multiple principal elements: Novel alloy design concepts and outcomes, Adv. Eng. Mater. 6(5) (2004) 299-303.
[2] B. Cantor, I.T.H. Chang, P. Knight, A.J.B. Vincent, Microstructural development in equiatomic multicomponent alloys, Mater. Sci. Eng. A 375 (2004) 213-218.
[3] Z. Li, K.G. Pradeep, Y. Deng, D. Raabe, C.C. Tasan, Metastable high-entropy dual-phase alloys overcome the strength-ductility trade-off, Nature 534 (7606) (2016) 227-30.
[4] Y. Zhang, T.T. Zuo, Z. Tang, M.C. Gao, K.A. Dahmen, P.K. Liaw, Z.P. Lu, Microstructures and properties of high-entropy alloys, Prog. Mater. Sci. 61 (2014) 1-93.
[5] B. Gludovatz, A. Hohenwarter, D. Catoor, E.H. Chang, E.P. George, R.O. Ritchie, A fracture-resistant high-entropy alloy for cryogenic applications, Science 345(6201) (2014) 1153-1158.
[6] F. Otto, A. Dlouhy, C. Somsen, H. Bei, G. Eggeler, E.P. George, The influences of temperature and microstructure on the tensile properties of a CoCrFeMnNi high-entropy alloy, Acta Mater. 61(15) (2013) 5743-5755.
[7] Y.H. Jo, S. Jung, W.M. Choi, S.S. Sohn, H.S. Kim, B.J. Lee, N.J. Kim, S. Lee, Cryogenic strength improvement by utilizing room-temperature deformation twinning in a partially recrystallized VCrMnFeCoNi high-entropy alloy, Nat. Commun. 8 (2017).
[8] A.J. Zaddach, R.O. Scattergood, C.C. Koch, Tensile properties of low-stacking fault energy high-entropy alloys, Mater. Sci. Eng. A 636 (2015) 373-378.
[9] Y.F. Ye, Q. Wang, J. Lu, C.T. Liu, Y. Yang, High-entropy alloy: challenges and prospects, Mater. Today 19(6) (2016) 349-362.
[10] H. Luo, Z. Li, D. Raabe, Hydrogen enhances strength and ductility of an equiatomic high-entropy alloy, Sci. Rep. 7(1) (2017) 9892.
[11] Y. Zhao, D.-H. Lee, M.-Y. Seok, J.-A. Lee, M.P. Phaniraj, J.-Y. Suh, H.-Y. Ha, J.-Y. Kim, U. Ramamurty, J.-i. Jang, Resistance of CoCrFeMnNi high-entropy alloy to gaseous hydrogen embrittlement, Scr. Mater. 135 (2017) 54-58.
[12] H. Luo, Z.M. Li, A.M. Mingers, D. Raabe, Corrosion behavior of an equiatomic CoCrFeMnNi high-entropy alloy compared with 304 stainless steel in sulfuric acid solution, Corros. Sci. 134 (2018) 131-139.
[13] H. Luo, W. Lu, X. Fang, D. Ponge, Z. Li, D. Raabe, Beating hydrogen with its own weapon: Nano-twin gradients enhance embrittlement resistance of a high-entropy alloy, Mater. Today (2018).
[14] K.E. Nygren, K.M. Bertsch, S. Wang, H. Bei, A. Nagao, I.M. Robertson, Hydrogen embrittlement in compositionally complex FeNiCoCrMn FCC solid solution alloy, Curr.Opin. Solid St. M. (2017).
[15] K. Ichii, M. Koyama, C.C. Tasan, K. Tsuzaki, Comparative study of hydrogen embrittlement in stable and metastable high-entropy alloys, Scr. Mater. 150 (2018) 74-77.
[16] H. Luo, Z.M. Li, W.J. Lu, D. Ponge, D. Raabe, Hydrogen embrittlement of an interstitial equimolar high-entropy alloy, Corros. Sci. 136 (2018) 403-408.
[17] Y. Deng, A. Barnoush, Hydrogen embrittlement revealed via novel in situ fracture experiments using notched micro-cantilever specimens, Acta Mater. 142 (2018) 236-247.
[18] T. Hajilou, Y. Deng, B.R. Rogne, N. Kheradmand, A. Barnoush, In situ electrochemical microcantilever bending test: A new insight into hydrogen enhanced cracking, Scr. Mater. 132 (2017) 17-21.

[19] B.R.S. Rogne, N. Kheradmand, Y. Deng, A. Barnoush, In situ micromechanical testing in environmental scanning electron microscope: A new insight into hydrogen-assisted cracking, Acta Mater. 144 (2018) 257-268.
[20] Y. Deng, T. Hajilou, D. Wan, N. Kheradmand, A. Barnoush, In-situ micro-cantilever bending test in environmental scanning electron microscope: Real time observation of hydrogen enhanced cracking, Scr. Mater. 127 (2017) 19-23.
[21] Y. Deng, T. Hajilou, A. Barnoush, Hydrogen-enhanced cracking revealed by in situ micro-cantilever bending test inside environmental scanning electron microscope, Philos. Trans. Royal Soc. A 375(2098) (2017).
[22] Z. Li, Interstitial equiatomic CoCrFeMnNi high-entropy alloys: carbon content, microstructure, and compositional homogeneity effects on deformation behavior, Acta Mater. 164 (2019) 400-412.
[23] A. Barnoush, H. Vehoff, Electrochemical nanoindentation: A new approach to probe hydrogen/deformation interaction, Scr. Mater. 55(2) (2006) 195-198.
[24] D. Wang, X. Lu, Y. Deng, X. Guo, A. Barnoush, Effect of hydrogen on nanomechanical properties in Fe-22Mn-0.6C TWIP steel revealed by in-situ electrochemical nanoindentation, Acta Mater. 166 (2019) 618-629.
[25] B. Bhushan, Springer Handbook of Nanotechnology, 3 ed., Springer-Verlag Berlin Heidelberg2010.
[26] A. Pundt, R. Kirchheim, Hydrogen in metals: Microstructural aspects, Annu. Rev. Mater. Res. 36 (2006) 555-608.
[27] R. Kirchheim, Reducing grain boundary, dislocation line and vacancy formation energies by solute segregation. I. Theoretical background, Acta Mater. 55(15) (2007) 5129-5138.
[28] A. Barnoush, H. Vehoff, Recent developments in the study of hydrogen embrittlement: Hydrogen effect on dislocation nucleation, Acta Mater. 58(16) (2010) 5274-5285.
[29] K. Takai, H. Shoda, H. Suzuki, M. Nagumo, Lattice defects dominating hydrogen-related failure of metals, Acta Mater. 56(18) (2008) 5158-5167.
[30] D. Xie, S. Li, M. Li, Z. Wang, P. Gumbsch, J. Sun, E. Ma, J. Li, Z. Shan, Hydrogenated vacancies lock dislocations in aluminium, Nat. Commun. 7 (2016) 13341.
[31] S.P. Lynch, Mechanisms and Kinetics of Environmentally Assisted Cracking: Current Status, Issues, and Suggestions for Further Work, Metall. Mater. Trans. A 44a(3) (2013) 1209-1229.
[32] Q. Chen, H.W. Liu, Shear fatigue crack growth in large grain polycrystals, Proc. Am. Soc. Test. Mater. 1220 (1995) 467-483.